NASA Contractor Report 3958

Ames
IN-02
3611
p 137

A New Methodology for Free Wake Analysis Using Curved Vortex Elements

Donald B. Bliss, Milton E. Teske,
and Todd R. Quackenbush

CONTRACT NAS2-11295
NOVEMBER 1987

(NASA-CR-3958) A NEW METHODOLOGY FOR FREE WAKE ANALYSIS USING CURVED VORTEX ELEMENTS Final Report (Continuum Dynamics) 137 p CSCL 01A
N91-12047
Unclas
H1/02 0003611

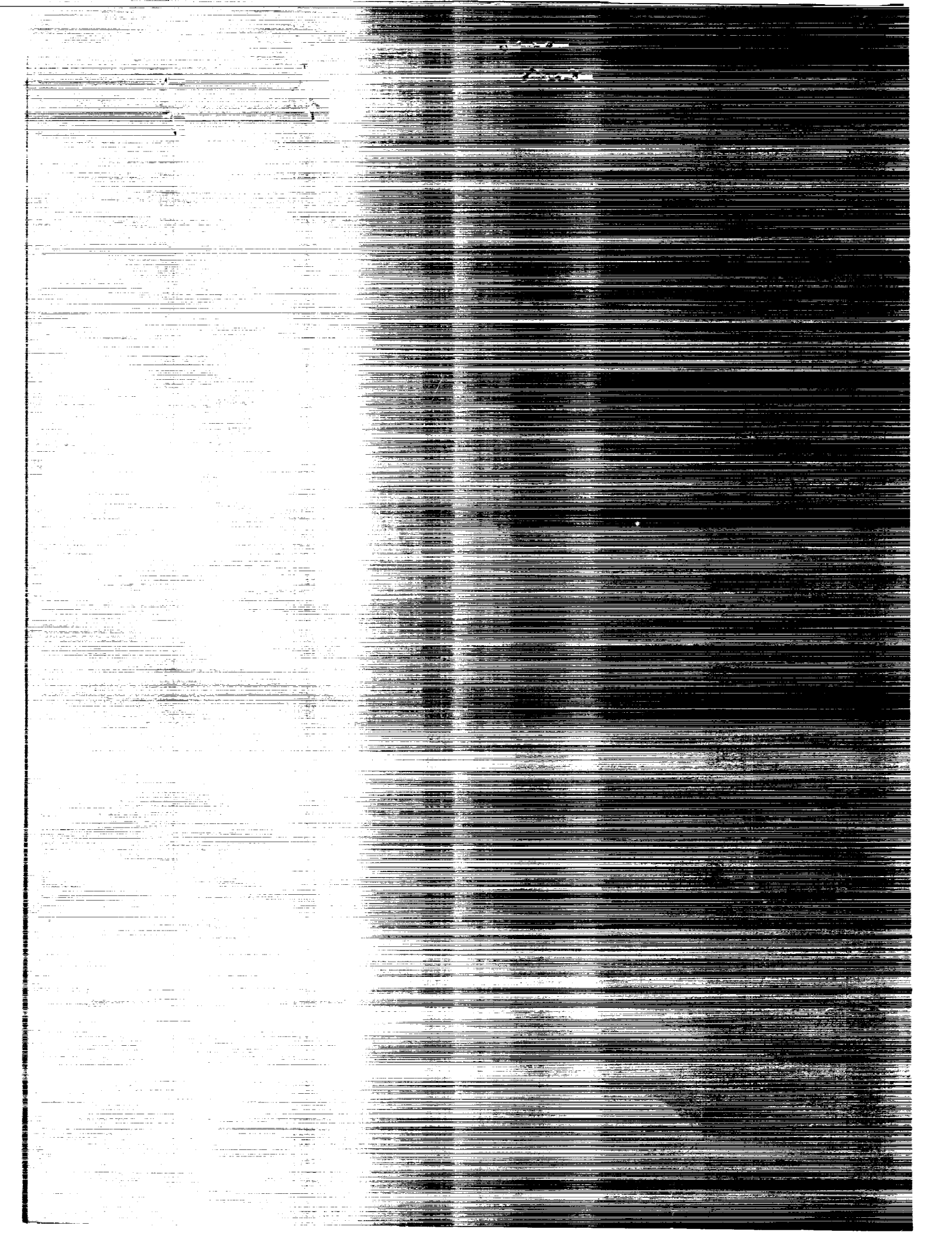

NASA Contractor Report 3958

A New Methodology for Free Wake Analysis Using Curved Vortex Elements

Donald B. Bliss, Milton E. Teske,
and Todd R. Quackenbush
Continuum Dynamics, Inc.
Princeton, New Jersey

Prepared for
Ames Research Center
under Contract NAS2-11295

National Aeronautics
and Space Administration

**Scientific and Technical
Information Division**

1987

PREFACE

This investigation was sponsored by the National Aeronautics and Space Administration, Ames Research Center, under contract NAS2-11295. The NASA Technical Monitor for this contract was Mr. Fort F. Felker. The Principal Investigator was Dr. Donald B. Bliss, Senior Associate, Continuum Dynamics, Inc. The Co-investigators were Dr. Milton E. Teske, Senior Associate, Continuum Dynamics, Inc., and Mr. Todd R. Quackenbush, Research Assistant, Princeton University. This report is also designated as Continuum Dynamics, Inc. Report No. 84-6.

ii INTENTIONALLY BLANK

PRECEDING PAGE BLANK NOT FILMED

A NEW METHODOLOGY FOR FREE WAKE ANALYSIS USING CURVED VORTEX ELEMENTS

Donald B. Bliss and Milton E. Teske
Continuum Dynamics, Inc., Princeton, New Jersey 08540

Todd R. Quackenbush
Princeton University, Princeton, New Jersey 08540

SUMMARY

This report describes research to evaluate the feasibility of using curved vortex elements to do rotor free wake calculations. The Basic Curved Vortex Element (BCVE) was developed for this purpose. The element is based on the approximate Biot-Savart integration for a parabolic arc filament shape. Special care was taken to insure the accuracy of the method at points close to the arc. A scheme called the interpolated point method was also developed to determine the curvature and orientation of these elements when placed between collocation points along the wake contour.

The computer time and accuracy of the BCVE were studied extensively in relation to the performance of the simpler straight-line elements which have traditionally been used. In numerical simulations, curved elements were found to be far more accurate in predicting vortex filament flow fields, even when much larger elements were used. Although the curved element is more complex analytically, the fact that the elements can be larger leads to a net reduction in computer time while maintaining a strong accuracy advantage.

As part of the accuracy study, the errors made by straight-line elements were evaluated. These errors were found to be related to deviations in position relative to the filament contour and to a failure to simulate the local curvature of the arc. Based on a local analysis, universal formulas were developed for predicting straight-line element errors. Within one element length of a vortex filament, straight-line elements induce velocity errors of the same order as the self-induced velocity due to local curvature, an effect included in free wake analyses. This raises a question of consistency in the straight-line element technique.

The curved element method was implemented into a forward flight free wake analysis using a time stepping approach. A new far wake model was also developed which utilizes free wake information to prescribe and update the far wake shape downstream of the free wake region. Sample calculations were performed for different element sizes and advance ratios for single and multi-blade rotors. The highly distorted free wake shapes showed a number of common features, the most distinctive being a strong tendency toward rapid roll-up of the sides of the wake immediately downstream of the rotor. A preliminary assessment was made of the effect of element size on the downwash field at a rotor blade, with there being only small differences between elements generated by 15°, 30° and 45° increments of blade rotation. In general, the curved element approach exhibited rapid convergence.

As a final demonstration of capability, the free wake routine was implemented into the Boeing Vertol B-65 rotor aerodynamics program. Previously, this code used a prescribed wake analysis for the tip vortex. Sample calculations were performed for a four-bladed rotor with a prescribed wake and with free wakes using different element sizes.

TABLE OF CONTENTS

TABLE OF CONTENTS (Cont'd)

NOMENCLATURE

a_B	radius of Betz vortex core
a_c	vortex core radius or length scale
a_v	radius of viscous vortex core
$a(x)$	coefficient of x_1^0 in quadratic expression, Eq. (12)
A	nondimensional kinetic energy of vortex core swirl velocity
$A_0, A_1, A_2, \ldots$	longitudinal flapping coefficients
b_t	distance from blade tip to point of maximum spanwise load
$b(x)$	coefficient of x_1^1 in quadratic expression, Eq. (12)
B	number of rotor blades
$B_0, B_1, B_2, \ldots$	lateral flapping coefficients
c	integration contour along vortex filament
$c(x)$	coefficient of x_1^2 in quadratic expression, Eq. (12)
C	nondimensional kinetic energy of vortex core axial velocity
d_c	cut-off distance for self-induced velocity
$d(x)$	subinterval integration limit, Eqs. (16) and (20)
$\vec{e}_r$	radial unit vector for local polar coordinates on a filament
$\vec{e}_\theta$	tangential unit vector for local polar coordinates on a filament
$F_0(x), F_1(x), F_2(x)$	approximating functions in piecewise quadratic model, Eqs. (17) and (18)
$h(x)$	piecewise continuous function in quadratic model, Eq. (19)
i	summation index
$\vec{i}$	unit vector in element Cartesian coordinate system, tangent to filament
$I_n(x)$	integrals arising in curved element model, Eq. (12) and Appendix

j	collocation point index along a vortex filament
$\vec{j}$	unit vector in element Cartesian coordinate system, inplane normal to filament
$\hat{j}$	interpolated point index number
$\vec{k}$	unit vector in element Cartesian coordinate system, normal to filament and filament plane
k_c	constant relating convergence time steps to number of elements, Eq. (54)
k_p	proportion constant in prescribed wake calculation time ratio, Eq. (50)
ℓ	half the distance between ends of a parbolic vortex element
ℓ_c	distance between ends of a curved vortex element
ℓ_s	distance between ends of a straight-line vortex element
$\vec{\ell}_s$	equivalent element length vector
m	intermediate value of summation index to apply integral approximation, Eq. (30)
M	number of velocity calculation points not in the free wake
$M(x,x_1)$	quadratic function for piecewise approximation of quartic term, Eq. (8)
$M_o, M_\pm$	subinterval representations of $M(x,x_1)$
n	summation index for far field element array
N	number of vortex elements per blade
N_c	number of curved vortex elements per blade
N_{FWC}	number of time steps for free wake convergence
N_s	number of straight-line vortex elements per blade
P	number of subinterval calculations per blade for points in the wake
$\vec{q}$	velocity vector
$\vec{q}_c$	velocity from nearby element corrected for core velocity distribution

$\vec{q}_{CA}$	velocity field near a curved element
$\vec{q}_D$	velocity vector from a discrete Biot-Savart element
$\vec{q}_{Di}$	velocity vector for the ith discrete Biot-Savart element along a filament
$\vec{q}_e$	velocity vector at the edge of a vortex core
$\Delta\vec{q}_F$	velocity error during final convergence of straight-line elements
$\Delta\vec{q}_L$	velocity error from the nearest straight-line element(s)
$\vec{q}_m$	velocity vector induced by nearby filament without vortex core effect
$\vec{q}_{row}$	net velocity from far field element row
$\vec{q}_{SL}$	velocity field near a straight-line element
$\Delta\vec{q}_{TOT}$	total velocity error associated with straight-line elements
$\vec{q}_1, \vec{q}_2$	velocity contributions of first and second elements in far wake element row
$\Delta\vec{q}_D$	velocity error from distant straight-line elements along a filament
Q	number of subinterval calculations per blade for points not on the wake
r	radial coordinate in local polar coordinates; radial distance from vortex filament
$\bar{r}$	normalized radial distance, r/a_c
r_m	minimum distance from a collocation point to a nearby curved element
$\vec{r}_s$	inter-element spacing vector in far field element row
$\vec{r}_v$	distance vector from point on filament to point of evaluation
$\vec{r}_{vi}$	distance from ith far wake element to point of evaluation
R	local radius of curvature of filament

R_o	equivalent radius of curvature of curved vortex element
R_r	rotor radius
$R_1(x_1)$	notation for $\lvert\vec{r}_v\rvert$ in element velocity integrals
s	arc length along filament
$d\vec{s}$	incremental arc length vector
$\Delta\vec{s}_i$	length vector of discrete Biot-Savart element
t	time
t_{CE}	computer time to find the velocity at one point using curved elements
t_{SL}	computer time to find the velocity at one point using straight-line elements
T_A	computer time for three-point circular arc geometry and orientation
T_{CE}	computer time for a curved element calculation (no subintervals)
$T_{CE(s)}$	computer time for a curved element calculation (with subintervals)
T_G	computer time for curved element geometry and local coordinates location
T_{IP}	computer time for interpolated point location scheme
T_{OC}	computer time to find velocity contributions not from the free wake
T_P	computer time for prescribed wake point generation
T_{SI}	computer time for a self-induced velocity calculation
T_{SL}	computer time for a straight-line element calculation
T_{UD}	computer time to update free wake collocation point locations
u	velocity component in x-direction
U	free stream velocity
v	velocity component in y-direction
$v_o(r)$	vortex core swirl velocity distribution
w	velocity component in z-direction

w_{CALC}	velocity component normal to the plane of a vortex ring, calculated using straight-line or curved vortex elements
w_{EXACT}	exact answer for the velocity component normal to the plane of a vortex ring
$w_o(r)$	vortex core axial velocity distribution
w_{SI}	local self-induced velocity
x	Cartesian coordinate in $\vec{i}$ direction of local element coordinate system
x_1	dummy variable for integration in x-direction
X	Cartesian coordinate in global reference coordinates, positive in direction of flight ($\psi = 180°$)
y	Cartesian coordinate in $\vec{j}$ direction of local element coordinate system
y_1	dummy variable for integration in the y-direction
Y	Cartesian coordinate in global reference coordinates, positive to the right of vehicle ($\psi = 90°$)
z	Cartesian coordinate in $\vec{k}$ direction of local element coordinate system
z_r	vertical distance directly above a vortex ring filament
z_1	dummy variable for integrations in the z-direction
Z	Cartesian coordinate in global reference coordinates, positive down
α	curve fitting constant in subinterval integration scheme, Eq. (20)
β	curve fitting constant in subinterval integration scheme, Eq. (20)
δ_c	Maximum position error of curved elements
δ_s	maximum position error of straight-line elements
Γ	total circulation
Γ_B	circulation at the edge of the Betz core radius

$\Gamma(r)$	distribution of circulation in a vortex core
Γ_v	circulation at the edge of the viscous core radius
Γ_o	constant part of curved element circulation
Γ_1	linearly varying part of curved element circulation
γ_c	correction factor applied to velocity to account for vortex core effects
Δ	discriminant in element integrals, see Appendix
$\Delta\psi$	azimuth angle increment associated with a single time step
ε	parabolic element amplitude constant
θ	angular variable in local polar coordinates
θ_a	arc angle variable along a curved element
θ_r	azimuth angle variable for a vortex ring
θ_o	equivalent curved element arc angle
θ_1, θ_2	circular arc angles between adjacent pairs of collocation points
μ	advance ratio, $U/\Omega R_r$
ν	kinetic viscosity of air
σ	exponent in calculation time analysis, $1 \leq \sigma \leq 2$
τ_{CE}	time to converge a curved element free wake calculation
τ_{SL}	time to converge a straight-line element free wake calculation
ψ	azimuth angle of principal rotor blade
Ω	rotor angular rotation rate
$( )\|_{arc}$	integration limits evaluated at the endpoints of an arc
$( )\|_{MP}$	evaluated around the mid point of a vortex element
$( )\|_{EP}$	evaluated around the endpoint of a vortex element(s)

1. INTRODUCTION

A critical issue in the field of rotor aerodynamics is the treatment of the wake. The wake is of primary importance in determining overall aerodynamic behavior and in predicting structural vibration and aerodynamic noise. The two most common approaches to rotor wake modelling can be broadly categorized as prescribed wake and free wake analyses.

In prescribed wake models, the wake position is determined according to some relatively simple criterion. For example, the wake location can be kinematically determined from the rotor motion and the downwash field derived from momentum theory. The Biot-Savart law can then be used to find the downwash induced by this wake at the rotor plane. In some schemes, the wake location may be adjusted by empirical factors or slightly updated as the calculation progresses. However, the determination of a prescribed wake shape always involves a process which does not consider in detail the various effects acting on the wake, and in particular the effect of the wake on itself. Thus, a prescribed wake configuration is not a valid free vortex flow. Prescribed wake methods are nevertheless valuable since they provide accurate results for some applications, and have the advantage of relative simplicity and low user cost.

Free wake models have been developed in an attempt to simulate in detail the actual shape and motion of the wake (Refs 1 through 15). The primary emphasis has been on locating the strong tip vortex, although methods have also been developed to model the inboard shed vorticity. Typically, the tip vortex has been approximated by a series of connected straight-line segments. The velocity induced at each connection point is calculated by integrating the Biot-Savart law over the rest of the wake and over the bound vorticity on the rotor. A cut-off distance approach is used to avoid singular behavior when evaluating the velocity induced on the vortex itself. The connection points are assumed to be convected at the local velocity over a small time increment. The wake location is then updated and new convection velocities are calculated. This procedure is continued until the solution

converges to a final wake configuration which is repeatable from cycle to cycle within some specified accuracy.

The currently available free-wake models have been somewhat more successful than prescribed wake models in the low speed flight regime. In particular, computed wake shapes show a fair degree of qualitative agreement with the primary features seen in flow visualization experiments, namely, wake contraction in very close proximity to the rotor plane, and a tendency in forward flight for the overlapping vortex filaments to "roll-up" along the sides of the wake downstream of the rotor. However, to obtain good quantitative agreement between predicted aerodynamic loads and experimental results often requires the judicious adjustment of calculation parameters. Furthermore, the considerable complexity and high operating cost of current free wake codes must also be viewed as a problem.

The purpose of this report is to describe a new method for free wake modelling. This method is intended to improve accuracy and to reduce computing time and cost. The central feature of this approach is the development of a new free wake element. The "Basic Curved Vortex Element" (BCVE) is a curved arc, typically of greater length than the straight-line segments used previously. The curved element has a constant circulation plus a linear variation to account for changes in tip vortex strength due to the azimuthal load variations experienced by the rotor blades. An approximate analytical solution can be obtained for such a curved vortex element, and this fact is largely responsible for making the curved element approach practical. The derivation of the curved vortex element is described in the next section. This element is to be used throughout the wake in place of straight-line elements.

Of particular importance to the success of the method is the development of a means to pass the arcs between the connection points along the wake. Since fewer elements are to be used, the choice of an optimum method for finding the properties of each arc is critically important. The problem is essentially one of determining an appropriate spline fit procedure for the vortex wake curve and ensuring that this procedure is compatible with the

efficient use of curved vortex elements. Several element connection schemes are described, and their advantages and disadvantages are discussed. The best of these, called the interpolated point method, is then used in subsequent calculations.

Because of its greater arc length and curved shape, which is naturally compatible with the wake shape, the wake can be modelled accurately with many fewer BCVE's than the straight-line segments normally used. Reducing the number of elements reduces the number of wake position points that must be updated in each solution iteration, which reduces the required computing time. Since the computer time to converge a free wake calculation depends strongly on the number of elements, there is a strong incentive to reduce the number of elements. However, the element model itself is more complicated and this partially offsets the savings in computer time. The computer time and accuracy of curved elements relative to straight-line elements have been studied thoroughly in Section 3. It is found that by using curved elements computer time can be reduced while avoiding significant errors associated with straight-line elements. An interesting result is that using straight-line elements incurs an error in the velocity field near a filament on the same order as the self-induction effect normally included.

The new curved element method has been incorporated into a forward flight free wake analysis. This analysis has been used on its own for demonstration purposes, and has also been implemented into an existing aerodynamic loads code developed by Boeing Vertol Company, replacing a prescribed wake routine. This forward flight free wake work is the subject of Sections 4 and 5 of this report. The curved element has also been used in a free wake hover analysis, described in Reference 13, and in a new approach to the hover problem, described in Reference 15.

2. CURVED VORTEX ELEMENTS

2.1 Vortex Element Models

Two types of vortex elements are required to implement a free wake analysis. The first type of element is used to evaluate the velocity induced at any point in the flow field not on the element itself. Traditionally, straight-line elments have been used for this purpose. The present work develops an alternate approach using a more sophisticated curved element. This curved element will be referred to as the Basic Curved Vortex Element, or BCVE. The second type of element is used only to evaluate the velocity induced by the element on itself. This element will be called the Self-Induction Vortex Element, or SIVE. The SIVE has been used previously by other researchers,[6,11-16] and will be described only briefly. The BCVE is new and will be described first and in more detail.

2.1.1 The Basic Curved Vortex Element (BCVE)

The derivation of the BCVE is based on the fact that the Biot-Savart integration can be done approximately, but accurately, for a parabolic arc. A parabolic arc is an excellent approximation to a circular arc passed between the same midpoint and end points up to fairly large arc angles, as the sketch in Figure 1 indicates. In the coordinates shown, the parabola is given by:

$$y = \varepsilon x^2 \tag{1}$$

where

$$\varepsilon = \frac{\cos\frac{\theta_o}{2} - 1}{R_o \sin^2\frac{\theta_o}{2}} \tag{2}$$

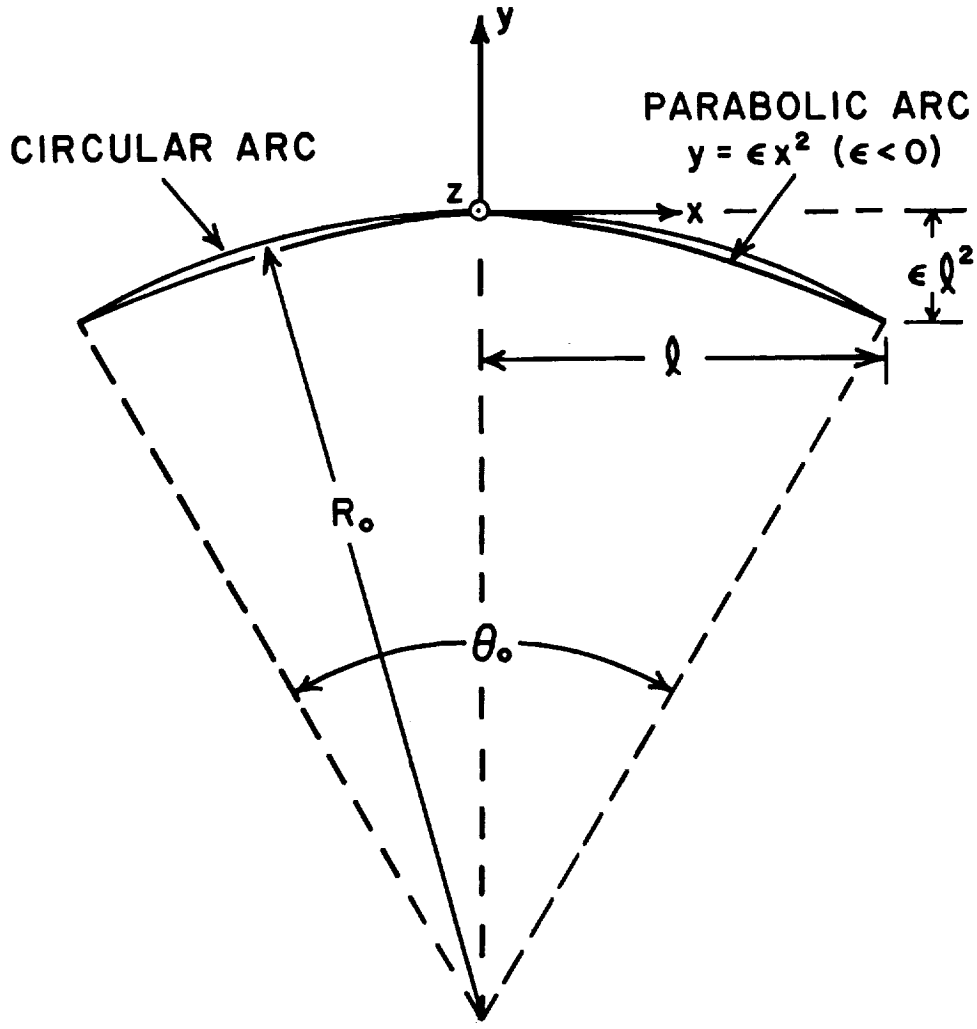

Figure 1. Comparison of parabolic arc and circular arc geometry.

For convenience, the parameter ε is defined in terms of the properties of the corresponding circular arc; note that $\varepsilon < 0$.

For the largest acceptable arcs, say 60° to 90°, there are discernible differences in the shape of circular and parabolic arcs. The differences in local slope and in curvature are most important near the end points. As will be shown later, even for large arcs the difference between a circular arc velocity field and a parabolic arc velocity field is only noticeable very near the arc, typically at distances much less than an arc length. However, the important point here is that introducing a curved element is the significant refinement over previous work. Whether the arcs which approximate the actual wake curve locally are parabolic or circular should not matter. In fact, in any calculation where this difference is important, the arc lengths are too large.

The geometry for performing the Biot-Savart integration is shown in Figure 2. The Biot-Savart law for the velocity vector $\vec{q}$ has the general form:

$$\vec{q} = -\frac{1}{4\pi}\int_c \frac{\Gamma\, \vec{r}_v \times d\vec{s}}{r_v^3} \tag{3}$$

The circulation Γ may vary along the arc provided that vorticity conservation is satisfied by some other part of the wake model, e.g., by using a model for an adjacent spanwise vortex sheet. This issue will not be considered further at present, other than to allow for a linear variation in Γ when evaluating Eq. (3). From Figure 2 the incremental arc length vector is given by

$$d\vec{s} = (\vec{i} + 2\varepsilon x_1 \vec{j})dx_1 \tag{4}$$

and the vector distance from the arc to the point of evaluation is

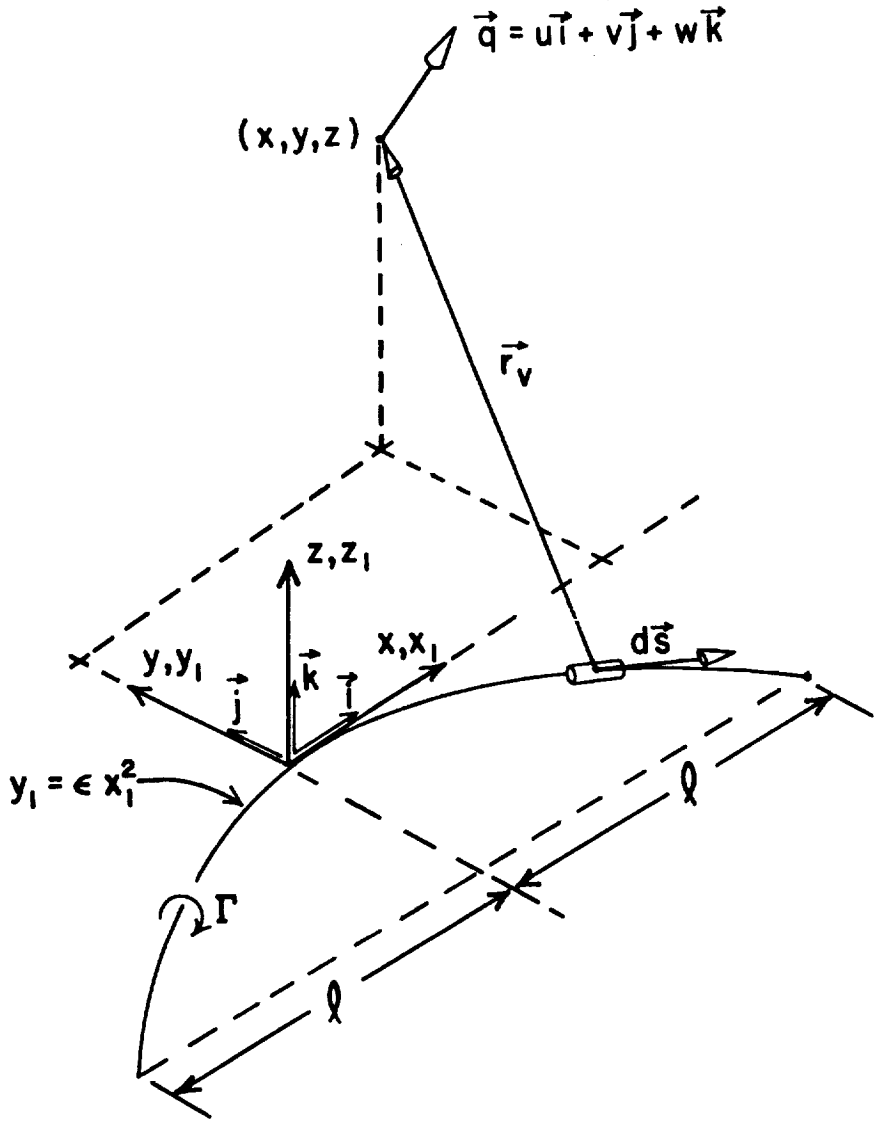

Figure 2. Geometry for the Biot-Savart integration over a parabolic arc.

$$\vec{r}_v = (x - x_1)\vec{i} + (y - \varepsilon x_1^2)\vec{j} + z\vec{k} \tag{5}$$

The cross-product of these quantities is found to be

$$\vec{r}_v \times d\vec{s} = -2\varepsilon z x_1 dx_1 \vec{i} + z dx_1 \vec{j} + (2\varepsilon x_1 x - \varepsilon x_1^2 - y) dx_1 \vec{k} \tag{6}$$

Calculating the cube of the magnitude of Eq. (5), and grouping terms in powers of x_1 yields

$$r_v^3 = \left\{(1 - 2\varepsilon y)x_1^2 + (-2x)x_1 + (x^2 + y^2 + z^2) + \varepsilon^2 x_1^4\right\}^{3/2} \tag{7}$$

The presence of the term $\varepsilon^2 x_1^4$ in the above provides the principal difficulty in evaluating Eq. (3) in a relatively simple analytical form. Although this term appears to be small, it is actually quite important when the point of evaluation is near the vortex filament, particularly when the arc angle is large. To obtain accurate results near the vortex it is necessary to model this term. The most elaborate model that allows for simple evaluation of Eq. (3) is a quadratic in x_1. The term to be modeled turns out to be most important when $x_1 \simeq x$, and thus the model, denoted by $M(x,x_1)$, must adapt to the value of x, namely

$$\varepsilon^2 x_1^4 \simeq M(x,x_1) = \varepsilon^2 \left[F_2(x)x_1^2 + F_1(x)x_1 + F_o(x)\right] \tag{8}$$

A single quadratic in x_1 cannot fit the function x_1^4 over the entire interval $-\ell < x_1 < \ell$ with sufficient accuracy for all choices of x_1, at least if very good accuracy is desired for points in the velocity field very near a large arc. The problem is that very high accuracy is needed when $x_1 \simeq x$, while still maintaining reasonable accuracy elsewhere. This

difficulty can be overcome by dividing the interval of integration into three sub-intervals and using a different form of Eq. (8) in each sub-interval. Fortunately, this can be done in a fairly simple and efficient manner, as described later.

For the moment, substitute Eq. (8) into Eq. (7) to obtain

$$r_v^3 = \{(1 - 2\varepsilon y + \varepsilon^2 F_2)x_1^2 + (-2x + \varepsilon^2 F_1)x_1 + (x^2 + y^2 + z^2 + \varepsilon^2 F_o)\}^{3/2} \tag{9}$$

The possibility of a variation in circulation along the arc length will be modelled by including a linear dependence on x_1 , namely

$$\Gamma(x_1) = \Gamma_o + \Gamma_1 x_1 \tag{10}$$

Then the numerator of Eq. (13) is given by

$$\Gamma(x_1)\vec{r}_v \times d\vec{s} = (-2\varepsilon\Gamma_o z x_1 - 2\varepsilon\Gamma_1 z x_1^2)dx_1\vec{i} + (\Gamma_o z + \Gamma_1 z x_1)dx_1\vec{j} + (-y\Gamma_o + [2\varepsilon\Gamma_o x - y\Gamma_1]x_1 + [2\varepsilon\Gamma_1 x - \varepsilon\Gamma_o]x_1^2 - \varepsilon\Gamma_1 x_1^3)dx_1\vec{k} \tag{11}$$

Since Eq. (11) involves only integer powers of x_1 , and since Eq. (9) contains only a quadratic in x_1 , all integrals required to evaluate Eq. (3) have the form

$$I_n = \int \frac{x_1^n}{[cx_1^2 + bx_1 + a]^{3/2}} dx_1 \tag{12}$$

Here a , b , and c are the coefficients of the quadratic in x_1 in Eq. (9). The integrals I_n are available in integral tables for the first few values of n , and for larger n they can be found using integration by parts. Appendix A gives the value of this integral for the values $n = 0,1,2,3$ which are of interest to the present work, and mentions other considerations for accurate numerical evaluation.

Defining the velocity components as $\vec{q} = u\vec{i} + v\vec{j} + w\vec{k}$, the evaluation of Eq. (3) yields the following results:

$$u = \frac{\varepsilon\Gamma_o z}{2\pi} I_1 \Big|_{arc} + \frac{\varepsilon\Gamma_1 z}{2\pi} I_2 \Big|_{arc} \tag{13}$$

$$v = -\frac{\Gamma_o z}{4\pi} I_o \Big|_{arc} - \frac{\Gamma_1 z}{4\pi} I_1 \Big|_{arc} \tag{14}$$

$$w = \frac{y\Gamma_o}{4\pi} I_o \Big|_{arc} - \frac{[2\varepsilon\Gamma_o x - y\Gamma_1]}{4\pi} I_1 \Big|_{arc} - \frac{[2\varepsilon\Gamma_1 x - \varepsilon\Gamma_o]}{4\pi} I_2 \Big|_{arc} + \frac{\varepsilon\Gamma_1}{4\pi} I_3 \Big|_{arc} \tag{15}$$

Here the notation $I_n\big|_{arc}$ has been used to indicate integration over the arc. This integration is done in two different ways depending on the distance from the point of evaluation to the closest point on the arc. If this distance exceeds approximately 1.5ℓ , the quadratic model of $\varepsilon^2 x_1^4$ can be neglected ($F_o = F_1 = F_2 = 0$) with an error of less than 1%. The integral is then evaluated at the arc end points, namely $I_n\big|_{arc} = I_n\big|_{-\ell}^{+\ell}$. This simplification reduces the computer time to evaluate a vortex element contribution by about a factor of 2. In an actual free wake calculation, the majority of integral evaluations are of this simpler type. If the distance

from the arc is less than approximately 1.5ℓ , the integral evaluation is done as described below. In practice, the distance from the arc is estimated by testing to see if the distance from the midpoint or either end point exceeds 1.5ℓ .

At points close to the arc the piecewise quadratic model of the term $\varepsilon^2 x^4$ is used. The integration over the arc actually is done in three sub-intervals, with different values of a, b, and c in Eq. (12). This is due to the different values of F_o , F_1 and F_2 in the quadratic model for each sub-interval. The interval of integration is subdivided as follows:

$$I_n\Big|_{arc} = I_n(M_-)\Big|_{-\ell}^{-d(x)} + I_n(M_o)\Big|_{-d(x)}^{d(x)} + I_n(M_+)\Big|_{d(x)}^{\ell} \qquad (16)$$

Here $\ell = R_o \sin(\theta_o/2)$ is half the distance between the ends of the arc shown in Figures 1 and 2. The sub-interval end points at $\pm d(x)$ adapt to the value of x . The notation M_- , M_o , M_+ denotes the choices of the model for $\varepsilon^2 x^4$ given by Eq. (8) in each sub-interval. This sub-interval modelling procedure is now explained in more detail.

It is necessary to have $M(x,x_1)$ model the term $\varepsilon^2 x_1^4$ very accurately when $x_1 \simeq x$ and $-\ell < x < \ell$, since at this point the rest of the terms in Eq. (7) are near a minimum. The model should give the correct value at $x_1 = x$ and match, or at least nearly match, the local slope. At points away from $x_1 = x$, it is not the absolute accuracy of $M(x,x_1)$ that is important, but rather the size of the error relative to the quantity $(x - x_1)^2$, which is the largest term in Eq. (7) (if regrouped). The choice of a model which will provide sufficient accuracy is not unique, and the approach given below was chosen for its relative simplicity as well as its accuracy. Based on Eq. (7), define

$$M_{\pm}(x,x_1) = F_o(x) \mp F_1(x)x_1 + F_2(x)x_1^2 \qquad (17)$$

where good results are obtained using

$$F_o(x) = h(x)^4 + \ell^2 h(x)^2 \tag{18a}$$

$$F_1(x) = 4h(x)^3 + 2\ell^2 h(x) \tag{18b}$$

$$F_2(x) = 4h(x)^2 + \ell^2 \tag{18c}$$

with

$$h(x) \equiv \begin{cases} \alpha\ell & x \leq \alpha\ell \\ |x| & \alpha\ell \leq x \leq \ell \\ \ell & x \geq \ell \end{cases} \tag{19}$$

Here $M_{\pm}(x,x_1)$ is used in the sub-interval integrations denoted by Eq. (16), along with the end point location

$$d(x) = \alpha\ell + \beta[h(x) - \alpha\ell] \tag{20}$$

Good choices of the constants are $\alpha = 0.3$ and $\beta = 0.4$, so that $0.3\ell \leq d \leq 0.58\ell$. Finally, for the middle interval in Eq. (16)

$$M_o(x,x_1) \equiv 0 \tag{21}$$

The effect of Eqs. (17) through (21) is now explained. Figure 3 shows the piecewise parabolic model of $\varepsilon^2 x_1^4$ for three cases. The model always fits well around $x_1 = x$ and the errors near the discontinuities at $x_1 = \pm d$ largely cancel when the integration is actually performed. When $x \leq d$ or $x \geq \ell$, the parabolas are frozen in the positions shown for $x = 0.3$ and

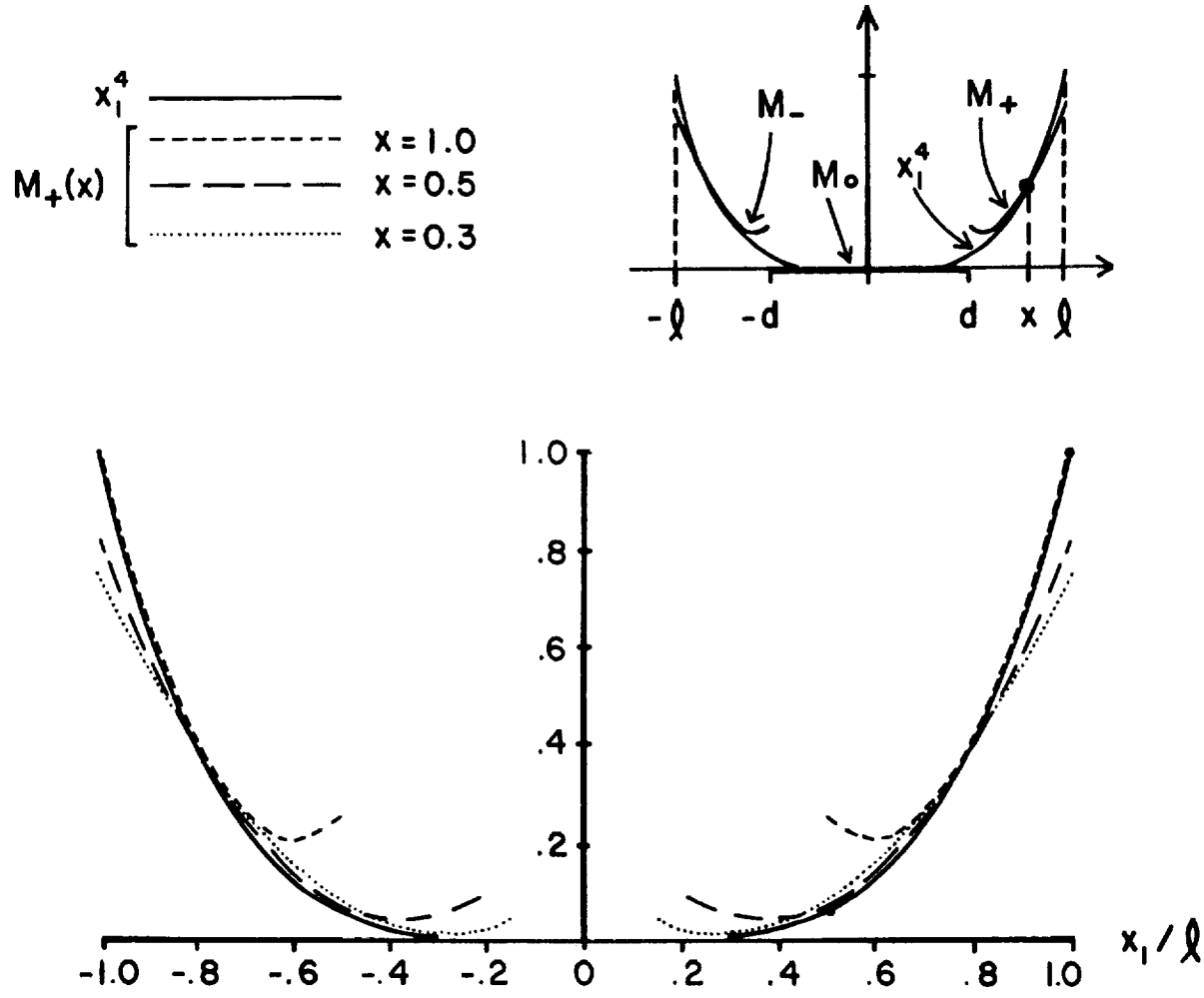

Figure 3. Piecewise quadratic model of $\varepsilon^2 x_1^4$ used in the Biot-Savart integration for the BCVE.

x = 1.0, respectively. The model is always symmetric, so for negative x a mirror image of Figure 3 would be obtained. Implementing this approach allows the Biot-Savart law to be evaluated to good accuracy for a parabolic arc. A detailed study of the accuracy of the BCVE is found in Section 3.

2.1.2 The Self-Induction Vortex Element (SIVE)

The geometry for the derivation of the Self-Induction Vortex Element, SIVE, is shown in Figure 4. A circular arc is passed through the three collocation points j-1 , j and j+1 for the purpose of evaluating the self-induced velocity at the center point j . The Biot-Savart integral must be stopped at a cut-off distance d_c on either side of j to avoid a logarithmic singularity in the velocity field. Previous work has shown how the cut-off distance should be chosen to give the correct answer.[17-19] Using the properly chosen cut-off distance is equivalent to having used the method of matched asymptotic expansions to match an inner solution for a curved rotational vortex core to an outer solution generated by the Biot-Savart integration over the vortex filament.

The cut-off distance expressed in terms of the vortex core radius, a , is given by

$$d_c = \frac{a_c}{2} e^{-(A - C - \frac{1}{2})} \tag{22}$$

where the constants A and C are related to the kinetic energy in the vortex core associated with the swirl and axial velocity components, respectively. In general

$$A = \lim_{\bar{r}\to\infty} \left[\int_0^{\bar{r}} \bar{r}\, v_o^2 d\bar{r} - \ln\bar{r} \right] \tag{23}$$

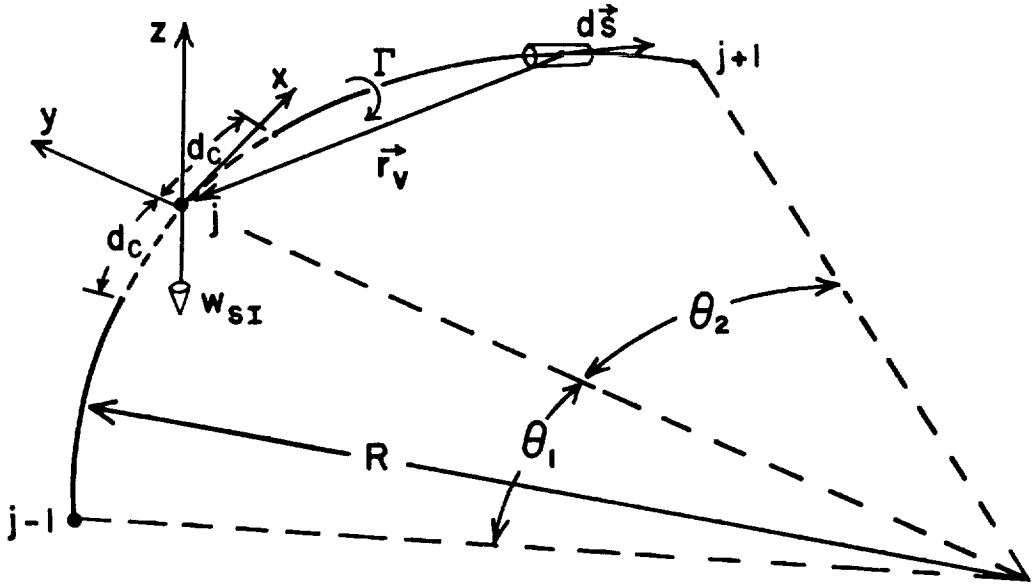

Figure 4. Geometry for the Biot-Savart integration to determine the self-induced velocity for the SIVE.

where $\bar{r} = r/a_c$, and $v_o(\bar{r})$ is the swirl velocity distribution in the vortex core nondimensionalized by $\Gamma/2\pi a_c$. Similarly, if $w_o(\bar{r})$ is the axial velocity distribution nondimensionalized by $\Gamma/2\pi a_c$,

$$C = \int_0^\infty 2\bar{r}w_o^2 d\bar{r} \tag{24}$$

It is of interest to give the value of A for two swirl velocity distributions of interest. For a constant vorticity core (solid body rotation) a simple calculation gives $A = 0.25$. For a "decaying" vortex core based on the similarity solution for viscous diffusion of a point vortex (here $a_c = \sqrt{4\nu t}$), a more difficult calculation gives $A = -0.058$. Typically, C will also be a number of order unity or smaller. The important conclusion is that the cut-off distance given in Eq. (22) is roughly the same order as the vortex core radius.

The Biot-Savart integral over the curved arc in Figure 4 is done most conveniently in polar coordinates. When the point of evaluation is on the arc itself, it is possible to do the integration analytically. The details of the calculation are omitted since it is staightforward and a similar approach has been used in other published work. The result shows that the induced velocity is normal to the plane of the arc and is given by

$$w_{SI} = -\frac{\Gamma}{4\pi R}\ln\frac{4R}{d_c} - \frac{\Gamma}{8\pi R}\ln\left[\left(\tan\frac{\theta_1}{4}\right)\left(\tan\frac{\theta_2}{4}\right)\right] \tag{25}$$

In this result, terms of order $(d_c/R)^2$ have been neglected in deriving the first term on the right side. This approximation is consistent with the accuracy of the analysis underlying the derivation of the cut-off distance formula.

2.2 Element Connection Procedure

A special procedure is required to connect curved vortex elements to form a wake. A similar problem does not arise for straight-line elements, since every two connection points uniquely determine the length and orientation of a straight-line segment. One way to locate a curved element is to specify two end points and a third point along the arc. There are other possibilities as well, such as the specification of two end points and one end point tangent vector. In any event, there are several ways to generate a connection scheme given a set of collocation points through which the arc must pass.

The first issue to be faced is whether the wake shape is to be fitted in a local or a global manner. An example of the global approach is to first fit all the collocation points at once using a high order polynomial curve fit or a spline method with strong continuity conditions between the spline segments. The curve fit can then be used segment-by-segment to calculate the appropriate length, curvature, and orientation of the curved vortex elements to be placed between the collocation points. There is at least one strong objection to the global approach. If a disturbance or shape change is introduced in one part of a wake, it will have some effect on the wake shape everywhere else due to the global nature of the curve fit. Part of this effect on other parts of the wake will come from changes in the Biot-Savart integration, as it should, but another part will come from the curve-fit procedure itself, which has no real physical basis in the fluid mechanics of the wake. This difficulty argues strongly for the use of an element connection procedure which is based on (relatively) local information.

Figures 5a, b and c show three methods of locating and connecting vortex elements based on the three point method of locating arcs. It should be stressed that this discussion applies primarily to the BCVE, namely to the location of elements not passing through the point where the velocity is being evaluated. The method of locating the SIVE, which must be compatible with the BCVE location method, will be explained later.

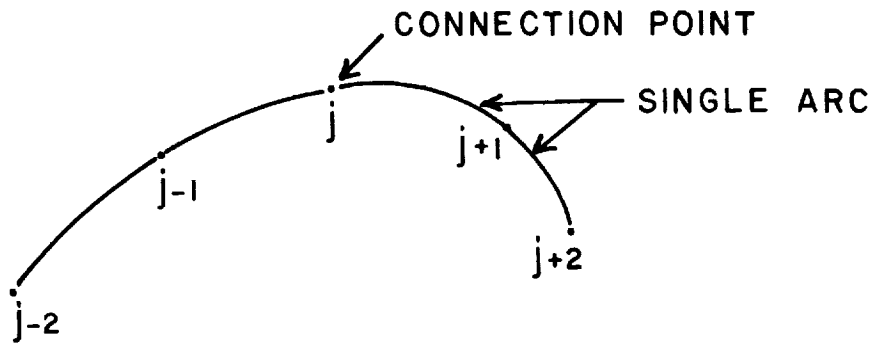

a.) END-TO-END CONNECTION METHOD

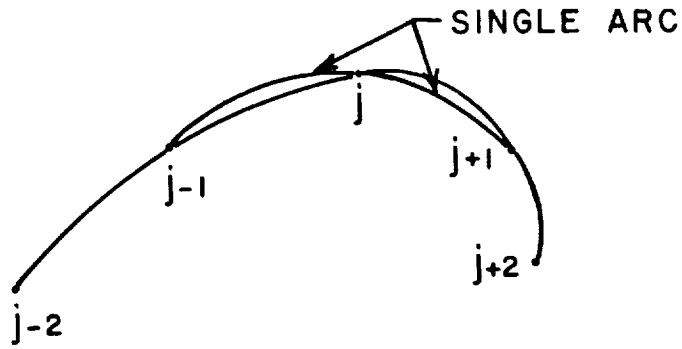

b.) OVERLAPPING ARCS METHOD

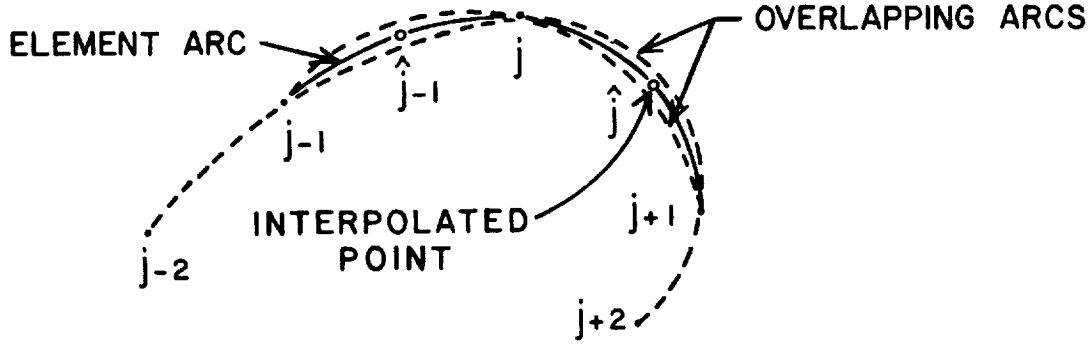

c.) INTERPOLATED POINT METHOD

Figure 5. Connection methods for curved vortex elements.

Figure 5a shows the end-to-end method of connecting arcs. Arcs are passed through each set of three points and touch end-to-end. The advantage of this method is that it uses the least number of arcs to span a given number of collocation points. Note that half as many arcs as straight line segments are required. One disadvantage is that fairly long elements must be used since two intervals (3 points) must be spanned. This may lead to some loss of accuracy since larger elements are somewhat less accurate, especially if the velocity near the element is needed. A stronger criticism is that while the method does a good job predicting the curvature near points $j-1$ and $j+1$, it behaves as if the curvature at point j is the average curvature of the two butted arcs. A much better estimate of the curvature at point j is obtained by passing an arc through the three points $j-1$, j and $j+1$. It is possible to construct examples in which this method would even predict the wrong sign for curvature at point j. Usually, such cases would occur in practice only if too few collocation points are used to model the wake.

Figure 5b shows the overlap method of connecting arcs. Each overlapped arc is of half strength. The approach effectively averages the position and curvature of the vortex based on the location of the four nearest points. Because each arc spans two intervals, the number of arc calculations equals the number of intervals, even though there are two arcs in each interval. Again, a disadvantage of this method is that long arcs are still needed. Another disadvantage is that the effective averaging that results from overlapping the elements may break down if the local wake configuration is very nonplanar, if successive interval sizes vary considerably, or if the curvature is changing rapidly. These conditions may lead to situations where the overlapped elements are not sufficiently close to each other to provide a credible average.

Figure 5c shows the interpolated point method, which has been chosen as the preferred connection scheme for the present work. An intermediate point is computed within each interval between collocation points. For example, the location of the point $\hat{j}$ between j and $j+1$ is interpolated based on the average properties (curvature and orientation) of the arcs passed through point sets $j-1$, j, $j+1$ and j, $j+1$, $j+2$. A curved vortex element is

then located to pass through the set of points j , $\hat{j}$, $j+1$. The properties of the element arc thus reflect the consistent use of information from the location of the four nearest points. An advantage of this method is that the arc length of the elements can be relatively short since only one interval between points is spanned by each arc. This approach is also not subject to the other possible disadvantages of overlapping, since only a single arc is used in each interval. A disadvantage of the method is that some additional complexity is required to locate each interpolated point. In addition, at each point where two arcs meet there will be a discontinuity in slope and curvature. However, the average effect seen in the nearby velocity field will be essentially correct, since curvature information from both sides of the connecting point is used for each of the arcs.

Residual discontinuities in slope and curvature are inevitable with any simple arc element model. They could be removed by using a higher order element model, e.g., an arc with torsion and linearly varying radius of curvature, with slope and curvature continuity conditions at the end points. However, these refinements are judged to be not worthwhile for current purposes. If connection point discontinuities are a problem, it is better to increase the number of collocation points in the wake to allow for a smoother fit. Including more points directly adds more real information about the wake shape than can be obtained by further refining the element model. However, the reason for using a curved element at all is that it makes the best use of the information available locally in a set of collocation points. Ultimately, an adequate number of collocation points must be determined based on the resulting smoothness of the wake, and their effect on the convergence properties of the solution. The optimum spacing of these points will not necessarily be uniform, with certain critical regions requiring higher point density (e.g., blade/vortex interactions) and other regions requiring very few points (e.g., the far wake). A more detailed study of the accuracy of fitting elements to a set of collocation points is found in Section 3.

To calculate the velocity at a collocation point in the wake requires that the self-induction vortex element, SIVE, also be used. As discussed earlier, the element shape is a circular arc passed through three collocation points.

The SIVE gives the velocity at the intermediate collocation point between the two end points. As shown in Figure 6, if the velocity is desired at point j, the SIVE spans the point set $j-1$, j, $j+1$ while the other points are spanned by BCVE's located by the interpolated point method. When the velocity is evaluated at a different collocation point the element patterns must be shifted accordingly. If the point of evaluation were not on the filament, then the SIVE shown in Figure 6 would be replaced by two BCVE's. If straight-line elements were used instead, then every BCVE would be replaced by a straight-line element.

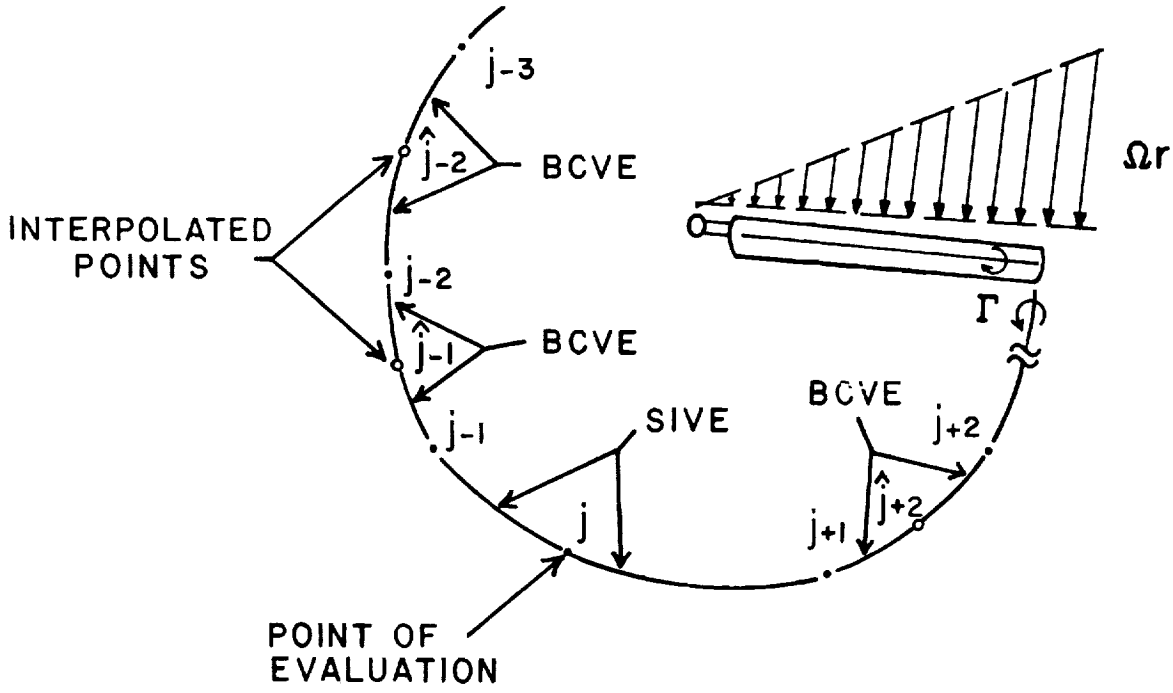

Figure 6. Typical arrangement of elements to calculate the self-induced velocity at point j .

3. ACCURACY AND CALCULATION TIME

3.1 Overview of Accuracy and Time Issues

The use of Basic Curved Vortex Elements (BCVE's) to model the tip vortex in helicopter free-wake calculations is described in the previous section and in Ref 13. This approach replaces the usual straight-line vortex elements with curved vortex elements. Because of their curvature, these elements provide a more natural geometric fit for the wake shape. There are two benefits to this approach, both of which derive from the significant improvement in fitting accuracy. First, the curved elements allow more accurate calculation of the velocity field at points near the vortex filament. This accuracy is an important issue in a rotor wake because successive turns of the curved tip vortex are often in close proximity. The second benefit is that much larger elements can be used. Since free-wake calculation time depends strongly on the number of elements (as explained later), reducing the number of elements has a strong effect on the calculation efficiency. However, there is also a penalty associated with the use of curved elements. Because the curved element model involves an increase in analytical complexity, the computer time to do individual element calculations is increased, and this increase partially offsets the benefit of fewer elements.

The purpose of this section is to give a relatively complete picture of the velocity field accuracy and calculation time of curved elements. Comparison is made to the straight-line element method, and therefore considerable information is provided about the performance of this more traditional approach. This information should be useful in assessing the accuracy of calculations done by either method. One qualification in the comparisons to be made should be stated clearly. The results for curved elements are based on their current level of optimization. Because this approach was developed only quite recently, future significant improvements in efficiency are quite possible. Nevertheless, the curved elements perform extremely well in their current form.

It should be noted that other researchers[9-11] have also recognized the need to account for filament curvature to improve accuracy, at least for the wake of a rotor in hover. The methods employed involve local curvature correction procedures to the straight-line element method. The present approach addresses the accuracy problem through the development of a curved element for general use.

3.2 Numerical Evaluation of the Biot-Savart Integral

The central problem in free-wake analysis is to calculate the effect of the tip vortex accurately and efficiently. Since this must be done numerically, the Biot-Savart integration has to be discretized in some manner. In principle, to obtain an accurate answer, the discretization distance along the vortex filament must be small compared to the minimum distance from the filament to the point of evaluation. Because it is sometimes necessary to determine the velocity at points very close to the filament, strict implementation of this condition would require a very large number of discrete elements. However, using such large numbers of elements would be prohibitive in terms of computation time. It is therefore necessary to keep the number of elements to a minimum and still try to maintain accuracy.

The Biot-Savart integral for the velocity field of a constant strength vortex filament is given by:

$$\vec{q} = -\frac{\Gamma}{4\pi} \int_C \frac{\vec{r}_v \times d\vec{s}}{r_v^3} \tag{26}$$

where $\vec{r}_v$ is the distance vector from the filament to the point of evaluation, and $d\vec{s}$ is the differential arc length vector tangent to the arc. In principle, this integral can be accurately evaluated along the filament contour by several numerical methods.

The most direct approach is the straightforward approximation of the integral by a summation of the form:

$$\vec{q} = -\frac{\Gamma}{4\pi} \sum_{i=1}^{N} \frac{\vec{r}_{v_i} \times \Delta\vec{s}_i}{r_{v_i}^3} = \sum_{i=1}^{N} \vec{q}_{D_i} \tag{27}$$

The velocity field due to one of the discrete elements in this summation is of the form:

$$\vec{q}_D = \frac{\Gamma}{4\pi r} \frac{r^2 \ell_s}{[x^2 + r^2]^{3/2}} \vec{e}_\theta \tag{28}$$

where $\ell_s = |\Delta s_i|$. This velocity is expressed in a local coordinate system centered on this element, as shown in Figure 7. Here r and x are coordinates in a cylindrical system, with the x-axis in the $\Delta\vec{s}$ direction. This treatment of the integral is expected to be accurate when $|r_{v_i}| >> |\Delta s_i|$, namely when $(x^2 + r^2)^{1/2} >> \ell_s$.

A somewhat more accurate approach is to approximate the curve shape by a series of straight-line segments, and then evaluate the integral exactly for this approximate shape. The errors associated with this approach are related only to the geometric approximation of the curve. The velocity field of a finite length vortex line can be evaluated exactly in closed form. Expressed in the same local coordinate system, the result is:

$$\vec{q}_{SL} = \frac{\Gamma}{4\pi r} \left\{ \frac{x + \frac{1}{2}\ell_s}{\sqrt{(x + \frac{1}{2}\ell_s)^2 + r^2}} - \frac{x - \frac{1}{2}\ell_s}{\sqrt{(x - \frac{1}{2}\ell_s)^2 + r^2}} \right\} \vec{e}_\theta \tag{29}$$

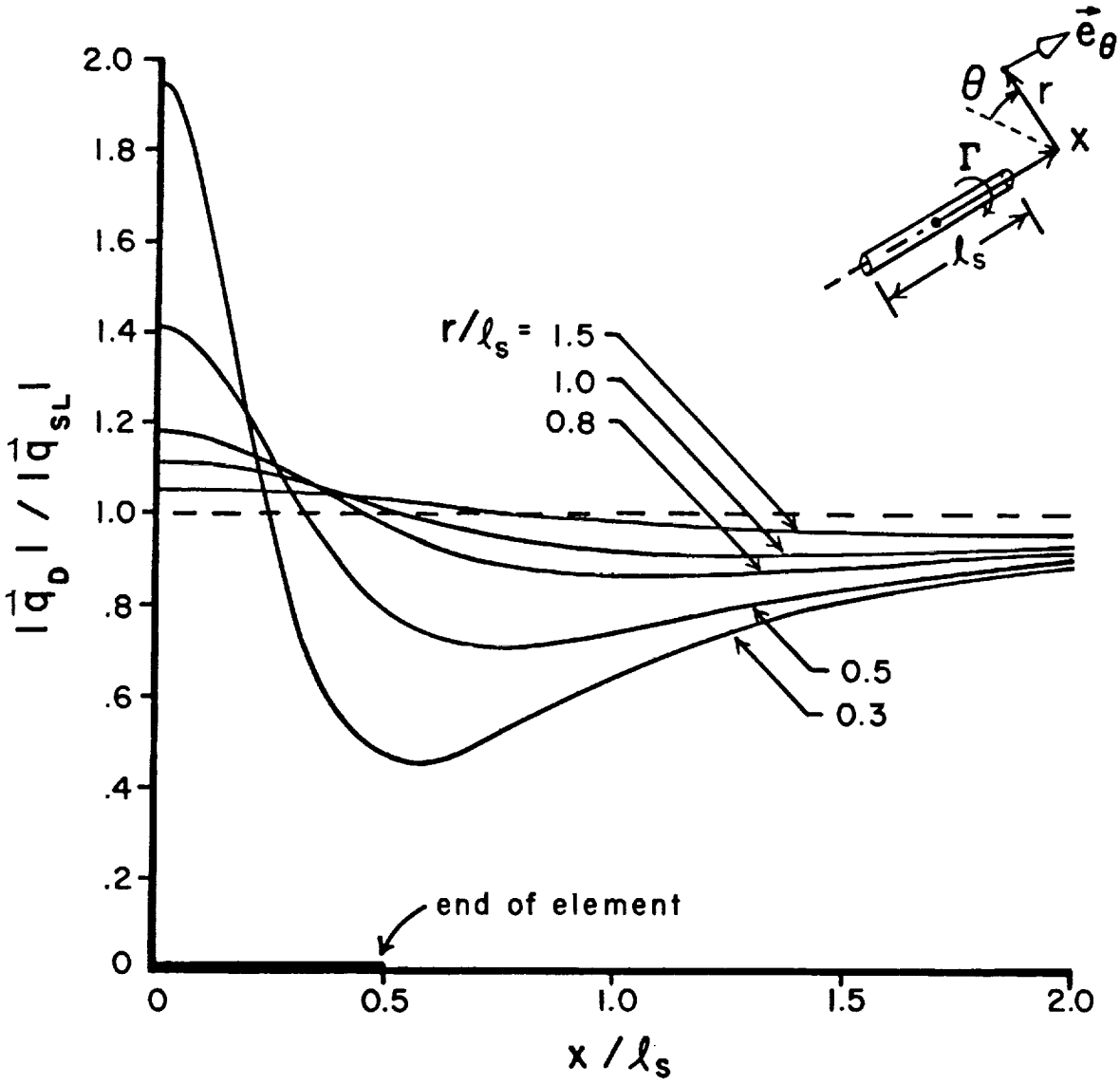

Figure 7. Ratio of velocity from a discretized Biot-Savart element to that of a straight-line element, shown as a function of position.

The contribution of the total vortex filament is then obtained by stringing together these straight-line elements to approximate the curve. This straight-line element approach has been used in many previous free-wake calculations. Its accuracy is one of the main concerns of this report.

It is of some interest to compare the accuracy of the approaches represented by Eqs. (28) and (29). Figure 7 shows the ratio of velocity magnitudes, $|\vec{q}_D|/|\vec{q}_{SL}|$, plotted versus location around a straight-line element. The error associated with using Eq. (28) is small (and rapidly decreasing) for radial distances in excess of about 1.5 element lengths. Because the element contributions fall off rapidly with increasing distance, the errors associated with large x/ℓ_s in Figure 7 are actually not very significant in absolute terms. It is clear that for distances not too close to the filament, the simple discretization of the Biot-Savart integral given in Eq. (27) works as well as the straight-line approximation. Comparing Eqs. (28) and (29) also shows that the functional form of Eq. (28) is somewhat simpler than Eq. (29). Although this might lead to a slight advantage in computational efficiency, the difference is probably not too significant. Nevertheless, the simple discretized element is certainly a viable option in some circumstances. In fact, its simple functional form allows an efficient way to sum the contribution from a semi-infinite array of vortex elements, and thus forms the basis for the forward flight far wake model described in Section 4.

Since the straight-line element is widely used, it is of primary importance to understand its performance. As mentioned, the use of straight-line elements constitutes a geometric approximation of the vortex curve. Reference 13 showed that straight-line elements introduce significant errors in the velocity field near a vortex ring (these results are reviewed in subsection 3.3). The errors associated with straight-line elements can be classified as position errors and curvature errors, see Figure 8. Position errors arise because the straight-line elements do not coincide with the filament position at most points along the curve. The size of the position error depends on the local element displacement, δ_s , as compared to the distance, r , from the filament. Curvature errors arise from the failure to

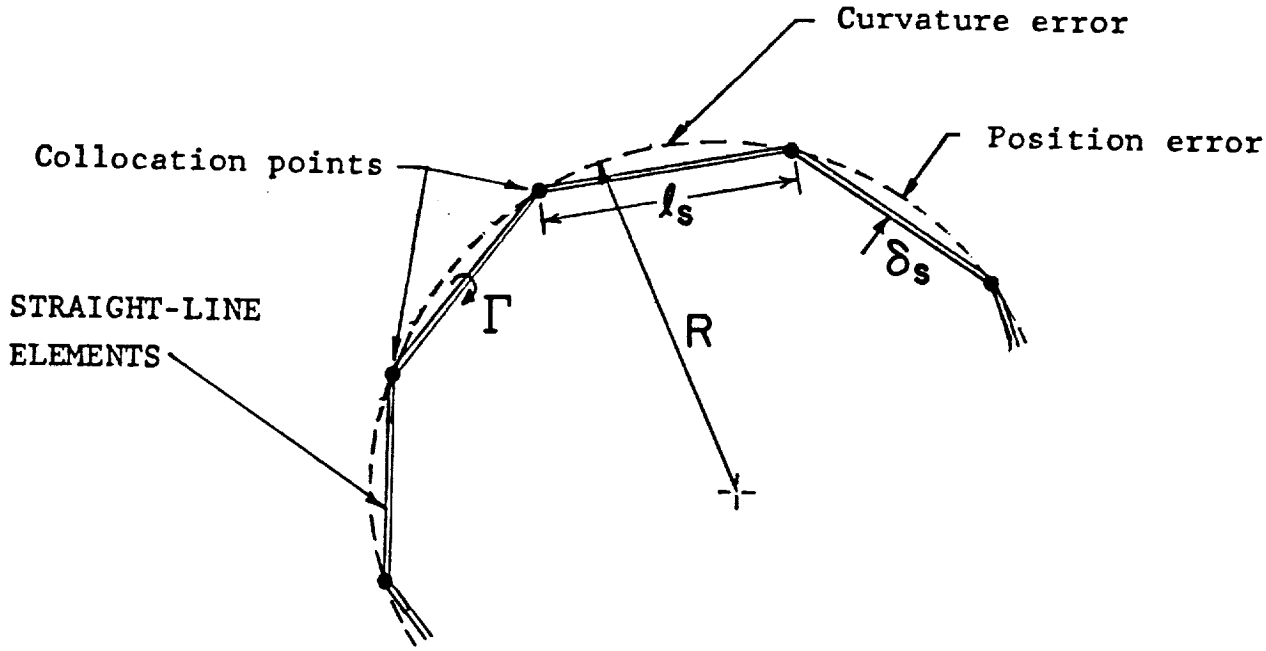

Figure 8. Types of geometric errors for straight-line elements.

duplicate the local curvature of the filament. The analytical solution for the velocity field near a curved vortex filament shows that the local curvature introduces a velocity normal to the plane of the arc. For a finite strength filament of infinitesimal cross-section this velocity component depends logarithmically on r, see References 18 and 19. This local curvature effect is not simulated at all by individual straight-line elements because they are not curved. Therefore, the curvature error is present to some extent everywhere on a filament modelled by straight-line segments. The position error varies along the filament, being insignificant at the collocation points where the straight-line elements coincide with the curved filament, and reaching a maximum in between. Typically, position errors are larger than curvature errors. The results of a detailed study of the errors associated with using straight-line elements are presented in later subsections.

It is possible to consider more sophisticated vortex elements than the simple discretized element of Eq. (28) or the straight-line element of Eq. (29). The next level of sophistication is to introduce curvature into the element in order to improve its fitting accuracy. The Basic Curved Vortex Element (BCVE) described in detail in Section 2 of this report represents this next level of refinement. The trade-off that must be considered is the increase in analytical complexity of the element versus the potential improvement in fitting accuracy. From an efficiency standpoint, a more complex element must be capable of offering a sufficient improvement in accuracy such that fewer elements of larger size can be used. In a free wake calculation the pay-off from using fewer elements is capable of off-setting the penalty associated with the increase in complexity of individual elements.

The computer time and accuracy of curved versus straight-line elements will be dealt with in detail later. However, the fact that curved elements are capable of a dramatically better geometric fit can be readily demonstrated. To demonstrate this point the relative ability of these elements to fit a circular arc will be considered. Referring to Figure 8, a simple calculation shows that the ratio of maximum position error to local radius of curvature for straight-line elements is

$$\frac{\delta_s}{R} \approx \frac{1}{2}\left(\frac{\ell_s}{2R}\right)^2 \approx 0.125\left(\frac{\ell_s}{R}\right)^2 \tag{30}$$

where to obtain a simple expression it has been assumed that $\ell_s/2R \ll 1$. For comparison, the BCVE has a parabolic shape touching the arc at the midpoint and end points as was shown in Figure 1. The total length spanned by a curved element is denoted by $\ell_c = 2\ell$ in Figure 1. Again, assuming $\ell_c/2R \ll 1$, it is possible to show that for the BCVE

$$\frac{\delta_c}{R} \approx \frac{3}{8.16}\left(\frac{\ell_c}{2R}\right)^4 \approx .00146\left(\frac{\ell_c}{R}\right)^4 \tag{31}$$

The maximum fitting error, δ_c, for the BCVE occurs at the quarterpoints, halfway between the midpoint and end points.

Clearly, the BCVE makes much smaller fitting errors, and these errors decrease much more rapidly with decreasing element size. For equal element size, $\ell_c = \ell_s$, the ratio of fitting errors is

$$\frac{\delta_c}{\delta_s} \approx .012\left(\frac{\ell_c}{R}\right)^2 \qquad \text{(equal size)} \tag{32}$$

As explained later, it is necessary to keep $\ell_c < R$. Clearly, the fitting error associated with using curved elements is very small; in fact it is about two orders of magnitude below that of straight-line elements. It is also interesting to see how large a curved element must be for equal fitting error, namely if $\delta_c = \delta_s$. The ratio of element lengths for equal error is

$$\frac{\ell_c}{\ell_s} \approx 9.2\left(\frac{R}{\ell_c}\right) \qquad \text{(equal error)} \tag{33}$$

which shows that a curved element can be about an order of magnitude larger

than a straight-line element for the same fitting error. Considering Eqs. (32) and (33) together, it is clear that a balance can be achieved in which larger curved elements are used but the fitting error still remains very small in comparison to that of straight-line elements.

The process of predicting the shape of a curve based on a set of collocation points contains certain implicit assumptions. The primary assumption is that the curve is smooth and changes only gradually over the separation distance between the collocation points. In practice, this means that the local radius of curvature must be larger than the local separation distance between collocation points. The radius of curvature can be estimated by passing an arc through each set of three collocation points. Figure 9a shows that when points are positioned such that the estimated radius of curvature exceeds the spacing between the points, there is no longer a rational basis for choosing one smooth curve through these points over another, even though the curves may differ considerably. However, when the radius of curvature exceeds the point spacing, as in Figure 9b, the location of the curve passing between these points can be estimated within a narrow latitude. An estimate of this latitude is the degree of overlap between arcs passed through adjacent sets of three points. Curved elements using the interpolated point method naturally fall within this range, but straight-line elements almost always fall outside it.

From the standpoint of using curved elements, the fundamental geometric limitation is the ratio of element size to local radius of curvature. When $\ell_c/R > 1$, the possibility of choosing the right curved element shape is lost, as indicated in Figure 9. However, when $\ell_c/R < 1$ the fitting accuracy will generally improve rapidly, as indicated by Eq. (31).

It is important to point out that the limitation on element size should not be considered entirely from a geometric point of view. It is not always known in advance what element size is appropriate for a given calculation. Using elements that are too large will filter out some of the finer structure in the vortex filament shape. This may or may not be important depending on what quantities are to be calculated, and what is deemed an acceptable trade-

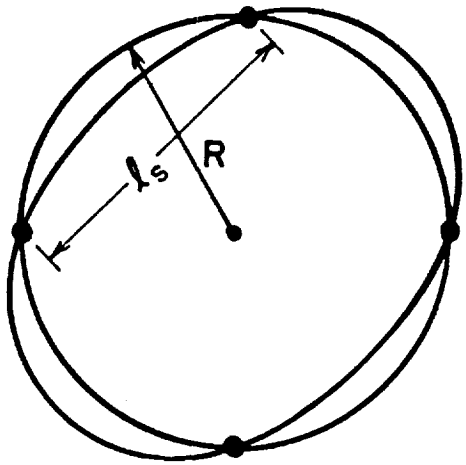

a) Point spacing greater than radius of curvature. Many different smooth curves can pass through these four points .

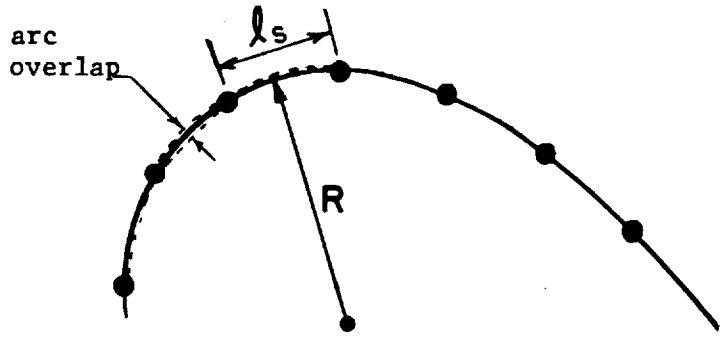

b) Point spacing less than radius curvature. The desired curve is defined within a narrow range .

Figure 9. Curve fitting accuracy as a function of the ratio of point separation to radius of curvature.

off between accuracy and efficiency. Furthermore, there may be considerable stretching and distortion in some portions of the flow, causing the ratio of element length to radius of curvature to change significantly. Thus, the choice of element size depends on a number of issues related to the particular problem to be solved.

3.3 Accuracy of Curved Vortex Elements

This subsection describes the calculated results used to assess the accuracy of the basic curved vortex element, BCVE, as compared to straight-line elements. The emphasis is on the accuracy of the new BCVE, since self-induction elements like the SIVE have been used previously. Although the calculated results necessarily deal with specific vortex filament configurations, the analytical work presented in the next subsection shows the same conclusions apply to arbitrary filament shapes.

The first issue is the accuracy of the Biot-Savart integration procedure for a parabolic arc. This is a concern because it was necessary to model one of the terms in the integral in order to perform the integration analytically. The correct answer for a parabolic arc can be obtained numerically by dividing the arc into so many small curved elements that the calculated result becomes independent of the number of elements used. This result can be used to establish the accuracy of a single BCVE corresponding to the same parabolic arc shape. As expected, the errors are found to increase as the arc size increases and as the distance from the arc decreases.

It is sufficient to present some results for the extreme case of a parabolic arc corresponding to $\theta_o = 90°$, see Figure 10. At the point a distance $z = 0.1R$ directly above the arc, the error in any of the three velocity components is at most a few percent. For the corresponding results at $z = 0.3R$, the errors are well under 1%. Although this level of accuracy is already very good, reducing the arc to a more realistic size causes a strong reduction in the error. This reduction occurs because the relative importance of the modelled term in the BCVE analysis increases as the square

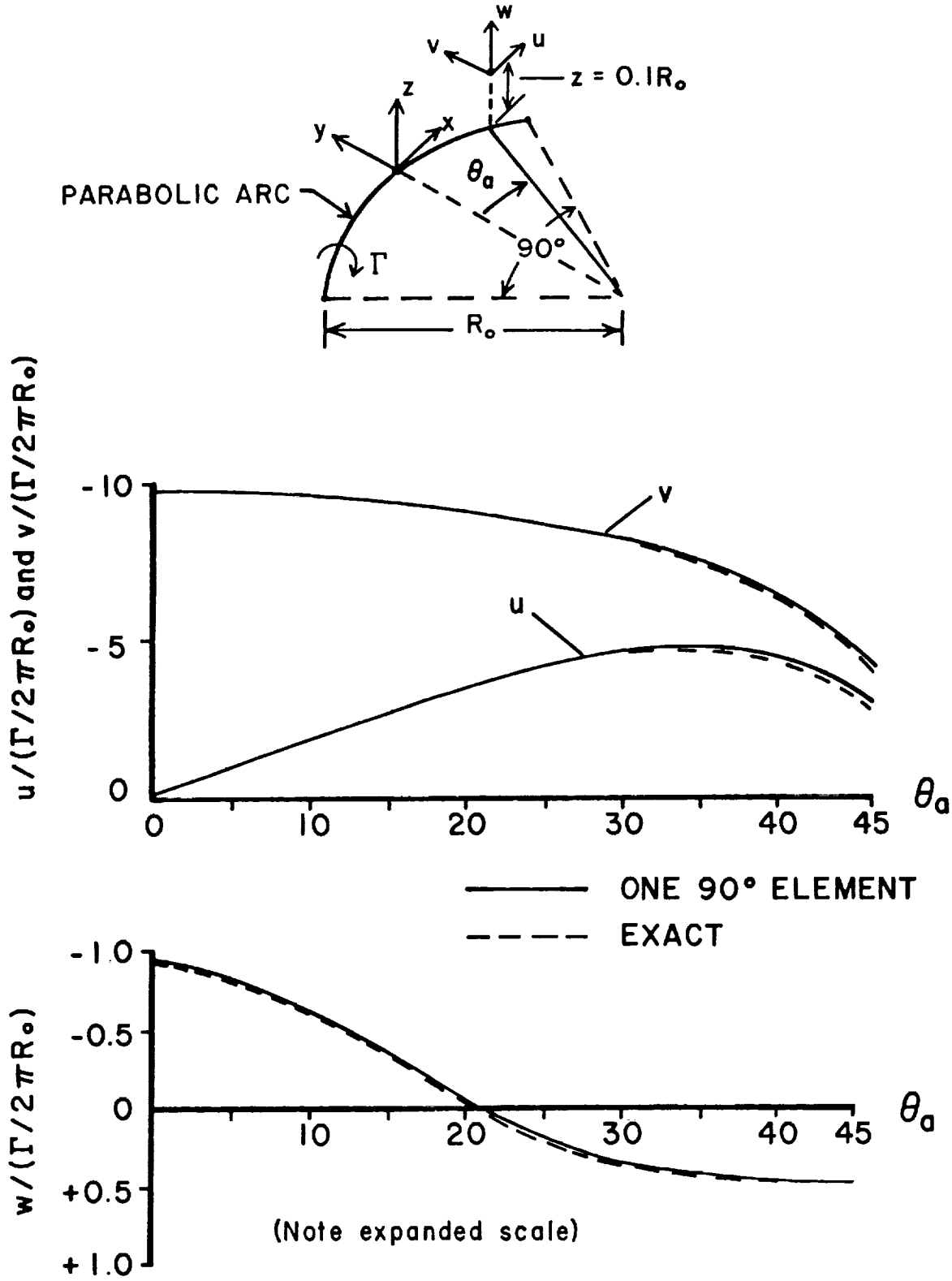

Figure 10. Comparison of predicted and exact velocity components above a parabolic arc as a function of position along the arc.

of the arc size. It is concluded that the integration procedure used for parabolic arcs introduces negligible errors.

Having established that the BCVE can represent a parabolic vortex filament very accurately, it is next important to see how accurately these elements can represent the velocity field of other vortex shapes. The vortex ring provides a simple test case.* Figures 11 and 12 show calculations of the velocity, w, normal to the plane of the ring at different distances directly above the vortex itself. The results are shown as a function of azimuthal angle, θ, for different numbers of BCVE's and straight-line elements. The correct answer is independent of θ. For any number of elements of either type the accuracy improves rapidly with increasing distance from the vortex. In all cases, relatively few curved elements are superior to many more straight-line elements. Note that only 4, 6 and 8 curved elements are compared with 8, 12 and 24 straight-line elements.

Looking first at the curved arc element results, the errors for small z can be attributed to two effects: position errors and curvature errors. The parabolic elements lie directly below the point of evaluation only at the points where the parabolic arcs and circular ring coincide. For instance, this occurs every 45° for the 4 element ring, and the error is seen to be a minimum at $\theta = 0$ and $\theta = 45°$, the arc end point and midpoint, respectively. The residual errors at these points are due largely to the local variation of curvature along the parabolic arc, which is particularly important near the ring. The maximum error occurs in between and is a combination of curvature and displacement errors. The maximum displacement errors occur near the arc quarterpoints. The analytical solution for the velocity field near a vortex ring filament shows that the normal velocity, w, depends on the radius of curvature. At $\theta = 0$ (an end point) the parabolic

* The analysis presented in the next subsection considers straight-line element errors on filaments of arbitrary shape. This analysis shows that velocity errors of the type encountered in the vortex ring test case also occur for general filament shapes.

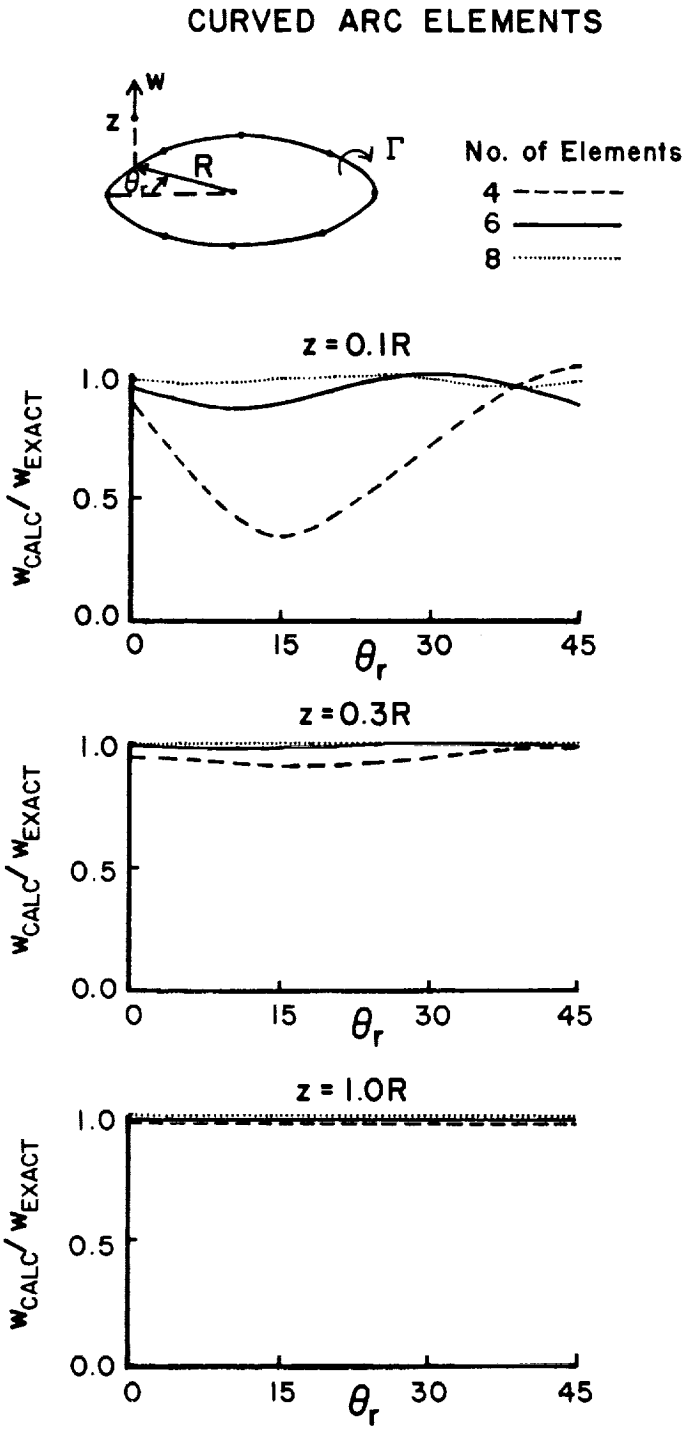

Figure 11. Normal velocity error above a vortex ring as a function of distance, azimuthal angle and number of elements - CURVED ELEMENTS.

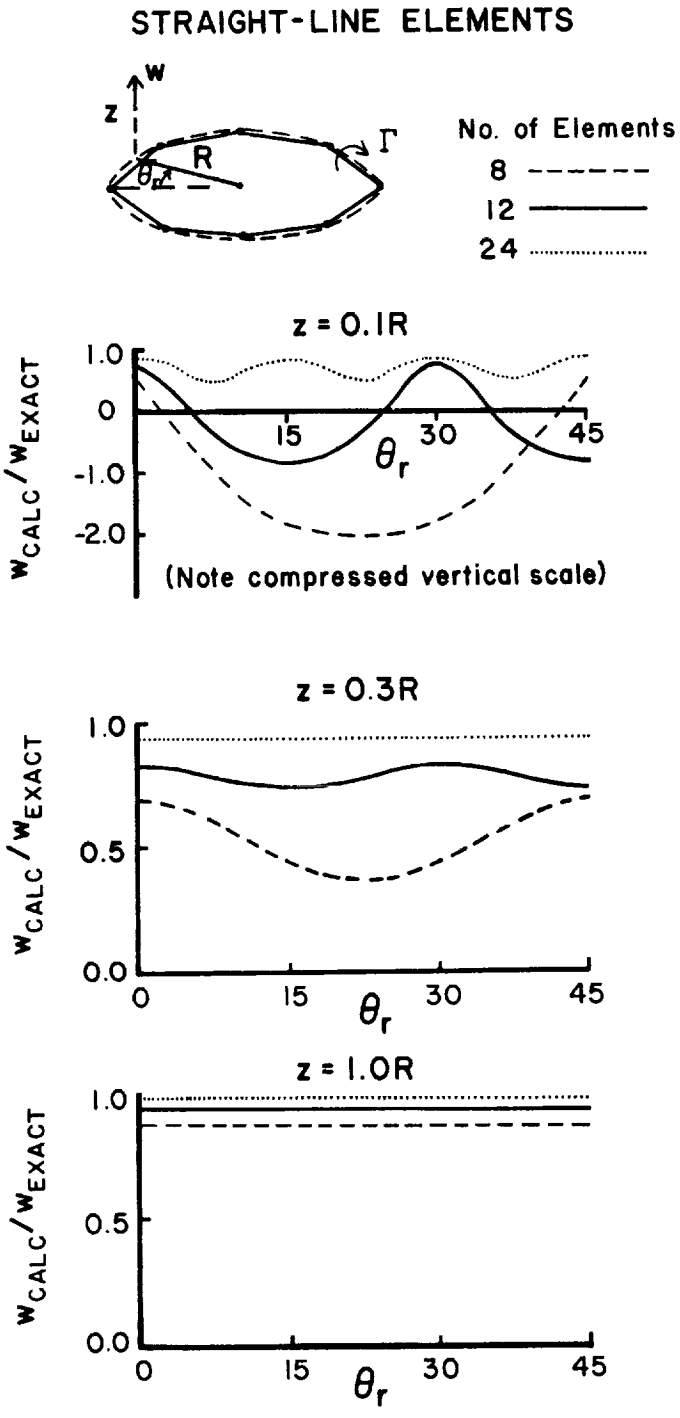

Figure 12. Normal velocity error above a vortex ring as a function of distance, azimuthal angle and number of elements - STRAIGHT-LINE ELEMENTS.

arc overestimates the radius of curvature and underestimates w, whereas at $\theta = 45°$ (a midpoint) the radius of curvature is underestimated and w is overestimated. The figures show that increasing the number of curved elements rapidly reduces both position and curvature errors. It should also be noted that the 4 element ring is presented as a limiting case. Because the element length exceeds the radius of curvature, the basic condition for accurate fitting ($\ell_c/R < 1$) is actually not satisfied.

In comparison, the ring made of straight-line elements* shows much worse errors, particularly near the ring, see Figure 12. Position errors are naturally much larger for straight-line segments. Curvature errors are severe, because the only simulation of curvature comes from the change in orientation from segment to segment. In fact, the portion of the normal velocity induced by local curvature, found in the analytical solution described later, is not simulated at all when straight-line segments are used. As a general rule, the distance from the ring must be somewhat greater than a straight-line element length in order to obtain accurate results. The pronounced azimuthal variation seen in the straight-line element velocity field raises a special concern. In a rotor wake, where successive turns of the vortex may be closely stacked, these azimuthal variations may produce spurious distortions and instabilities in neighboring turns. This possibility is seen to be much less likely for curved elements, even if many fewer curved elements are used.

Figure 13 shows the radial variation of the normal velocity, w, at a fixed distance above a vortex ring composed of either four BCVE's or eight straight-line segments. The effect of two azimuthal positions is also shown. The four curved elements generally provide a good approximation of the exact answer, and are relatively free of azimuthal dependence. On the other hand, twice as many straight-line elements do not perform as well. The

---

* A vortex ring was also used in Ref. 9 to illustrate straight-line element velocity errors.

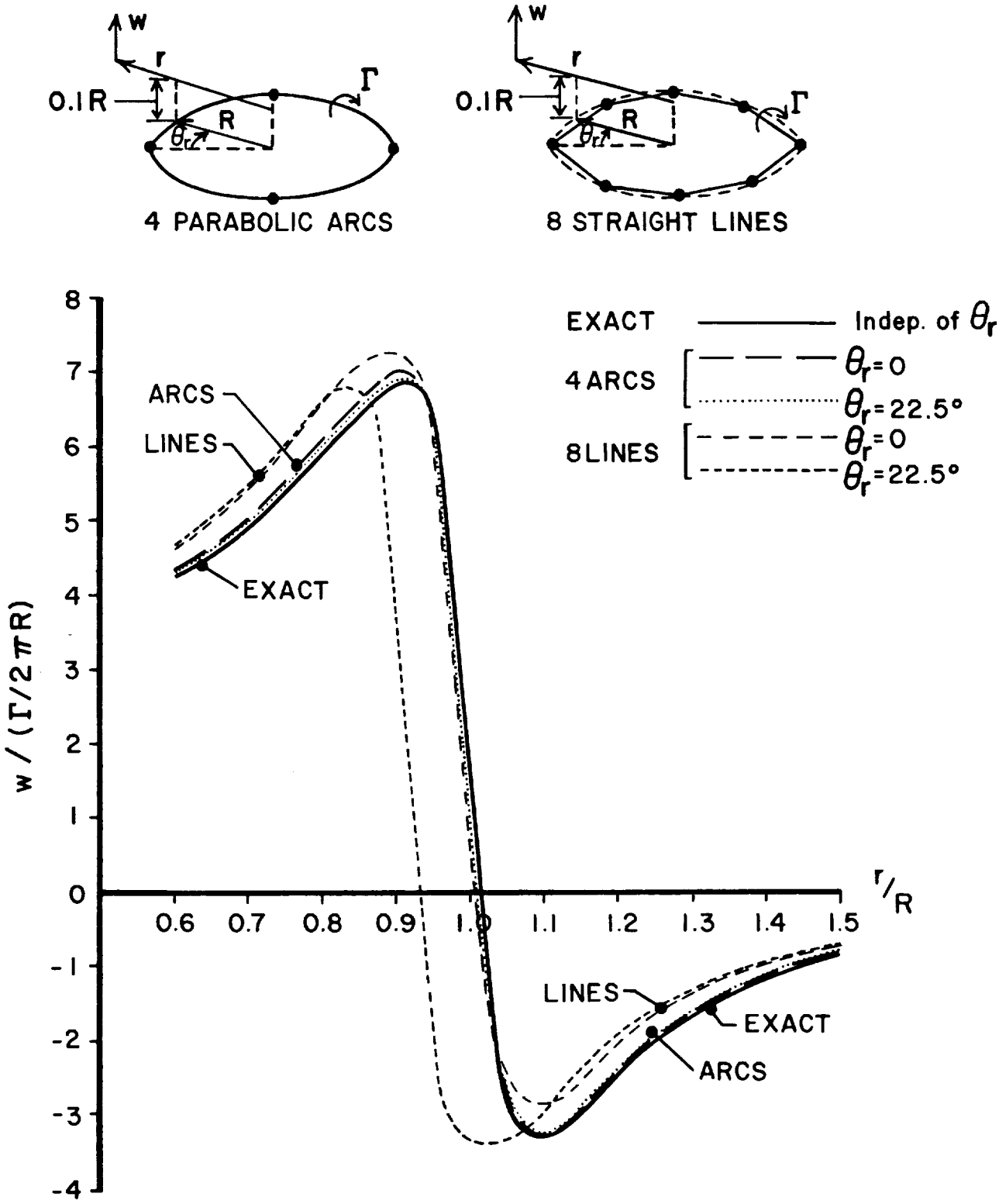

Figure 13. Azimuthal and radial variations in vertical velocity near a vortex ring constructed of four curved elements or eight straight-line elements.

azimuthally dependent position error associated with straight-line elements has a pronounced effect on the velocity field near the ring. For either type of element, increasing the number of elements used, or increasing the distance above the ring, both lead to rapid improvements in accuracy. The effect is particularly dramatic for curved elements. For N elements composing a ring, from Eqs. (30) and (31), the geometric position error is proportional to $(\ell_c/R)^4 \propto \frac{1}{N^4}$ for curved elements and proportional to $(\ell_s/R)^2 \propto \frac{1}{N^2}$ for straight-line elements.

Referring again to Figures 11, 12 and 13, it is clear that the velocity component, w , normal to a curved vortex filament is a sensitive indicator of calculation accuracy. Figure 13 in particular shows that w is subject to rapid variations in the region directly above the filament, and thus to calculate this quantity accurately is a challenge for any vortex element method. Therefore, the ability to correctly predict this quantity is used as a criterion for accuracy in this report. It should be noted that the percentage error in w , although it is a convenient way to present results, is not an indication of comparable percentage error at all points in the flow. At many places the large swirl velocity dominates, making the percentage error much smaller. However, the magnitude of the error in w is an indication of the general magnitude of the velocity error at points equally close to the filament. At points close to the filament, the magnitude of this error is shown in the next subsection to be the same order as that of the self-induction effect. Therefore, in cases where filaments are in close proximity to one another, these errors are too large if such calculations are to be made to a consistent order of accuracy.

3.4 Analysis of Straight-Line Element Errors

The previous subsection presented computed results showing the errors in the velocity near a vortex ring simulated by straight-line vortex elements. It will now be shown that the errors can be predicted by an analytical model that assumes the major error contribution is due to the nearest one or two elements. The local nature of this model demonstrates that similar errors

will be encountered for arbitrary vortex filament configurations, and not just for the vortex ring configuration studied numerically. In other words, it is possible to draw general conclusions about the magnitude and behavior of the errors associated with using straight-line elements.

As a starting point, the percent errors in normal velocity, w, above a vortex ring are summarized in Figure 14. The errors are presented as a function of N, the number of elements and of collocation points, for two distances above the ring. The relative azimuthal locations where the calculations were performed are denoted as end point, midpoint, and quarter point. The end point location is directly above a collocation point; the midpoint location is halfway between collocation points; and the quarter point location is halfway between the end point and midpoint locations. The results presented in Figure 14 correspond to those shown earlier in Figures 11 and 12. When fitting a circular arc, straight-line elements make the maximum error at the midpoint location where the geometric position error is largest. The minimum error for straight-line elements occurs at the end point location. However, for the BCVE the quarter point error is largest, the midpoint error is smallest, and the end point error is in-between. It is obvious from Figure 14 that the BCVE is superior when considered purely from the standpoint of accuracy. It produces large errors only when so few collocation points are used that the element length exceeds the radius of curvature.

An interesting feature of Figure 14 is the strong similarity between the straight-line element results for $z/R = 0.1$ and $z/R = 0.3$. It will be shown that these two calculations can be collapsed into a single curve once the appropriate nondimensional variables are introduced. It is also of interest to know that the straight-line error diminishes as N^{-2} as the number of elements become large, whereas the BCVE convergence rate is much faster, roughly N^{-4}.

To approach this problem analytically consider Figure 15 which shows straight-line elements approximating an arbitrary curved filament with local radius of curvature R. Suppose the point of evaluation is close to the

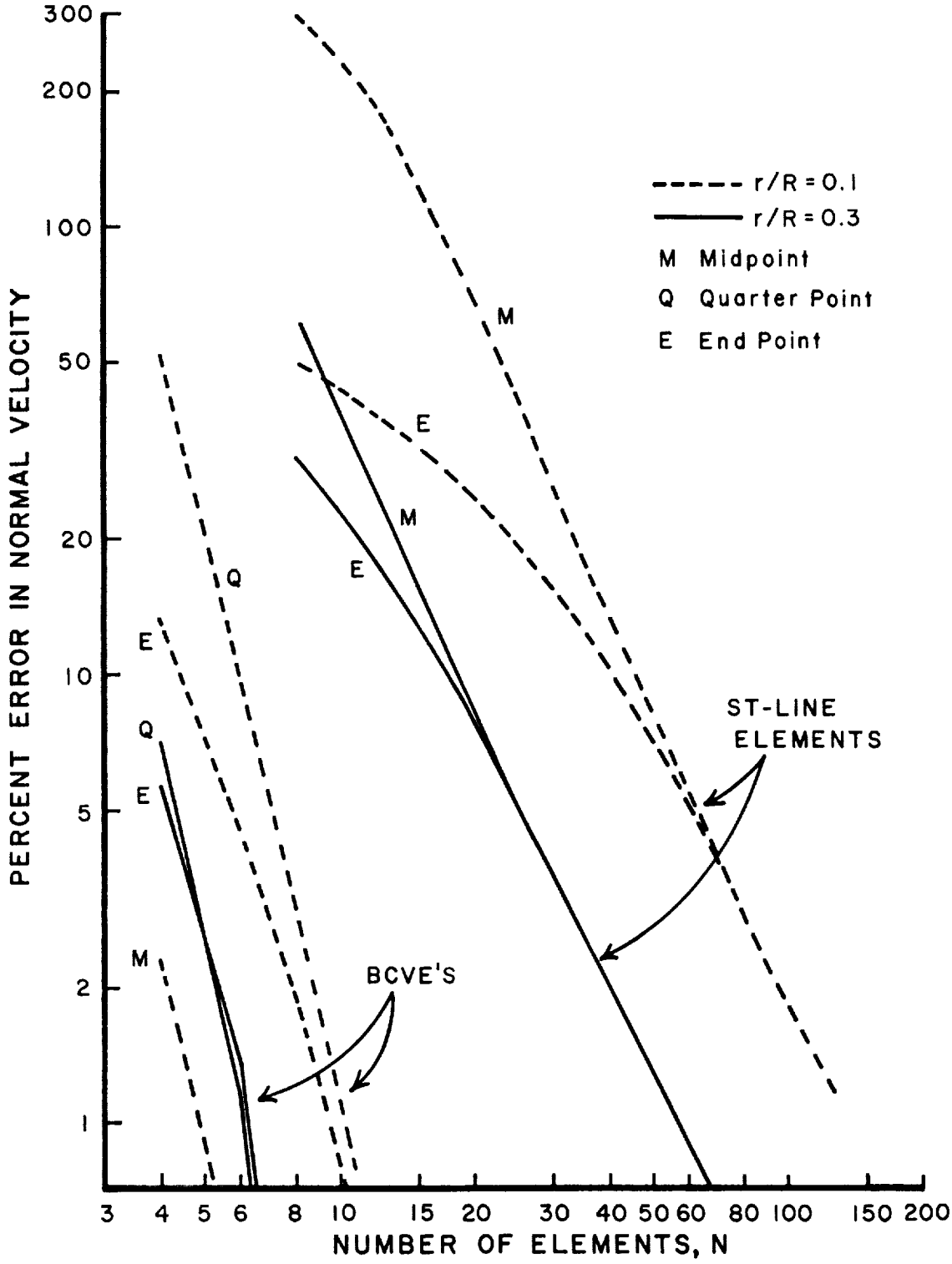

Figure 14. Percent error in normal velocity above the edge of a vortex ring as a function of the number of elements.

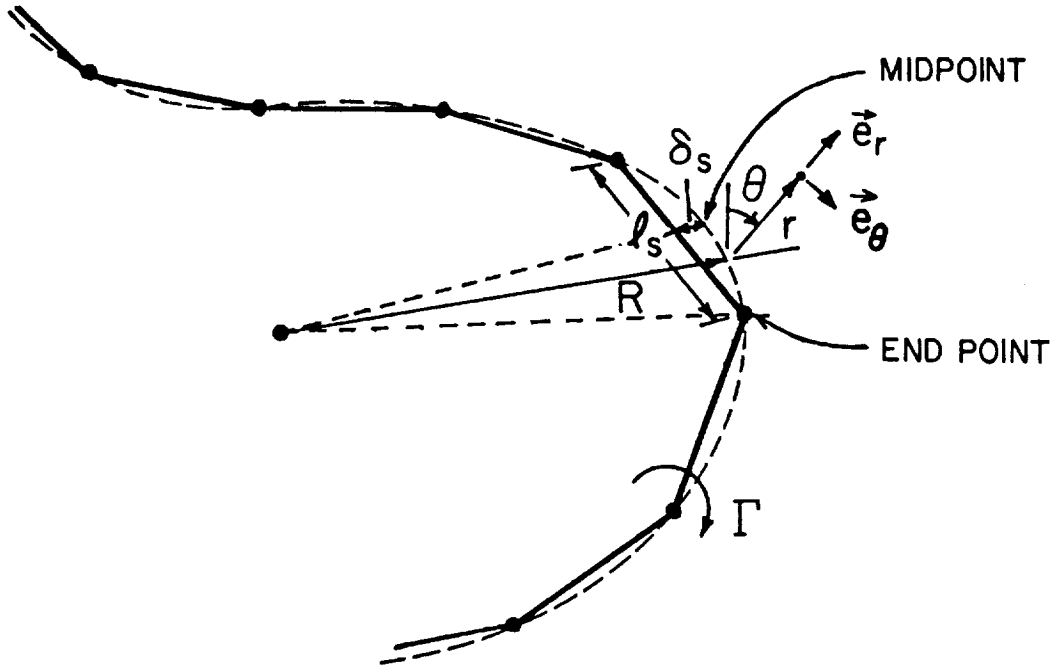

Figure 15. Local coordinate system for the analysis of errors induced by straight-line elements approximating an arbitrary curved vortex filament.

filament in the sense that $r \ll \ell_s$, but still far enough away that $r \gg \delta_s$. Furthermore, it is assumed that there is an adequate number of collocation points along the filament, so that $\ell_s \ll R$. Only the midpoint and end point locations will be considered in detail, since these produce the maximum and minimum error, respectively. In the midpoint case, at distances less that an element length, it is reasonable to suppose that the nearest element produces most of the error. Similarly, the two adjacent elements should be the important contributors in the end point case. These cases are illustrated in Figure 16a,b respectively. The analytical approach is to estimate the error by calculating the difference between the velocity field of these one or two straight-line elements and the corresponding arc of radius R . Accounting for the smaller errors of more distant elements can then be included as a refinement.

The required calculations are relatively straightforward, but somewhat lengthy. Much of the effort is directed at expanding the results in the small parameters r/ℓ_s . However, this work ultimately leads to simple nondimensional results. Therefore, the required steps are only explained briefly, and the principal results are cited and interpreted.

The straight-line element contribution given in Eq. (27) is expressed in a coordinate system centered on the element as shown in Figure 7. The velocity must be evaluated at the appropriate position and re-expressed in the coordinate system of either Figure 16a or 16b, depending on whether the end point or midpoint problem is being considered. As an alternative, the straight-line integration can be performed directly for the appropriate element orientations. Along the way, the results are expanded in the small parameters r/ℓ_s , ℓ_s/R and δ_s/r , and, in a consistant manner, only lowest order terms are retained. This step allows the velocities to be expressed as simple formulas which are subject to physical interpretation. After considerable manipulation, the velocity contributions of the nearest straight-line element(s) in the midpoint and end point cases are, respectively,

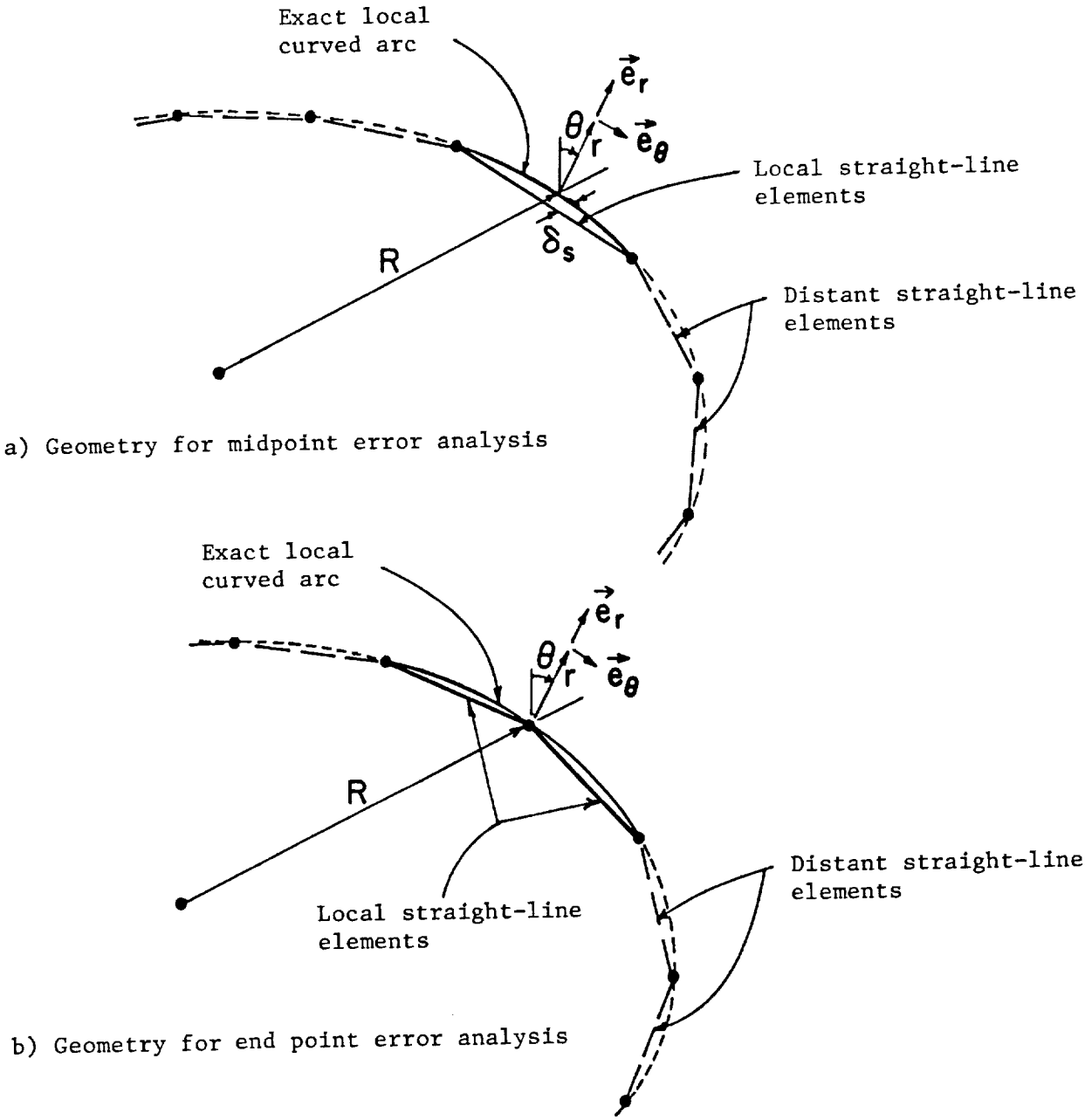

Figure 16. Element geometries for evaluating midpoint and end point errors.

$$\vec{q}_{SL}\Big|_{MP} = \frac{\Gamma}{2\pi r}\left[1 - 2\left(\frac{r}{\ell_s}\right)^2\right]\vec{e}_\theta$$

$$- \frac{\Gamma}{4\pi R}\left\{\left[\frac{1}{4}\left(\frac{\ell_s}{r}\right)^2 - \frac{1}{2}\right]\cos\Theta\,\vec{e}_r + \left[\frac{1}{4}\left(\frac{\ell_s}{r}\right)^2 + \frac{1}{2}\right]\sin\Theta\,\vec{e}_\theta\right\} \tag{34}$$

and

$$\vec{q}_{SL}\Big|_{EP} = \frac{\Gamma}{2\pi r}\left[1 - \frac{1}{2}\left(\frac{r}{\ell_s}\right)^2\right]\vec{e}_\theta - \frac{\Gamma}{4\pi R}\left(\frac{\ell_s}{r}\right)\sin\Theta\,\vec{e}_\theta \tag{35}$$

As expected when near the elements, the dominant term* is $\Gamma/2\pi r$, the swirl velocity of a two-dimensional vortex. The remaining terms correct for the finite length of the elements and their orientation and offset relative to the point of evaluation.

The corresponding results for a curved arc must also be derived. As Figures 16a and b indicate, a Biot-Savart integration over a finite length centered curved arc is required in either case; only the span of the arc is different. In general, such an integration comes out in terms of special functions (elliptic integrals). However, for the small parameter assumptions being invoked, the difference between the circular arc and a parabolic arc is higher order. Therefore it is easiest to start with this simplification, and the integration then proceeds as the BCVE derivation described in Section 2. Since the arc is small in the sense that $\ell_s/R \ll 1$, the higher order term $\epsilon^2 x_1^4$ modelled in the BCVE derivation can be neglected here. The fact that the arc is centered about the point of evaluation is a further simplification. That the BCVE and the circular arc answer coincide in this limit illustrates again that the BCVE is an inherently more accurate element.

---

* The term proportional to r^{-2} in the second line of Eq. (34), which appears to be the most singular, cannot dominate because of the restriction that r/ℓ_s , ℓ_s/R , and δ_s/r all be small.

The velocity contributions from the curved arc(s) between the nearest collocation points in the midpoint and end point cases are, respectively,

$$\vec{q}_{CA}\Big|_{MP} = \frac{\Gamma}{2\pi r}\left[1 - 2\left(\frac{r}{\ell_s}\right)^2\right]\vec{e}_\theta$$

$$+ \frac{\Gamma}{4\pi R}\left\{\left[\ln\left(\frac{\ell_s}{r}\right) - 1 + 3\left(\frac{r}{\ell_s}\right)^2\right]\cos\Theta\ \vec{e}_r\right. \tag{36}$$

$$\left. - \left[\ln\left(\frac{\ell_s}{r}\right) + 3\left(\frac{r}{\ell_s}\right)^2\right]\sin\Theta\ \vec{e}_\theta\right\}$$

and

$$\vec{q}_{CA}\Big|_{EP} = \frac{\Gamma}{2\pi r}\left[1 - \frac{1}{2}\left(\frac{r}{\ell_s}\right)^2\right]\vec{e}_\theta$$

$$+ \frac{\Gamma}{4\pi R}\left\{\left[\ln\left(\frac{\ell_s}{r}\right) - 1 + \frac{3}{4}\left(\frac{r}{\ell_s}\right)^2\right]\cos\Theta\ \vec{e}_r\right. \tag{37}$$

$$\left. - \left[\ln\left(\frac{2\ell_s}{r}\right) + \frac{3}{4}\left(\frac{r}{\ell_s}\right)^2\right]\sin\Theta\ \vec{e}_\theta\right\}$$

As before, the dominant effect is the $\Gamma/2\pi r$ swirl velocity, while the remaining terms account for the finite length, changing position, and curvature of the filament. The logarithmic terms account for the local curvature of the filament and are missing in the corresponding straight-line results.

Viewing Eqs. (36) and (37) as correct, and Eqs. (34) and (35) as the straight-line element approximations, the error associated with the local straight-line elements is obtained by finding the difference between the corresponding expressions. Thus, the error associated with the filament being

locally represented by straight-line elements is given by

$$\Delta\vec{q}_L\Big|_{MP} = \frac{\Gamma}{4\pi R}\left\{\left[\frac{1}{4}\left(\frac{\ell_s}{r}\right)^2 + \ln\left(\frac{\ell_s}{r}\right) - \frac{3}{2} + 3\left(\frac{r}{\ell_s}\right)^2\right]\cos\Theta\,\vec{e}_r + \left[\frac{1}{4}\left(\frac{\ell_s}{r}\right)^2 - \ln\left(\frac{\ell_s}{r}\right) + \frac{1}{2} - 3\left(\frac{r}{\ell_s}\right)^2\right]\sin\Theta\,\vec{e}_\theta\right\} \tag{38}$$

and

$$\Delta\vec{q}_L\Big|_{EP} = \frac{\Gamma}{4\pi R}\left\{\left[\ln\left(\frac{2\ell_s}{r}\right) - 1 + \frac{3}{4}\left(\frac{r}{\ell_s}\right)^2\right]\cos\Theta\,\vec{e}_r + \left[\left(\frac{\ell_s}{r}\right) - \ln\left(\frac{2\ell_s}{r}\right) - \frac{3}{4}\left(\frac{r}{\ell_s}\right)^2\right]\sin\Theta\,\vec{e}_\theta\right\} \tag{39}$$

where the subscript L indicates that the error is from the local element(s) only.

Aside from the appearance of different constants in the expressions, the major difference between Eqs. (38) and (39) is the additional term involving $(\ell_s/r)^2$ in the midpoint error. Rewriting this term using Eq. (39) gives

$$\frac{\Gamma}{4\pi R}\,\frac{1}{4}\left(\frac{\ell_s}{r}\right)^2 = \frac{\Gamma\delta_s}{2\pi r^2} \tag{40}$$

which shows that this term represents a vortex dipole of strength $\Gamma\delta_s$. This dipole arises from the position error, δ_s, of the vortex filament which is a maximum in the midpoint case. The dipole comes from subtracting away the vortex at the correct location and adding the straight-line vortex at an incorrect location in its place. This dipole term is the dominant source of error, and is largely responsible for size of the midpoint error. The other terms in Eqs. (38) and (39) are associated with incorrect orientation and the absence of curvature.

The error from the remainder of the straight-line elements must also be evaluated. It can be shown that only the next few nearby elements induce any significant error. Surprisingly, to lowest order this additional error has the extremely simple form of a constant velocity normal to the filament, independent of r/ℓ_s . Analysis shows that as ℓ_s decreases, the fitting error gets smaller, but the sources of error are nearer. These two effects counterbalance each other to lowest order leaving a constant residual error velocity. This error from distant elements on a constant curvature arc was evaluated numerically, with the results

$$\Delta\vec{q}_D\Big|_{MP} = \frac{\Gamma}{4\pi R}(.270)\left[-\cos\Theta\,\vec{e}_r + \sin\Theta\,\vec{e}_\theta\right] \tag{41}$$

and

$$\Delta\vec{q}_D\Big|_{EP} = \frac{\Gamma}{4\pi R}(.078)\left[-\cos\Theta\,\vec{e}_r + \sin\Theta\,\vec{e}_\theta\right] \tag{42}$$

The midpoint error term is larger because the distant elements are closer.

The total straight-line errors for the midpoint and end point cases can be obtained by adding Eq. (41) to Eq. (38) and Eq. (42) to Eq. (39), giving in either case

$$\Delta\vec{q}_{TOT} = \Delta\vec{q}_L + \Delta\vec{q}_D \tag{43}$$

Therefore, for $r/\ell_s \ll 1$,

$$\Delta\vec{q}_{TOT}\Big|_{MP} = \frac{\Gamma}{4\pi R}\left\{\left[\frac{1}{4}\left(\frac{\ell_s}{r}\right)^2 + \ln\left(\frac{\ell_s}{r}\right) - 1.770 + 3\left(\frac{r}{\ell_s}\right)^2\right]\cos\Theta\,\vec{e}_r\right.$$
$$\left. + \left[\frac{1}{4}\left(\frac{\ell_s}{r}\right)^2 - \ln\left(\frac{\ell_s}{r}\right) + .770 - 3\left(\frac{r}{\ell_s}\right)^2\right]\sin\Theta\,\vec{e}_\theta\right\} \tag{44}$$

and

$$\vec{\Delta q}_{TOT}\Big|_{EP} = \frac{\Gamma}{4\pi R}\left\{\left[\ln\left(\frac{2\ell_s}{r}\right) - 1.078 + \frac{3}{4}\left(\frac{r}{\ell_s}\right)^2\right]\cos\Theta\,\vec{e}_r\right.$$

$$\left. + \left[\left(\frac{\ell_s}{r}\right) - \ln\left(\frac{2\ell_s}{r}\right) + .078 - \frac{3}{4}\left(\frac{r}{\ell_s}\right)^2\right]\sin\Theta\,\vec{e}_\theta\right\} \qquad (45)$$

These equations differ very little from Eqs. (38) and (39), demonstrating that the local element errors are by far the most important. The important feature of this result is that the total error, $\vec{\Delta q}_{TOT}$, once nondimensionalized by $\Gamma/4\pi R$, depends only on the angular position, Θ, and on the nondimensional distance r/ℓ_s. This establishes the order of magnitude of the error, and shows that its dependence on distance scales with the element length.

Figure 17 shows the results of Figure 14 replotted in this nondimensional form. The straight-line errors at different distances from the ring now collapse onto the same curve. The analytical formulas for the midpoint and end point errors, Eqs. (44) and (45), are seen to agree well with the computed results as long as r/ℓ_s is sufficiently small. The apparent failure of these formulas as $r/\ell_s \to 1.0$ is only due to the breakdown in the small parameter expansions used in their derivation, and is not unexpected. The ability to collapse the error curves in this way is a universal result, and is not unique to vortex ring configurations. Normal velocity errors from other filament shapes would fall on the same curves in Figure 17. This is demonstrated by the analytical derivation which makes no specific assumption regarding the overall filament shape. Equations (44) and (45) are generally applicable to predict straight-line element errors for arbitrary filament shapes.

The BCVE errors from Figure 14 are also replotted in Figure 17. The BCVE errors do not collapse onto universal curves because their fitting errors have a somewhat different functional dependence. Essentially, the BCVE fit

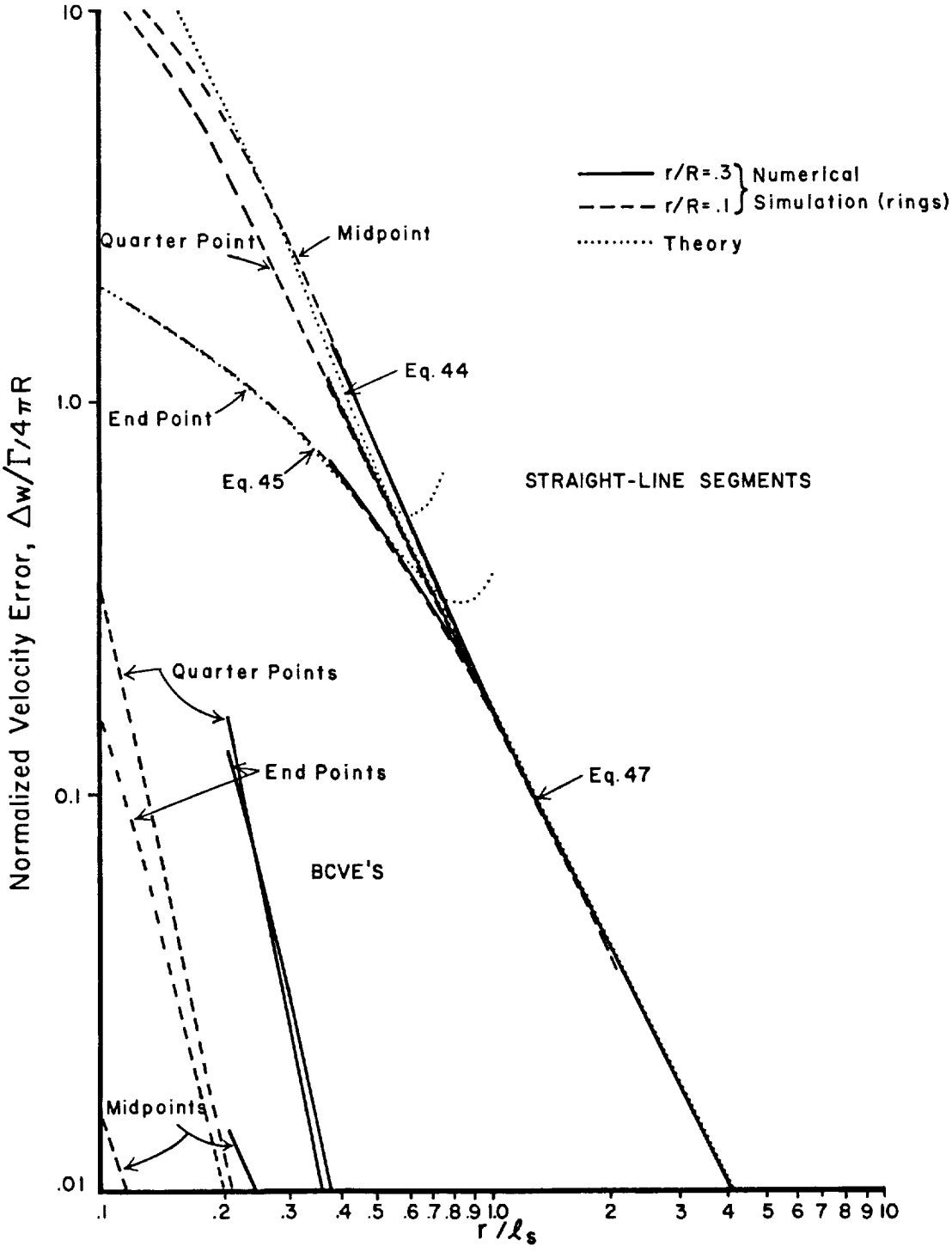

Figure 17. Universal plot of straight-line element errors comparing computed and theoretical results.

improves very rapidly as r/ℓ_s increases, as can be seen by the relatively steep slope of the BCVE curves. The worst BCVE errors are typically about two orders of magnitude smaller than the corresponding straight-line element errors. These trends correspond roughly to the formulas for the geometric displacement errors given earlier in Eqs. (30) and (31).

Figure 17 also shows that the nondimensionalization collapses the results in the region of final convergence as the elements become smaller compared to the distance from the filament. In this case, the point of evaluation is still effectively close to the filament, namely $r \ll R$. However, because the point of evaluation is distant relative to the element length, the distinction of being over an end point or a midpoint is washed out. The case of $r/\ell_s > 1$ was also studied analytically. It can be shown that the residual error is of the vortex dipole type (very much like the predominant term in the midpoint error discussed earlier). The dipole strength can be shown to be $\Gamma\bar{\delta}_s$, where $\bar{\delta}_s$ is the average geometric displacement error along the arc. It can also be shown that $\bar{\delta}_s = 2\delta_s/3$ where δ_s is given in Eq. (30). The final convergence error velocity is then found to be

$$\Delta\vec{q}_F = \frac{\Gamma}{4\pi R}\frac{1}{6}\left(\frac{\ell_s}{r}\right)^2 \left[\cos\Theta\,\vec{e}_r + \sin\Theta\,\vec{e}_\theta\right] \qquad r/\ell_s > 1 \qquad (46)$$

Note the similarity to the dipole terms in Eq. (44). This result is plotted in Figure 17 and shows excellent agreement with the numerical simulation for $r/\ell_s > 1$. For $r/\ell_s < 1$, the formula also predicts the straight-line quarter point error in normal velocity to good accuracy, although this appears to be somewhat fortuitious. Equation (46) exhibits the same nondimensional dependences found earlier in Eqs. (44) and (45).

At this point, the results of this subsection are summarized. General formulas, Eqs. (44), (45) and (46), have been developed to predict the errors associated with the use of straight-line elements. These formulas show how the errors for different cases can be nondimensionalized and collapsed onto a single curve. The agreement with computed results is excellent. The errors

are induced primarily by the nearest elements and are thus local in character. Fundamentally, straight-line elements induce errors on the order of $\Gamma/4\pi R$, where R is the local radius of curvature, whenever the point of evaluation is within an element length of the vortex filament. The corresponding errors induced by the BCVE method are typically two orders of magnitude smaller.

The size of the straight-line element error raises a disturbing question about the consistency of free wake calculations using straight-line elements. It is generally agreed that the self-induction effect should be included, and this effect is of order $\Gamma/4\pi R$, as the discussion of the SIVE in Section 2 shows. However, the above analysis has demonstrated that straight-line element errors are of this same order whenever the point of evaluation falls within one element length of the filament. Note that the general nature of the analysis demonstrates that this will be true for realistic wake configurations as well as for idealized filament configurations such as rings or helices. It is frequently necessary to calculate velocities within one element length of vortex filament in free wake calculations, both in hover and forward flight. For instance see the forward flight calculations presented later in Section 4. It is not formally correct to retain some effects of order $\Gamma/4\pi R$ while discarding others. Furthermore, the local radius of curvature, R, is often much smaller than the rotor radius, considerably amplifying effects of order $\Gamma/4\pi R$ in high distortion portions of the wake.

3.5 Calculation Time

This subsection describes the factors that influence the computer time required to determine the velocity field around vortex filaments.* The

* It should be emphasized that these calculations deal only with the wake and are not rotor performance calculations. In practice, wake calculations of this type are only one part of the larger calculation to determine blade loading, blade dynamic motion and vehicle trim.

relative times to perform calculations using either straight-line elements or curved vortex elements are compared. The dependence of time on the type of element and the number of elements is evaluated for both prescribed wake and free wake type calculations. The important issue of calculation accuracy was treated in the previous subsection and the relationship between time and accuracy is studied in the next subsection. In addition to explaining the factors influencing calculation time, the discussion below outlines the operations required to implement the curved vortex element method.

The straight-line element calculation procedure was taken from Appendix I of Ref.3 (essentially the same approach is also derived in Ref. 8). This method is straightforward and efficient. Given two points in a Cartesian coordinate system, the three velocity components due to a straight-line vortex element connecting these points are found directly in the same coordinate system. The time to do one such calculation is denoted by T_{SL} .

The Basic Curved Vortex Element (BCVE) calculation procedure was taken from Section 2 of this report. There are several factors which affect computation time. In the first place, there are actually two element calculation times. As mentioned in Section 2, for high accuracy near the vortex filament, it is necessary to evaluate the element integrals in three sub-intervals. The time to do this evaluation is denoted by $T_{CE(S)}$. However, at distances greater than roughly three-quarters the distance between the element end points, the sub-interval integration is not required for accurate results (the error associated with this simplification is less than 1%). The time to do a BCVE calculation without the sub-intervals is denoted by T_{CE} . In practice, the majority of BCVE calculations are of this type. This simplification is important since $T_{CE} \simeq 1/2\ T_{CE(S)}$. The BCVE element model, as currently formulated, gives the velocity components in a local element-fixed coordinate system, so the velocity components in a global coordinate system must be obtained by a subsequent transformation. This transformation is included in the times T_{CE} and $T_{CE(S)}$.

Additional operations are required to use the curved element model. The curved element must be sized, located and oriented in space. Of the possible

approaches to do this, a scheme called the interpolated point method was chosen. It is convenient to divide these operations into three separate computer times. The first time, T_A , is associated with passing circular arcs through each set of three adjacent points and finding the radius of curvature, the arc angles, and the vectors (tangent, normal and binormal) at the central point which effectively locate the arc in space. The second time, T_{IP} , is associated with the interpolated point method. An interpolated point is located between each two collocation points by averaging the midpoint locations of the two circular arcs passed between these points. The third time, T_G , is associated with finding the geometry and local coordinate system for the BCVE passing through each two collocation points and their interpolated point. The transformation matrix required to go from local to global coordinates is determined in this process.

Whether BCVE's or straight-line elements are used for most of the vortex filament, the velocity at a point on the element, induced by the element itself, is properly found using a Self-Induction Vortex Element (SIVE) of the type described in Section 2. This element uses a circular arc filament passed through three adjacent collocation points. The self-induced velocity is found at the middle collocation point and is normal to the plane of the arc. The time required to do a calculation of this type is conveniently divided into two parts. The first contribution is the time, T_A , associated with finding the properties of the arc passed through three points, including the tangent, normal and binormal vectors which form the local element coordinate system at the central point. Exactly the same set of operations are required as part of the procedure to establish the BCVE geometry. Thus, the time T_A required to find the geometry for a self-induction calculation need only be done if straight-line elements are used. If BCVE's are used for the rest of the vortex, the required information is already available, and need not be recalculated. A second time contribution, T_{SI} , is the time required to make the SIVE calculation once the arc properties are known, and to resolve the self-induced velocity into global coordinates. This portion of the self-induction calculation time is always required.

Table 1 summarizes the definitions of the time coefficients, and gives the relative values of the ones which ultimately have a significant impact on computer time.

Now that the times to do individual operations have been defined, it is possible to develop formulas to make rough estimates of the computation time for prescribed wake and free wake calculations. It should be stressed that there is a danger associated with this estimation approach. Efficient computing involves the development of a dynamic structure in which the various portions of a program function in concert. The run time is sensitive to the way in which the various constituent parts are made to interact. The approach of assigning times to the various individual activities serves to compartmentalize this process in a way that is conceptually helpful, but is only an approximation to what may be actually happening in the program. Thus, the formulas to be given for estimated run times should be viewed as approximate. Nevertheless, they do show clearly the predominant functional dependences and relative importance of various parts of the calculation to the overall time.

Estimated values for some of the time contributions are also given in Table 1. The values were obtained from numerical simulations performed on an IBM 3081 computer. The programs were written in FORTRAN and used the FORTRAN H optimizing compiler. Of course, the actual values obtained depend on the system used and on the actual program structure. There was an effort to make the various parts run efficiently, but the curved element methodology is complex and further significant optimization of its various parts is believed to be possible. The subsequent discussion will show that some of the time contributions in Table 1 are much more important than others in determining the overall calculation time and, in particular, the time contributions associated with a given method are not simply additive. Additional results from these numerical simulations are presented in Subsection 3.6.

TABLE 1

Definition of Normalized Computer Time Coefficients for Vortex Element Calculations*

$T_{SL} = 1.0$	Straight-line element (Ref. 3)
$T_{CE} \simeq 3.3$	BCVE (no subintervals)
$T_{CE(S)} \simeq 6.7$	BCVE (with subintervals)
T_{SI}	SIVE
T_A	Three point circular arc geometry and orientation
T_{IP}	Interpolated point location
T_G	BCVE geometry and local coordinates
T_P	Prescribed wake point generation
T_{OC}	Other contributions to velocity (blade circulation, near wake, far wake, etc.)
T_{UD}	Update free wake collocation points

* These time coefficients do not indicate the relative free wake calculation times for curved and straight-line elements. The ratio of times depends on the number of elements used in each case, e.g., see Eq. (57).

3.5.1 Prescribed Wake Calculations

In a prescribed wake calculation, the wake position is usually determined according to some relatively simple criterion. For instance, the wake location can be kinematically determined using the rotor motion and the downwash field derived from momentum theory, or the wake location may be determined based on a curve fit to experimental data. The Biot-Savart law can then be used to find the velocity induced by the wake at other points of interest, e.g., the downwash induced along the rotor blades. The influence of the wake on itself is not considered in a prescribed wake approach. Thus, such calculations tend to be shorter and simpler than free wake calculations.

If N_S straight-line elements are used to analyze a prescribed wake, then the total calculation time to find the velocity at one point not on the vortex filament is approximately:

$$t_{SL} = N_S(T_{SL} + T_P) \tag{47}$$

Here T_P is the time to generate the points to locate the elements from a given wake prescription. If BCVE's are used instead, the time to find the velocity at one point using N_C elements is given by:

$$t_{CE} = (N_C - P)T_{CE} + PT_{CE(S)} + N_C T_G + N_C T_P \tag{48}$$

Here P is the number of curved elements sufficiently close to the point of evaluation that subinterval integration is required for good accuracy. Typically, only a few elements require the subinterval scheme, so that $P << N_C$.

In formulating Eq. (48) only the time T_G is needed to establish the element geometry. As long as the prescribed wake shape is known analytically,

as will usually be the case, a set of points intermediate to the collocation points can be specified as part of the time contribution T_P . These intermediate points and the collocation points are all that are needed to perform the operations associated with time T_G to locate the BCVE's. In contrast, if only the collocation points were known, then the intermediate points would have to be constructed by the interpolated point method, and the time required would be $T_A + T_{IP} + T_G$. This full procedure is required for free wake calculations, to be discussed later, where the analytical shape is not known, and only a set of collocation points is given.

Equations (47) and (48) can be used to estimate the relative prescribed wake calculation times. For large numbers of elements ($N_C >> P$) the ratio of times is approximately

$$\left.\frac{t_{CE}}{t_{SL}}\right|_{\substack{\text{prescribed}\\\text{wake}}} \approx \frac{T_{CE} + T_G + T_p}{T_{SL} + T_p} \frac{N_C}{N_S} = K_p \frac{N_C}{N_S} \qquad (49)$$

Notice that the time ratio depends linearly on the ratio of the number of elements. The proportionality constant, K_p , for the vortex ring accuracy calculations presented previously is approximately 3.8. This result shows that in prescribed wake calculations significantly fewer curved elements must be used to make the run time comparable to that for straight-line segments. The use of much larger curved elements is not at all unreasonable, since three or four straight-lines are required to make a crude geometric approximation of an arc. Although the result of Eq. (49) may appear to show the curved element approach at a disadvantage for prescribed wakes, the numerical simulations presented later illustrate that the curved element method is actually superior in this application when the issue of accuracy is considered. Accuracy is probably the important consideration in any event, since the run time is less of a problem in prescribed wake calculations than it is in free wake analyses.

3.5.2 Free Wake Calculations

Free wake calculations attempt to determine the actual shape of the wake as a free vortex flow. The primary emphasis is on locating the strong, concentrated tip vortex. In the usual approach to this problem, the velocity is found at a number of collocation points along the wake (connection points for the vortex elements), as well as at other points of interest, such as in the plane of the rotor. The time-dependent evolution of the wake is then followed by a time stepping procedure in which the wake is transported by the net velocity induced at each collocation point. The fact that the influence of the wake on itself must be computed has a fundamental effect on the way the calculation time depends on the number of vortex elements that model the wake.

Only the computer time associated directly with the free wake itself will be considered in the following discussion. The time associated with the other functions a particular computer program may perform, such as blade dynamic motion, vehicle trim conditions, etc., are not discussed and may be considered as a separate issue. Although there are several schemes for making free wake calculations, it is sufficient to make time estimates for the commonly used time stepping Lagrangian approach, which is also the approach taken in Section 4 of this report. Formulas will now be developed for the computer time to calculate the velocity at each point due to all other portions of the wake. Note, however, that in many free wake calculation schemes this full updating of the velocity field is not done at every time step in order to reduce the computer time. The effect of this sort of optimization on the calculation time formulas is discussed later.

For the present purpose it is sufficient to consider a rotor with B blades, each trailing a wake represented by N elements located between $N + 1$ collocation points. At each time step the last point and last element in the wake are discarded, while a new point and new element are added at the top of the wake to fill the space left by the incremental blade motion. Because the last point is discarded, it is necessary to find the velocity only at the first N collocation points. Typically, it will also be necessary to find the velocity induced by the wake at M other points along each rotor blade.

If the full free wake calculation is done using N_S straight-line elements and SIVE's, then the time estimate for one calculation cycle (one time step) is given by:

$$t_{SL} = B^2 N_S(N_S - 2)T_S + BN_S(T_A + T_{SI}) + B^2 N_S M T_S + BN_S T_{OC} + BN_S T_{UD} \quad (50)$$

The first term on the right reflects the fact that $N_S - 2$ straight-line segments are needed to find the velocity induced at each of the N_S collocation points. The number is $N_S - 2$, not N_S, because each self-induction calculation using SIVE's spans two intervals between points. The second term on the right accounts for these self-induction calculations. The third term on the right is associated with the N_S elements required to find the velocity at each of the M other points not on the wake. The fourth term is associated with the calculation of the velocity induced on the collocation points by all other contributions, such as the bound circulation on the blades, near wake and far wake model, etc. The final term on the right is the computer time required to time step and update the collocation point positions.

A corresponding estimate can be made for a free wake calculation involving BCVE's. If the number of curved elements is N_C, the time estimate is:

$$t_{CE} = B^2 N_C(N_C - 2)T_{CE} + B^2 N_C P(T_{CE(S)} - T_{CE}) + BN_C(T_A + T_{IP} + T_G + T_{SI}) + B^2 N_C(M - Q)T_{CE} + B^2 N_C Q T_{CE(S)} + BN_C T_{OC} + BN_C T_{UD} \quad (51)$$

where P and Q are the average number of subinterval element calculations required for points on the wake and elsewhere, respectively. The first two terms on the right hand side of Eq. (51) account for the time to do BCVE calculations for the velocity at the N_C collocation points in the wake. The third term accounts for the time to size and locate the elements, and for the time to do the self-induction calculations. Both of these operations require

the time T_A to find the three point circular arc geometry and orientation, so it is only necessary to do this sequence of operations once (hence the time appears as T_A, not $2T_A$). The fourth and fifth terms on the right are the times required to find the velocity at M other points not on the wake. The sixth term is the time to calculate the effect of all other velocity contributions (bound circulation, far wake, etc.) on the free wake. The seventh term is the computer time required to time step and update the collocation point positions.

The relative size of these computer time estimates using either straight-line or curved vortex elements can now be assessed. The numbers P and Q will be relatively small since on the average only a few other collocation points will be near enough to any given element to require subinterval integration. Typically $N >> M >> 1$, namely most of the calculations involve points in the wake itself, even though a substantial number of calculations may also be made elsewhere (although not necessarily at every time step). Equations (50) and (51) show that element geometry and self-induction calculation times depend linearly on N, and are thus relatively unimportant to the total time required. The largest terms contain the factors B^2N^2 and B^2NM, with the B^2N^2 term usually being much larger. Then using Eqs. (50) and (51) and Table 1, the ratio of calculation times for the two methods using full velocity updating is approximately, for $N >> M >> 1$,

$$\left.\frac{t_{CE}}{t_{SL}}\right|_{\substack{\text{one time step}\\ \text{full updating}}} \approx \frac{T_{CE}}{T_{SL}}\,\frac{N_C^2 + N_C M}{N_S^2 + N_S M} \approx \frac{T_{CE}}{T_{SL}}\left(\frac{N_C}{N_S}\right)^2 \approx 3.3\left(\frac{N_C}{N_S}\right)^2 \qquad (52)$$

This result shows that the ratio of calculation times for one cycle is dominated by the ratio of basic element calculation times and the square of the ratio of the number of elements. Because of the squared effect, it is only necessary to have half as many curved elements, namely curved elements twice as large as straight-line elements, to have the curved element computer time for one free wake calculation cycle be somewhat shorter. Because curved elements have far better accuracy, even when twice as large, the actual

numerical simulations presented later clearly demonstrate their superiority. In fact, when the time to converge an entire free wake calculation is considered, the case for curved elements is even stronger, as will be explained shortly.

For this case of full velocity updating notice that the times associated with establishing the element geometry, $T_A + T_{IP} + T_G$, and the time to do element calculations with subintervals, $T_{CE(S)}$, do not appear in Eq. (52), because both are relatively unimportant. The geometry calculations need to be done only once per free wake calculation cycle, as reflected by their linear dependence on N_C. Thus, they are relatively unimportant compared to the approximately N_C^2 element calculations that must be done. Element calculations using subintervals are time consuming but relatively few need to be done, since P and Q will typically be very much smaller than N_C and M. Interestingly, the geometry routines and the subinterval element model contribute significantly to the excellent accuracy of the curved element methodology, even though they do not have much effect on the calculation time. Therefore, the use of these relatively sophisticated procedures seems well justified.

In practice, free wake computer programs do not necessarily calculate the effect of every element on every other element at each time step. To reduce computer time, various optimization schemes are utilized (Refs. 2, 6 and 7). One approach is to use a partial updating method, first decribed in Ref. 2, in which contributions from parts of the wake distant from a given collocation point are recalculated infrequently, rather than at every time step. It is interesting to consider the effect of optimizing the calculation procedure in this way. The wake must be subdivided into near field and far field (seldom updated) regions in relation to each collocation point. The size of each near field region must be based on a proximity criterion determined by physical considerations. If larger elements are used, then proportionately fewer of these elements will fall within the near field region. As a result, the calculation time formulas (Eqs. (50) and (51)) will still contain terms proportional to N^2, but these terms will be reduced in size by the fraction of elements which are being updated. However, other parts of the calculation

which are proportional to N will now be more important (e.g., element geometry, self-induction, collocation point convection, etc.). The resulting calculation time formulas will contain significant contributions from both N and N^2 terms, although the fraction of elements in the near field must be very small for the N^2 terms not to dominate the wake calculation.

It is difficult to generalize the effect of partial updating on the ratio of curved element to straight-line element calculation times. Probably the most important point is that the calculation time is dramatically reduced, roughly by the fraction of updated elements, regardless of which type of elements are used. Consideration of various cases using the calculation time formulas with numerically determined time coefficients suggests that the most extreme effect of partial updating would be to reduce the power of two in Eq. (52) to unity. The coefficient 3.3 in this equation now applies as a conservative estimate. Then, for rough estimation purposes, Eq. (52) can be generalized as

$$\left.\frac{t_{CE}}{t_{SL}}\right|_{\text{one time step}} \approx 3.3\left(\frac{N_C}{N_S}\right)^{\sigma} \tag{53}$$

where $\sigma = 2$ for full updating and $\sigma \to 1$ for partial updating involving very few elements.

Finally, consider the time required to converge an entire free wake calculation. From a physical point of view, convergence is obtained when the incorrect starting solution is washed out of the free wake region and the solution has relaxed to its final form. This requires the number of blade motion increments to exceed the number of free wake elements, N, trailed from a blade. In practice, adequate convergence of velocity at the blades may require fewer time steps than are needed for full convergence of the entire free wake. In any event, the required number of free wake calculation cycles to obtain convergence, N_{FWC}, will be given by

$$N_{FWC} = K_c N \tag{54}$$

where K_c is an order one constant that depends on the convergence criterion. The time to converge a free wake calculation using straight-line elements is therefore

$$\tau_{SL} = K_c N_S t_{SL} \tag{55}$$

where t_{SL} is the straight-line element computer time for each time step. Likewise, the convergence time for curved elements is

$$\tau_{CE} = K_c N_S t_{CE} \tag{56}$$

where t_{CE} the curved element computer time for each time step.

Using Eqs. (53) (55) and (56), and referring to the preceding discussion of optimization by partial updating, the ratio of free wake convergence times using curved versus straight-line elements is given by

$$\left.\frac{\tau_{CE}}{\tau_{SL}}\right|_{\substack{\text{free wake}\\ \text{convergence}}} = \frac{N_C}{N_S}\frac{t_{CE}}{t_{SL}} \approx 3.3\left(\frac{N_C}{N_s}\right)^{\sigma+1} \tag{57}$$

where $1 < \sigma < 2$ depending on the degree of optimization through partial updating. Because this convergence time ratio depends on the ratio of the number of elements raised to a power, there is an incentive to use larger elements. Using curved elements that are twice as large as straight-line elements will reduce the calculation time for the free wake part of a computer

program, with unquestionably better accuracy. If even larger elements can be used, there will be an even more significant reduction. The trade-off between time and accuracy is considered in the next subsection.

3.6 Time Versus Accuracy Comparisons

It has been shown that using sufficiently large curved elements can reduce computer time, and also that larger curved elements are typically more accurate than smaller straight-line elements. These results can now be combined to see what level of accuracy is offered by each method for a fixed amount of time, and alternatively what amount of time is required for a fixed level of accuracy. The trade-off between computer time and accuracy is now considered by means of numerical simulation.

Figure 18 shows a comparison of calculation time versus number of elements for the vortex ring calculations described in subsection 3.3. The calculation time is that required to find the velocity at a single point above the ring. For the same number of elements the BCVE calculation takes over three times longer. There is more than one BCVE curve because different numbers of subinternal calculations are required depending on how many ring elements are very close to the point of calculation, this being a function of distance and azimuthal location.

Figure 18 can be cross-plotted with Figure 14 to eliminate the number of elements, N. The results presented in Figure 19 show the maximum errors in normal velocity above the vortex ring versus computer time. The high accuracy of the curved element method is clearly apparent. The time versus accuracy relationships in Figure 19 are like those of a prescribed wake calculation, or one time step of an optimized free wake calculation, since the calculation time depends linearly on the number of elements.

To simulate a free wake calculation cycle, calculations were made on three turns of a helix, as shown in Figure 20. This configuration can be thought of as a crude model of a rotor wake in hover. The computer time shown on the top

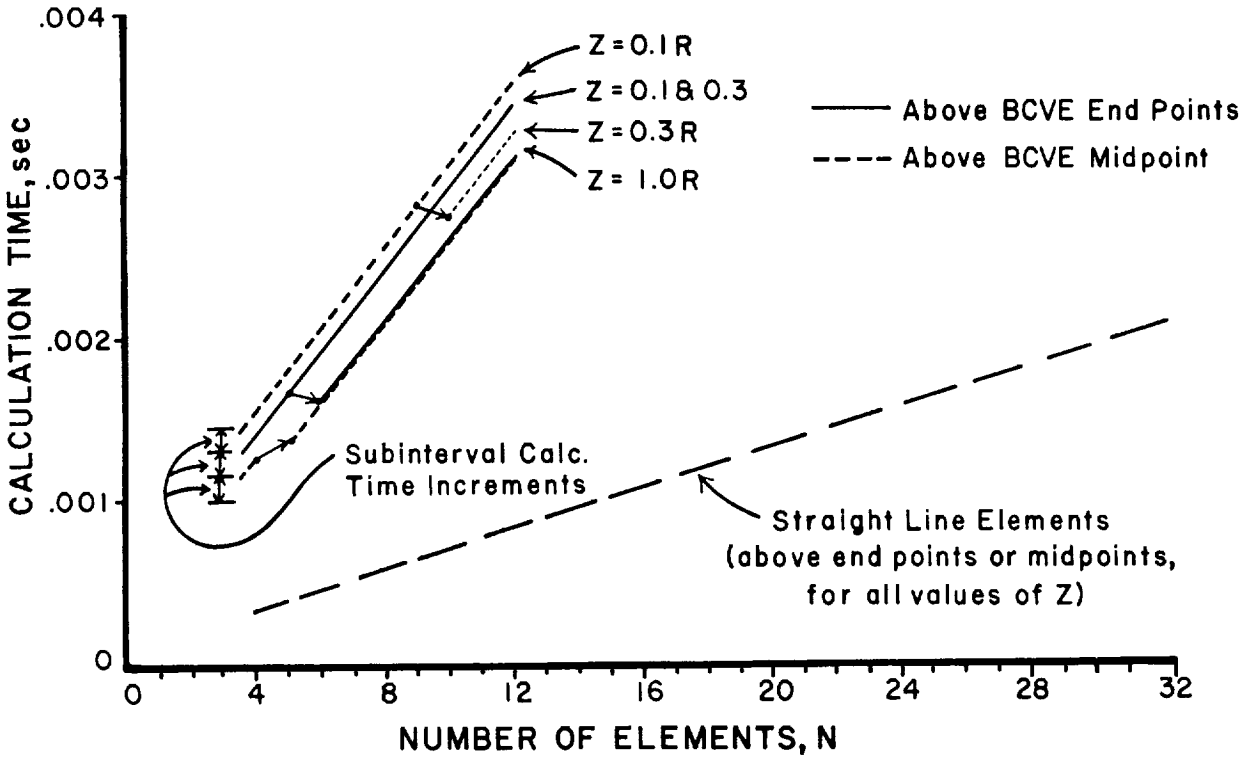

Figure 18. Comparison of curved and straight-line element calculation times for the velocity above a vortex ring as a function of the number of elements.

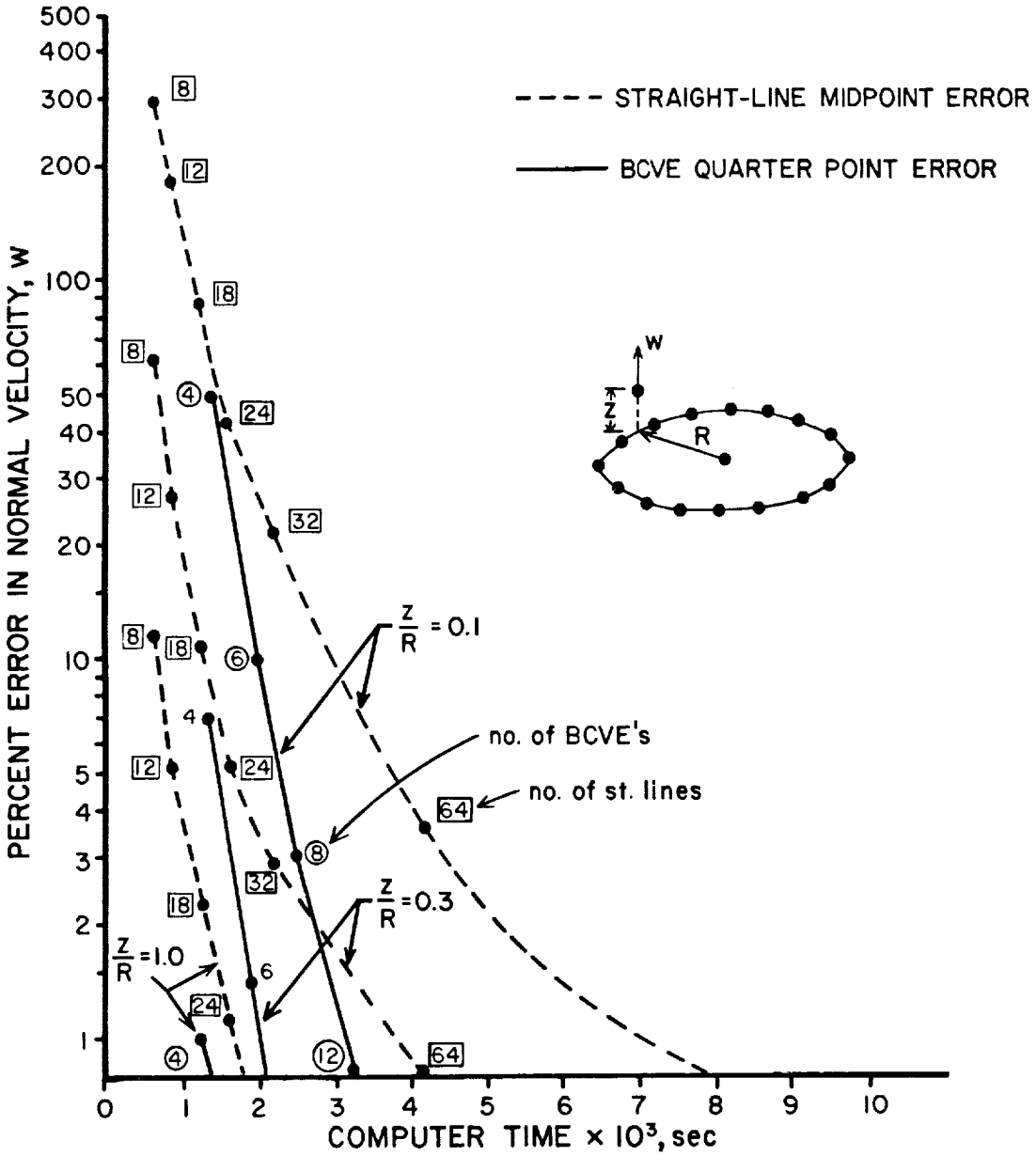

Figure 19. Comparison of peak errors versus computer time for the normal velocity above a vortex ring.

horizontal scale was based on finding the velocity at every collocation point on the helix plus at ten other stations along a blade positioned at the top of the helix. This calculation corresponds to full velocity updating in a free wake time step. The calculated error is that incurred at two representative points. Point A is at the location of an opposing blade, half the helix pitch above the top turn. Point B is in the middle of the filament, on the helix itself. The straight-line and curved element end point errors are compared. This places the straight-line elements in the most favorable light possible since they are most accurate at end points. Because Figure 20 represents a free wake calculation cycle, the computer time is roughly proportional to the square of the number of elements, and thus the use of fewer elements dramatically reduces this time. The curved element method shows dramatic superiority in this comparison, both in terms of accuracy and rate of convergence. The errors at point B are lower than at point A because both methods use the same SIVE to evaluate the self-induction at B. If the same calculation were made to simulate partial velocity updating, the results would be somewhat less dramatic, but the superiority of curved elements would still be clearly evident.

Figure 21 shows a similar calculation only at point B to indicate the effect of azimuthal location of the collocation points. As the number of elements per turn is varied continuously, point B is alternatively subjected to errors ranging between end point and midpoint types. The cross-hatched region in Figure 20 indicates the range of variation of these errors. The errors are induced primarily by the elements above and below since point B itself uses a SIVE in both cases. For the same reasons as before, curved vortex elements are seen to perform dramatically better than straight-line elements. Increasing the helix pitch would significantly reduce the errors. However, the tight helix pitch shown is realistic for a hovering rotor or for simulating the close interaction between filaments in forward flight.

It should again be mentioned that the errors shown are for one particular velocity component. The above results should not be interpreted to mean that all velocity calculations associated with this configuration are similarly in error if straight-line elements are used. There are locations where there

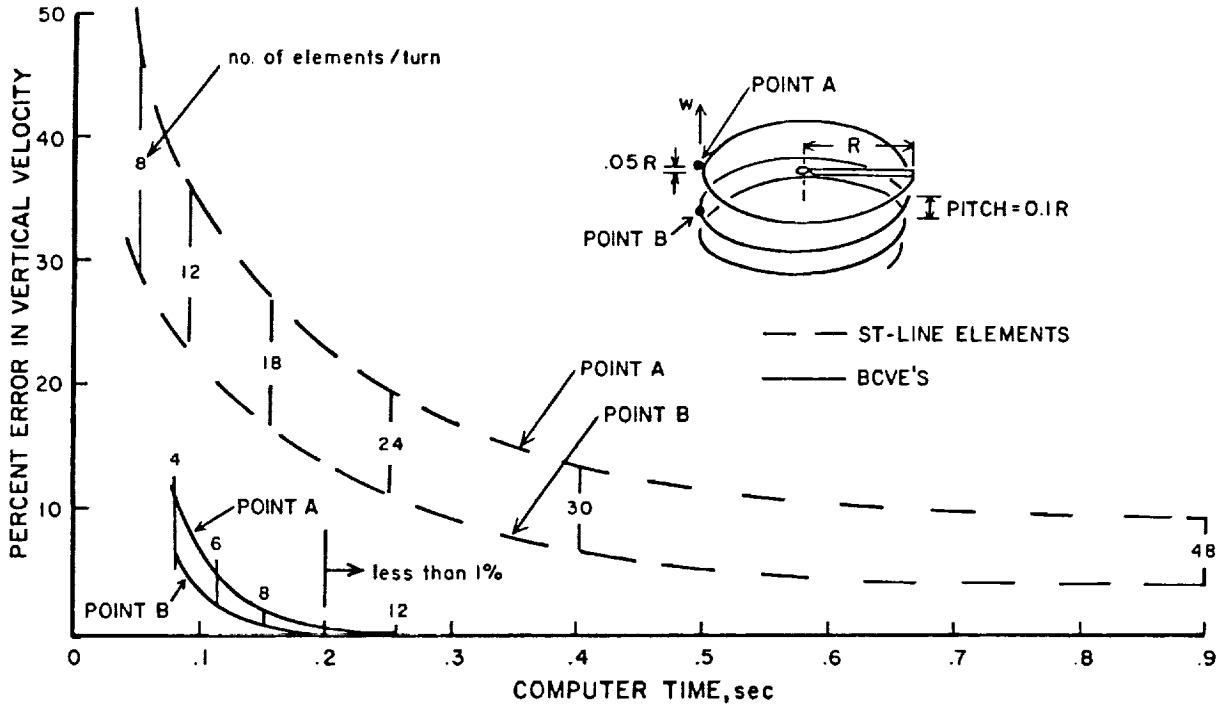

Figure 20. Comparison of straight-line and curved element errors versus computer time for a simulated free wake calculation cycle. Errors are for two points of evaluation on a three turn helix. (Only end point errors are shown.)

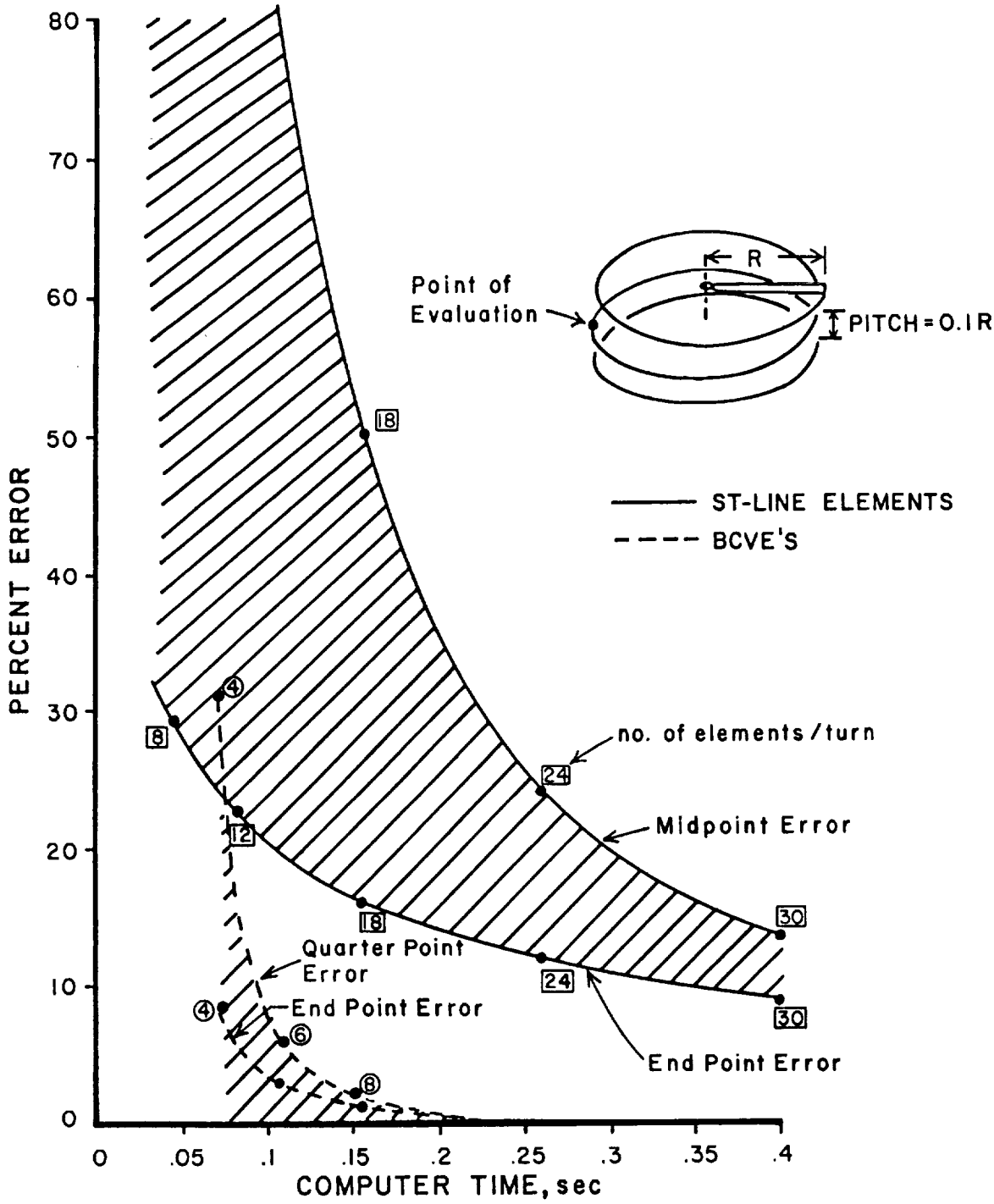

Figure 21. Comparison of straight-line and curved element errors for a simulated free wake calculation cycle, showing the range of errors as the number of collocation points is varied.

would be less difference in accuracy between element types (for instance at the inboard stations on the blade), but the curved element approach would still be more efficient. Nevertheless, the errors shown are of practical concern in free wake calculations, since the answer depends on a delicate balance between closely interacting vortex filaments. Furthermore, these errors were shown to be of the same order as the self-induction effect and must therefore be considered important. By using curved vortex elements, this accuracy problem can be avoided while still improving efficiency.

4. FREE WAKE ANALYSIS

4.1 Forward Flight Free Wake

The curved element method described earlier was implemented into a forward flight free wake analysis. This analysis was developed for two reasons. The first was to demonstrate the use of the curved element approach and to study its behavior. The second reason was to provide the basis for a free wake subroutine to be implemented in the Boeing B-65 rotor airloads computer program, which previously had a prescribed wake. The implementation of the free wake analysis in the Boeing program is described in Section 5 of this report.

For the purpose of demonstration, the forward flight model was kept relatively simple, with the emphasis on determining the tip vortex motion from a single or multi-bladed rotor. The demonstration program has no near wake or inboard wake models to account for the shedding of other vortices. The circulation can be allowed to vary as a function of blade azimuthal location, and the rotor blade can also undergo specified flapping motions. Nevertheless, there is no consideration of rotor trim or of blade dynamic motions in the calculations presented later in this section. However, these omissions in the demonstration program are corrected by its implementation into the Boeing B-65 program as described later. The purpose of the demonstration program is to examine the behavior of curved elements in a tip vortex free wake that is sufficiently simple that other competing effects are not present. Essentially, this model contains only the bound circulation on the blades, several turns of free wake tip vortex, and a special far wake model which is the subject of the next subsection.

The wake induced velocity is determined by calculating the effect of each BCVE at all the free wake collocation points plus all other points of interest (e.g., on the blade). The locations of all these points are first transformed from reference coordinates to the local coordinate system of this BCVE, as shown in Figure 22. All the velocity calculations associated with the

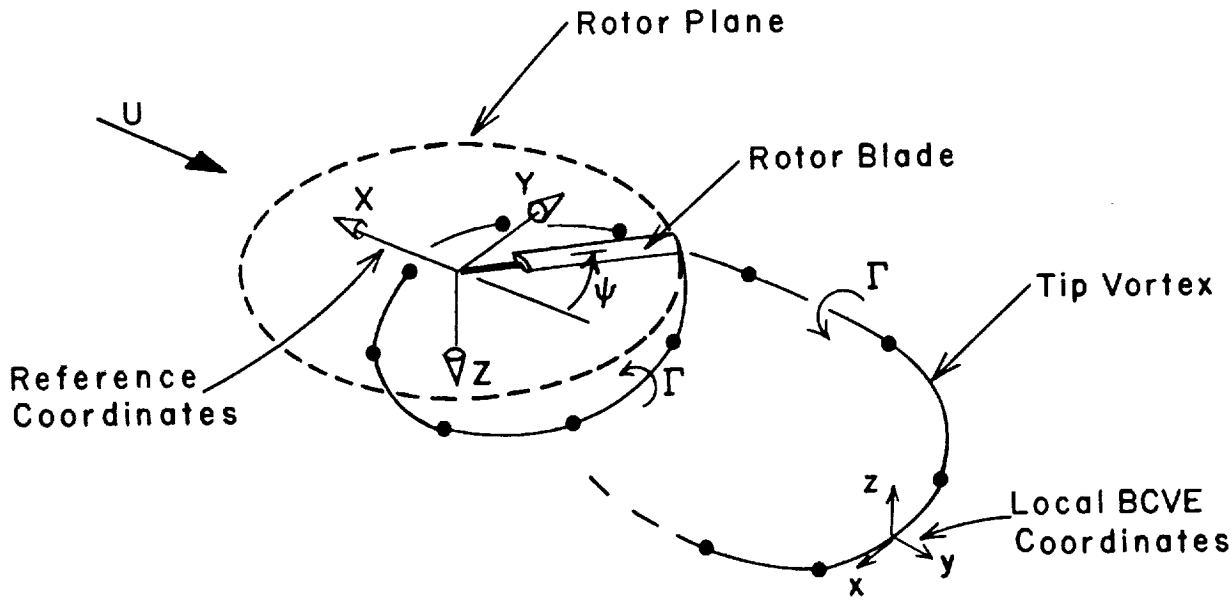

Figure 22. Coordinate systems for the forward flight analysis.

particular BCVE are then performed, transformed back to reference coordinates, and appropriately stored. The process is repeated for every other element. The velocity induced at any given point is not fully determined until the contributions of all the elements have been found. This particular calculation sequence appears to be the fastest approach computationally.

The free wake analysis is then implemented in the traditional time stepping manner. In each time step, the blade moves through an angular increment $\Delta\psi$ and lays down an additional vortex element between the previous collocation point (which was on the blade) and the present blade location. At the same time, the last element in the free wake is discarded to keep the total number of free wake elements constant. This process is illustrated in Figure 23. The displacements of all the collocation points in the wake are calculated from the velocity vectors induced at these points and the time step associated with the change in blade position. The motion of the collocation points is followed in a purely Lagrangian sense in the reference Cartesian system moving with the rotor, shown in Figure 22. The velocity at the free wake collocation points is produced by the free stream, the bound vorticity on the blades, the free wake itself (BCVE and SIVE elements), and by the far wake.

The time evolution is calculated using a predictor-corrector scheme[20] to ensure higher order accuracy as well as stability. Accuracy is particularly important since using large elements means rather large time steps and correspondingly large rotations of the rotor blade tips. The stability of the method also benefits greatly from the fact that the last free wake element is discarded at each time step. The wake behavior is largely dominated by the convective effects of blade rotation and forward flight. Wake distortions and errors in the solution are effectively swept down the wake. Repeatedly discarding the last element provides a way to remove these disturbances from the free wake; otherwise errors might accumulate at the junction between the free and the far wake. The far wake is recalculated at each time step so that it always connects smoothly with the remaining free wake, again see Figure 23.

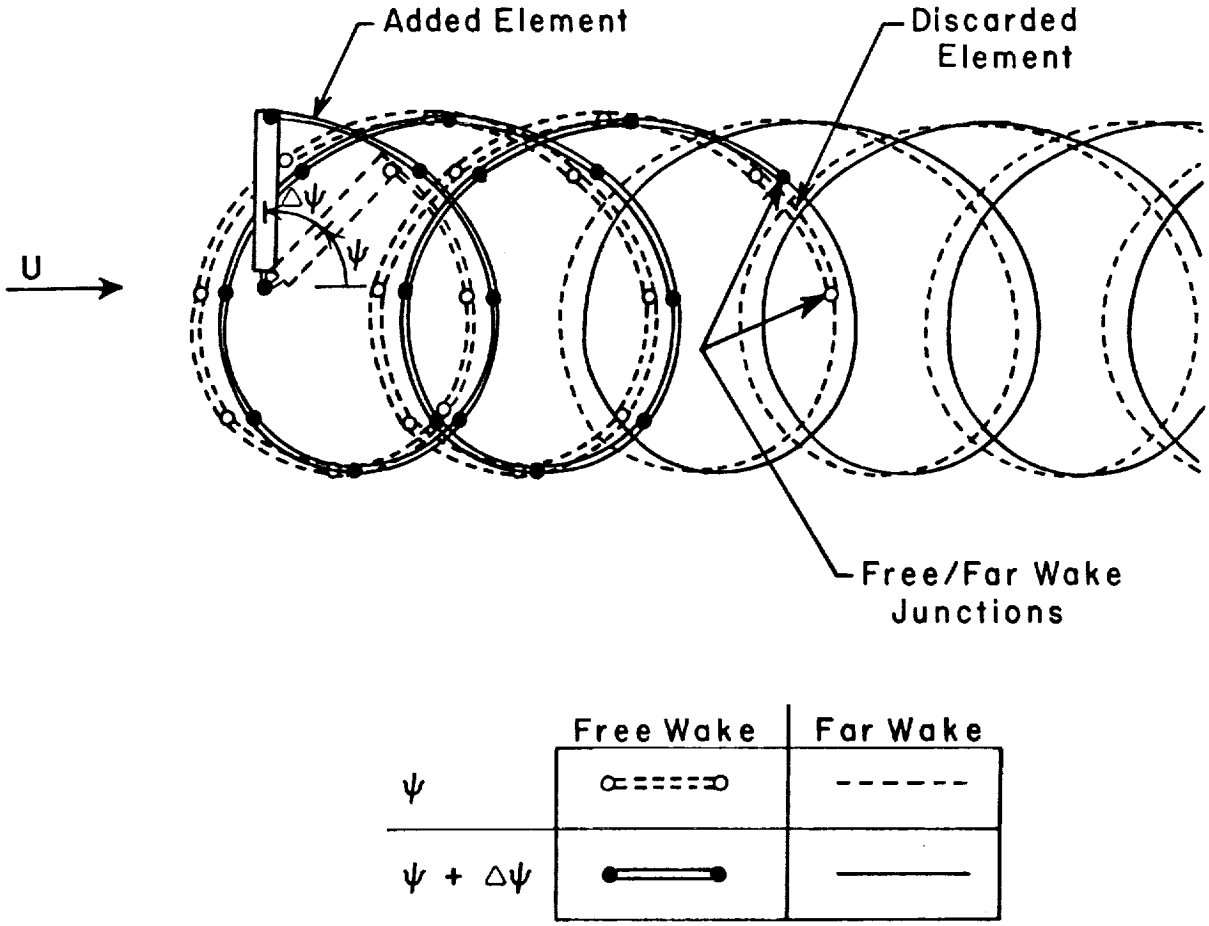

Figure 23. Time stepping procedure for the free wake calculation.

The idea that disturbances are swept down the wake (when viewed in the reference frame moving with the rotor) has been confirmed by visual examination of the step-by-step evolution of solutions. Furthermore, solutions do not fully converge until the number of rotor revolutions exceeds the number of free wake turns, i.e., the convergence time exceeds the time for disturbances to convect out of the free wake region. Convergence is said to occur when the positions of the collocation points repeat from turn to turn, to within some specified accuracy. As expected, points near the blade settle down first. Velocities induced at the blade may be quite repeatable even before the downstream end of the free wake converges. Although systematic studies of convergence have not been performed, the curved element method seems to behave extremely well in this regard. The collocation point locations converge rapidly to nearly repeatable values after a few blade turns. Generally, it is not difficult to decide when the solution is effectively converged. It is also worth noting that the curved element method seems to be quite robust, with converged solutions being obtained relatively quickly, even from a poorly chosen initial wake shape.

In the current free wake analysis none of the possible short cuts to reduce computer time were used. The effect of every point on every other point is recalculated without further approximation at every time step, i.e., full velocity updating is used. Unlike some other free wake analyses, no distinction is made between near and distant points in terms of whether or not to update their effect at every time step. Also, the tip vortex from every blade is treated as a separate entity. This unoptimized treatment reflects a conservative approach to the first implementation of a new method. In any event, at least in this basic analysis, the free wake calculation procedure is sufficiently efficient that further optimization to reduce computer time has not been necessary. The point is not that such approximations are invalid, but rather that the free wake computer program could be made even more efficient by their implementation. In fact, the use of curved elements considerably expands the opportunities for optimization. For example, the unique capability to use very large element sizes in certain parts of the wake to improve efficiency has yet to be explored.

4.2 Forward Flight Far Wake

The forward flight analysis necessarily involves a finite number of turns of free wake. For several reasons it is necessary to continue the wake with a far wake* model beyond the free wake region. The velocity induced by the far wake region has a significant effect on the evolution of the free wake, as well as some direct effect on the velocity field at the rotor blades. If the free wake were simply terminated, the flow field would be kinematically incorrect and the downstream end of the free wake would not converge. It is, therefore, important to develop an accurate far wake model which does not adversely affect the free wake convergence.

As each successive turn of rotor wake is shed from the blade and passes downstream, its subsequent motion can be thought of as a combination of overall convection and local distortion. The dominant convection effects are the free stream velocity and the net downwash from the remainder of the wake and the rotor itself. The distortion occurs largely as the result of the nonuniform flow induced by the vortex on itself, and is primarily associated with the collapse and tendency to "roll-up" of the wake tube, which rapidly takes on the appearance of a vortex pair downstream of the rotor. This behavior is apparent in the numerical simulations discussed later. Once this rapid initial distortion has occurred, typically within the first couple of wake turns behind the blades, the subsequent distortions appear to be confined primarily to the details of the roll-up region, where the concentration of vorticity is highest.

The far wake model is based on the idea that the best estimate of the shape of a far wake turn is the shape of the last free wake turn. One blade revolution later, the vortex represented by the last free wake turn would then occupy the position of the first far wake turn. This assumption corresponds

---

* In this report the term "far wake" applies to the region of wake downstream of the free wake. In some literature, however, this term is used to mean those portions of the free wake distant from the point of evaluation in a partial updating optimization scheme.

to freezing the shape after the last free wake turn. The effect of subsequent downstream distortion is, therefore, not included, and only convection in an average sense is taken into account. This approximate shape is best for the first few far wake turns, since there has been relatively little time for subsequent distortion. Neglecting this distortion in the far wake turns that are farther downstream makes little difference since the influence of their detailed shape is less crucial because they are farther away.

Given this model for the far wake, the problems to be resolved are the determination of the direction in which the wake is convected, and the development of an efficient method to sum the infinite number of repeated turns of far wake. The mean convection direction is determined by comparing the positions of the last and next to the last turns of free wake. The change in position of each set of corresponding points on these two turns is computed. These position differences between pairs of points, originally generated at the same blade azimuthal location, defines a displacement vector. A running average of all these displacement vectors, generated while stepping the blade through the previous full turn, is computed to determine an average displacement vector. This average displacement vector, $\vec{r}_s$, is taken to represent the average displacement per blade revolution of a wake turn due to overall convection. It is used to orient the successive far wake turns in space. The purpose of the running average over a cycle is to filter out the distortion effects that are superimposed on this mean convection.

The far wake configuration is illustrated in Figure 24. The far wake can be thought of as being composed of a set of semi-infinite rows of elements running in the direction of $\vec{r}_s$, one of which is shown in the figure. It is possible to sum the contributions of each row in an efficient manner by using the discrete approximation for the Biot-Savart law.* Consider one element

* In Section 3.2 this approximation was shown to work well for straight-line segments, and it can also be shown to work for curved elements at a distance if the correct equivalent strength is used.

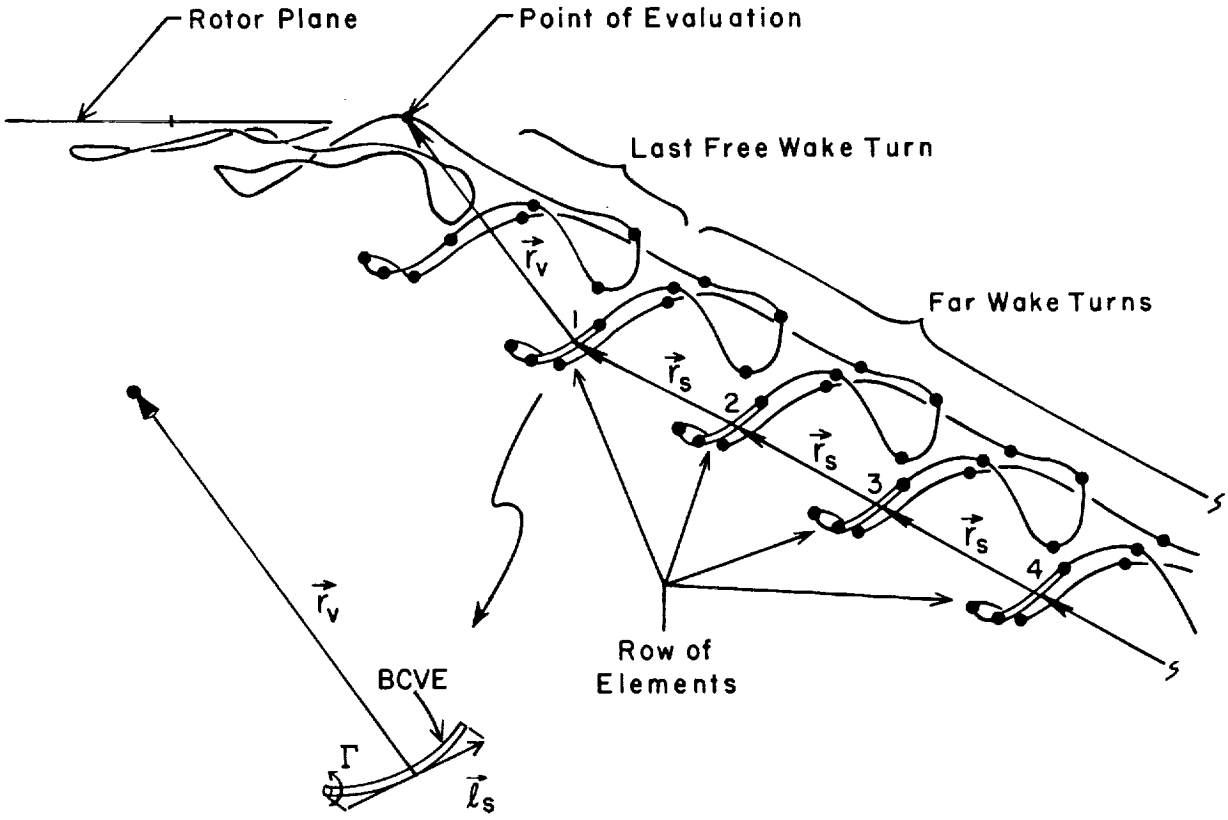

Figure 24. The far wake geometry showing one of the semi-infinite rows of elements.

from the semi-infinite row, as shown in detail in Figure 24. Provided the distance to the point of evaluation is considerably greater than the element length, the following approximation is reasonably accurate,

$$\vec{q}_{element} = -\frac{\Gamma}{4\pi} \int_{element} \frac{\vec{r}_v(s) x d\vec{s}}{|\vec{r}_v(s)|^3} \approx -\frac{\Gamma}{4\pi} \frac{\vec{r}_v x \vec{\ell}_s}{|\vec{r}_v|^3} \tag{58}$$

where $\vec{r}_v$ is interpreted as the distance from the center of the element in the final expression on the right. The vector $\vec{\ell}_s$ describes the element orientation and effective length. This simplified form can now be used to sum all the contributions from the element row, namely

$$\vec{q}_{row} \approx -\frac{\Gamma}{4\pi} \sum_{n=1}^{\infty} \frac{[\vec{r}_v + (n-1)\vec{r}_s] x \vec{\ell}_s}{|\vec{r}_v + (n-1)\vec{r}_s|^3} \tag{59}$$

where $\vec{r}_v$ is the distance from the first element to the point of evaluation. After some manipulation the following equivalent form is obtained

$$\begin{aligned} \vec{q}_{row} = &-\frac{\Gamma}{4\pi} \frac{\vec{r}_v x \vec{\ell}_s}{|\vec{r}_v|^3} \left\{ 1 - |\vec{r}|^3 \sum_{n=3}^{\infty} \frac{n-2}{|\vec{r}_v + (n-1)\vec{r}_s|^3} \right\} \\ &-\frac{\Gamma}{4\pi} \frac{(\vec{r}_v + \vec{r}_s) x \vec{\ell}_s}{|\vec{r}_v + \vec{r}_s|^3} \left\{ 1 + |\vec{r}_v + \vec{r}_s|^3 \sum_{n=3}^{\infty} \frac{n-1}{|\vec{r}_v + (n-1)\vec{r}_s|^3} \right\} \end{aligned} \tag{60}$$

Now, the velocity contributions from the first and second elements in the row are

$$\vec{q}_1 \approx -\frac{\Gamma}{4\pi} \frac{\vec{r}_v x \vec{\ell}_s}{|\vec{r}_v|^3} \qquad \text{and} \qquad \vec{q}_2 \approx -\frac{\Gamma}{4\pi} \frac{(\vec{r}_v + \vec{r}_s) x \ell_s}{|\vec{r}_v + \vec{r}_s|^3} \tag{61}$$

In practice, the infinite summations in Eq. (60) can be replaced by integrals for $n > m$, where m is sufficiently large that the integral approximation holds. Thus, the velocity contribution of a far wake row is

$$\vec{q}_{row} = \vec{q}_1 \left\{ 1 - |\vec{r}_v|^3 \left[\sum_{n=3}^{m-1} \frac{n-2}{|\vec{r}_v + (n-1)\vec{r}_s|^3} + \int_{m-1/2}^{\infty} \frac{(n-2)dn}{|\vec{r}_v + (n-1)\vec{r}_s|^3} \right] \right\}$$

$$+ \vec{q}_2 \left\{ 1 + |\vec{r}_v + \vec{r}_s|^3 \left[\sum_{n=3}^{m-1} \frac{n-1}{|\vec{r}_v + (n-1)\vec{r}_s|^3} + \int_{m-1/2}^{\infty} \frac{(n-1)dn}{|\vec{r}_v + (n-1)\vec{r}_s|^3} \right] \right\} \tag{62}$$

The above result shows that the velocity for the entire row can be found in terms of $\vec{q}_1$, $\vec{q}_2$, $\vec{r}_v$ and $\vec{r}_s$. In practice, the effect of two turns of far wake is found using BCVE's to determine $\vec{q}_1$ and $\vec{q}_2$ for each row of elements. Hence the approximation of Eq. (58) is actually not invoked until the third far wake turn. The effect of an infinite number of far wake turns is then obtained by multiplying the $\vec{q}_1$ and $\vec{q}_2$ for each row by the factors in brackets above. The approach has proved to be very efficient in practice.

The far wake model has been successfully implemented into the forward flight computer program. A smooth, stable transition between the end of the free wake and the beginning of the far wake has been achieved. This is especially remarkable because the far wake and free wake typically overlap and may be considerably intertwined, particularly at lower advance ratios. The success of this approach indicates that the physical ideas underlying the far wake modelling are essentially correct.

Since the far wake structure is based on free wake information, the far wake shape evolves along with the free wake solution. Note that there is a different far wake shape at each time step in the solution. The far wake configuration also adjusts automatically to the rotor flight condition. An indication of the success of the method is that in the forward flight wake shapes presented later it is quite difficult to tell where the free wake ends and the far wake begins.

4.3 Close Encounters Between Vortices

In the evolution of the free wake solution, large distortions occur in the tip vortex filament. As will be seen, these distortions are particularly strong along the sides of the wake which tend to roll-up forming a pattern that looks like a trailing vortex pair downstream. As a result, turns of the vortex wake that were not initially close together may experience close encounters. The frequent occurrence of these close encounters provides a strong justification for the curved vortex element method which retains its accuracy at points close to the filament. In the rapidly distorting and stretching roll-up regions, the local radii of curvature are often much smaller than the rotor radius, and initially small elements may stretch to encompass large arc angles. The evidence presented previously suggests that the use of straight-line elements in this region would introduce errors unless the elements were much smaller than normally used.

Another problem associated with extremely close encounters is of practical significance. When a collocation point falls very near another vortex element, very large velocities can be induced. This behavior is not only physically incorrect, but also causes problems in the numerical method since the particular point may experience extremely large displacements in a single time step. It is clearly necessary to introduce the effect of the vortex core.

The tip vortex is formed by the vortex sheet shed from the blade tip region beyond the point of maximum lift. The initially flat sheet rolls-up into a spiral structure. Viscous effects dominate the high velocity center portion of this region, forming a viscous vortex core in solid body rotation. Outside the viscous core is the vorticity from the rest of the spiral sheet. An analytical prediction of the circulation distribution outside the viscous core is given by the Betz roll-up model.[21,22] The Betz core structure is determined by assuming conservation of angular momentum during the sheet roll-up process. The swirl velocity distribution depends on the initial strength distribution of the vortex sheet, and thus, on the load distribution at the tip of the blade. In most cases, the swirl velocity

distribution in the Betz core must be calculated numerically. Fortunately, for the important case of elliptical loading a simple curve fit approximates the numerical solution with considerable accuracy.[23]

An alternative approach is to use an empirically determined vortex core structure. A recent experimental study[24] has shown that a wide range of cases can be represented by a three part empirical core model. The three parts consist of a solid body rotation region at the center, an intermediate turbulent mixing region, and an outer transition region associated with the remaining spiral vortex sheet. Reference 8 reviews some additional approaches to vortex core structure.

In general, the swirl velocity distribution in a vortex core is given by

$$q = \frac{\Gamma(r)}{2\pi r} \tag{63}$$

where $\Gamma(r)$ is the circulation as a function of radius. For a constant vorticity core

$$\Gamma(r) = \Gamma_v \left(\frac{r}{a_v}\right)^2 \qquad r \leq a_v \tag{64}$$

where a_v is the core radius and Γ_v is the circulation at the core boundary. This circulation distribution is sometimes used for convenience to describe the entire vortex core, and indeed it provides a good approximation to the swirl velocity distribution throughout much of the viscous core region.[24]

To illustrate the construction of a more realistic composite vortex core, the Betz roll-up model will be used. The approximate form for the Betz core produced by an elliptical load distribution[23] is

$$\Gamma_B(r) = \Gamma\left[2\,\frac{r}{a_B} - \left(\frac{r}{a_B}\right)^2\right]^{1/2} \qquad r \leq a_B \tag{65}$$

where Γ is the total circulation, and a_B is the Betz core radius. If the distance between the point of maximum blade load and the tip is b_t, then it can be shown that $a_B = \frac{\pi}{4}\, b_t$ for elliptic loading. The load distribution on the tip of a conventional helicopter blade can resemble an elliptical distribution.[25] A composite vortex core can be constructed with an inner viscous core modelled as a constant vorticity region surrounded by a Betz core. For this composite core,

$$\Gamma(r) = \begin{cases} \Gamma\left(\frac{r}{a_v}\right)^2 \left[2\,\frac{a_v}{a_B} - \left(\frac{a_v}{a_B}\right)^2\right]^{1/2} & 0 \leq r \leq a_v \\ \Gamma\left[2\,\frac{r}{a_B} - \left(\frac{r}{a_B}\right)^2\right]^{1/2} & a_v < r \leq a_B \\ \Gamma & r > a_B \end{cases} \tag{66}$$

where $a_B = a_c$, the vortex core boundary. This result combined with Eq. (63) gives a distribution of swirl velocity as shown in Figure 25. The constant a_v must be specified from experimental data and a_B depends on the blade load distribution; typically $a_B >> a_v$. An alternative composite core is the three region empirical model of Ref. 24. Interestingly, both this empirical core and the present model indicate that $a_c >> a_v$. In the demonstration calculations presented later in this section, a simple constant vorticity core was assumed because detailed blade loading calculation were not made.

The above approach can be used as a basis to adjust the velocity induced at a collocation point experiencing a close encounter with a nonadjacent element on the vortex. If the distance between the element and the point is less than the core size, then the core swirl velocity distribution can be used

C-2

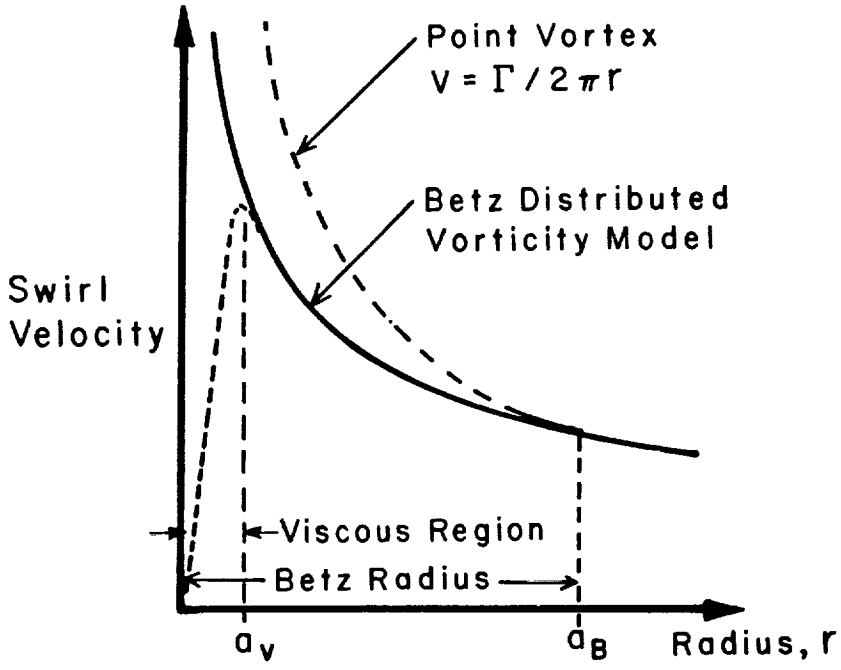

Figure 25. Composite core swirl velocity distribution.

to adjust the induced velocity, as described shortly. However, it should be noted that any approach of this type is necessarily approximate. In actuality, the occurrence of overlapping vortex cores may lead to physical phenomena beyond the scope of current free wake analyses. For instance, the merging or pairing of vortices is now a reasonably well known process in certain vortical flows. It is entirely possible that such effects take place commonly in the roll-up regions on the sides of the wake. The intertwined vortices on the sides may well merge to form a trailing vortex pair. In the present analysis, cores may pass through each other but cannot merge. However, in the absence of these complex viscous effects, it is hoped that the analysis still preserves the local centroids of motion to some reasonable degree, and the average effects of merging vortices (if this merging actually does occur) is adequately represented, at least as seen by other parts of the wake.

The correction to the velocity at a collocation point induced by a nearby vortex element is now considered. Because this correction is necessarily an approximation in the absence of real viscous interaction between the cores, it is reasonable to develop the correction itself in an approximate manner. Figure 26 shows a collocation point located very close to a BCVE. The approach involves first finding the minimum distance r_m from the filament to the collocation point. Then the ratio of the vortex core swirl velocity to the point vortex swirl velocity is used as a factor to reduce the velocity originally calculated at the collocation point. This type of correction can reasonably be applied because the local vortex flow field appears very nearly two-dimensional within the vortex core, even when the filament is curved.

The maximum velocity in the potential flow region around a curved element occurs at the edge of the vortex core. This core edge velocity is approximately

$$q_e \approx \frac{\Gamma}{2\pi a_c}\left\{\frac{x+\ell}{\sqrt{(x+\ell)^2+a_c^2}} - \frac{x-\ell}{\sqrt{(x-\ell)^2+a_c^2}}\right\} \qquad (67)$$

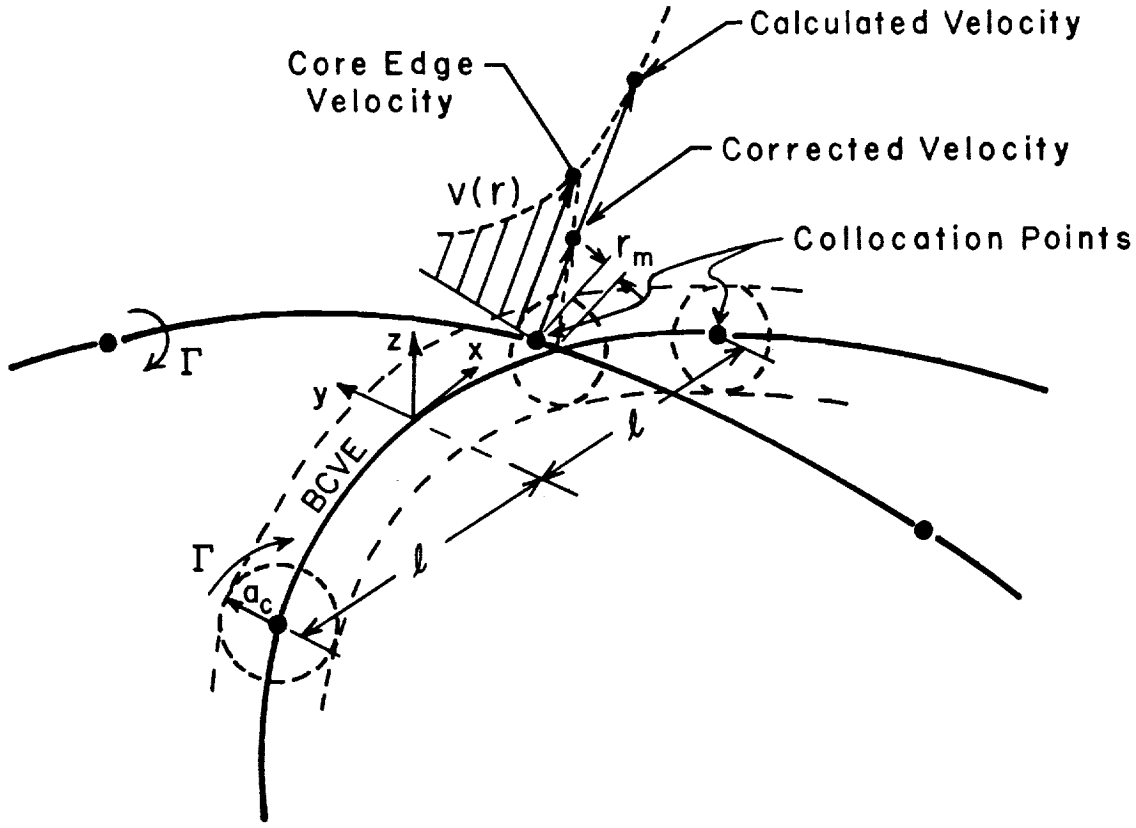

Figure 26. Treatment of close encounters between two vortex filaments.

where a_c is the core radius, x is the collocation point location in the local coordinate system of the nearby element, and ℓ is one-half the distance between the end points of the element. The function of x in brackets has been introduced because the element does not induce the full two-dimensional value of swirl velocity when the collocation point is near an end of the element, and because the element is of finite length. For instance, when the collocation point is next to the end of the element, the induced velocity is about half the two-dimensional value. The function in brackets actually comes from the straight-line element formula. The analytical work on accuracy discussed earlier can be interpreted to show that a straight-line element works reasonably well at close distances, if it is located at the proper radial distance from the point of evaluation. This function of x is convenient, and certainly accurate enough for the present purpose. This is not equivalent to making straight-line element type errors since the proper radial location (radial distance equal to core radius) is used.

The procedure to correct for close encounters is as follows. The essential features are illustrated in Figure 26. It is cumbersome to actually determine the minimum geometric distance, r_m, from a collocation point to a curved element (note that the minimum distance is not the distance between the nearest collocation points). Instead, the minimum distance is deduced from the calculated velocity. The velocity induced at each collocation point by a given BCVE is calculated. If the magnitude of one of these velocities, called q_m, exceeds the core edge velocity, q_e, from Eq. (67), then the corresponding collocation point is within the core region of the BCVE and the correction procedure is used. The velocity q_m very near a BCVE can be estimated as

$$q_m \approx \frac{\Gamma}{4\pi r_m} \left\{ \frac{x + \ell}{\sqrt{(x + \ell)^2 + a_c^2}} - \frac{x - \ell}{\sqrt{(x - \ell)^2 + a_c^2}} \right\} \tag{68}$$

where r_m is the minimum radial distance from the BCVE to the collocation point. As a simplification, the core radius a_c, rather than r_m, is used in the function in brackets. The difference is unimportant to within the

accuracy of the approach. Using Eqs. (67) and (68) to solve for r_m gives

$$r_m = a_c \frac{q_e}{q_m} \tag{69}$$

This radius can now be used in Eqs. (66) and (63) to determine the actual core swirl velocity, q_c . A correction factor for close encounters can now be defined as

$$\gamma_c = \frac{q_c}{q_m} \tag{70}$$

This correction factor is applied to reduce the velocity vector $\vec{q}_m$ calculated originally. The close encounter correction is required whenever a free wake collocation point falls too near a curved element in either the free wake or the far wake.

4.4 Sample Calculations

This subsection describes various sample calculations which illustrate the behavior of forward flight free wake solutions using the curved vortex element method. The results shown are for a simplified demonstration model having only a tip vortex free wake, a far wake, and constant bound circulation on the blades. This simplified model focuses on the behavior of the free tip vortex which is the primary feature of interest. In these calculations, the rotor plane is horizontal and aligned with the free stream flow. There is no dynamic blade motion and no consideration of flight trim for the rotor. This basic free wake demonstration program was developed to run on an IBM personal computer.

Figure 27a,b,c,d shows the evolution of a solution for a one-bladed rotor at advance ratio $\mu = .075$ with five turns of free wake with elements

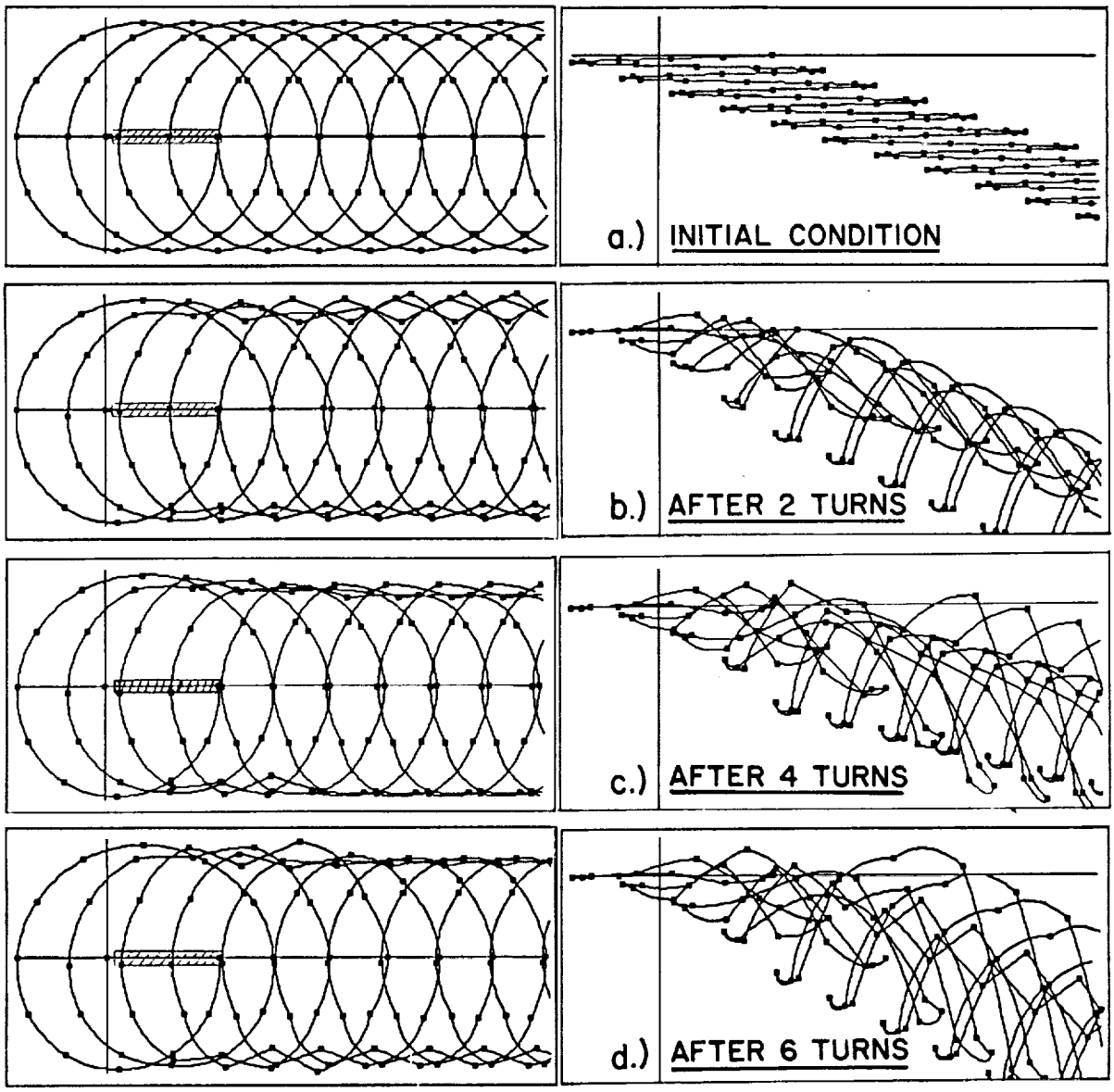

Figure 27. Evolution of a free wake solution for a one-bladed rotor with 5 turns of free wake at $\mu = .075$ - after zero, two, four, and six blade revolutions.

generated at every 30° of blade rotation. The results are shown at every two complete blade turns. The solution is nearly converged after six blade turns since there has been time to wash the incorrect initial shape out of the free wake. The solution is started from a skewed cylindrical form, from which significant distortions rapidly occur. Note that the vertical scale is expanded by a factor of 3.0 to show the structure of vertical displacements clearly. This scale expansion and the action of the plotting routine sometimes make the changes in wake shape from point-to-point appear abrupt, which is actually not the case with the curved element method.

The wake evolution seen in this sequence of figures illustrates an important aspect of this free wake method, which is its robust, stable nature in converging to a solution. Even from a poor starting point, the scheme evolves rapidly towards the solution. There seems to be a distinct absence of numerical instability problems with this method. This may be due in part to the use of curved elements, and to the interpolated point element connection scheme which guarantees a degree of smoothness in fitting the elements between the collocation points. The accuracy of these methods may help prevent spurious behavior in the evolving wake.

As Figure 27d shows, the primary characteristic of the wake distortion is the roll-up tendency of the overlapping vortex turns on the sides of the wake. In the present calculation this effect carries the tip vortex up through the rotor disk plane on the advancing and retreating sides. As will be seen, this interaction between the vortex turns along the sides of the wake produces a downstream flow field that looks very much like a trailing vortex pair. The concentration of vorticity along the sides tends to wash the center of the wake downward, producing a characteristic pattern in the side view. The turns which face forward, generated around $\psi = 180°$ become the forward facing loops seen in the side view at the lowest part of the wake. The turns which face rearward, generated around $\psi = 0°$, form the rearward facing loops near, or just above, the bottom of the wake. Farther back in the wake the vertical separation between the forward and rearward loops is seen to diminish. Essentially, the tube-like wake of the starting solution collapses in the middle due to roll-up along the side edges. This behavior is

most clearly seen at lower advance ratio, and for larger numbers of rotor blades, since in both cases there are more overlapping vortices along the sides of the wake.

The corresponding case of a one-bladed rotor at advance ratio $\mu = 0.15$ is shown in Figure 28. In this calculation there were 2-1/2 turns of free wake with elements generated at every 22.5° of blade rotation. Note that the vertical scale expansion is about 5.0 in this figure, so that in actuality the wake is flatter and does not descend as rapidly as in the previous case. Doubling the advance ratio halves the density of vortices in the wake. The top view shows much less distortion of the vortices along the sides of the wake. Some roll-up tendency is still evident in the front and side views, which show upward displacement and distortion of the sides of the wake. There are discernible differences in the distortions seen on the advancing and retreating sides. These differences are associated with the side-to-side asymmetry of the wake as seen in the top view. This asymmetry becomes more pronounced as advance ratio increases. The downward displacement of the center of the wake also shows a degree of asymmetry. The characteristic forward and backward facing loops mentioned earlier are still clearly evident.

In the results just shown, as well as those to be presented, the successful treatment of the far wake is to be noted. No irregularity at the transition between the free and far wake can be seen and in fact the transition point is hard to identify without carefully counting the free wake turns. The numerical output shows no problem with convergence in this transition region. Visually, the generated far wake shape appears quite consistent with the form of the free wake. Because of the overlapping nature of the wake, there is significant intermingling between free wake and far wake turns, but this does not have an adverse effect on free wake convergence. In all respects, the method of treating the far wake is judged to be quite successful.

Next consider a set of results for a two-bladed rotor. Figure 29 shows the solution at $\mu = .08$ for three turns of free wake from each blade. Note that the vertical scale is expanded by a factor of 2.25. The wake elements

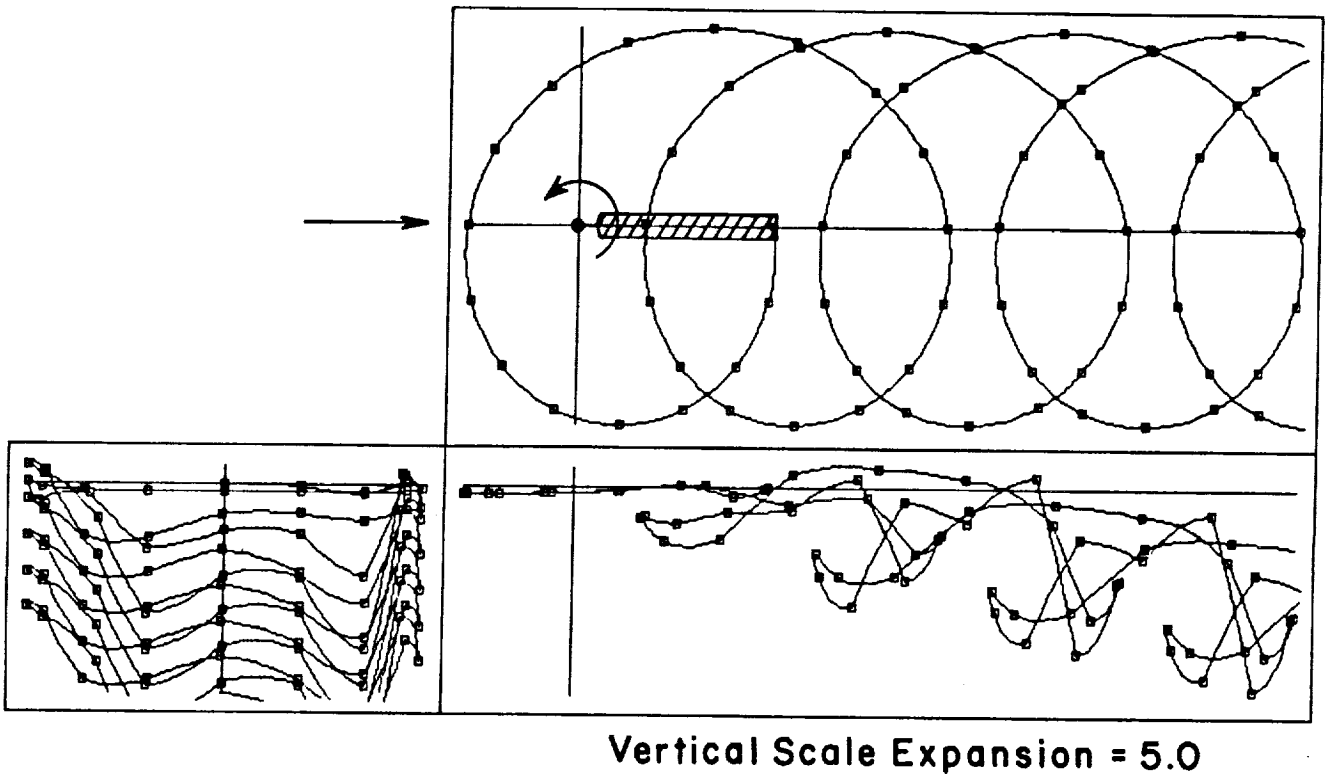

Figure 28. Solution for a one-bladed rotor with 2-1/2 turns of free wake at $\mu = .15$ after five blade revolutions.

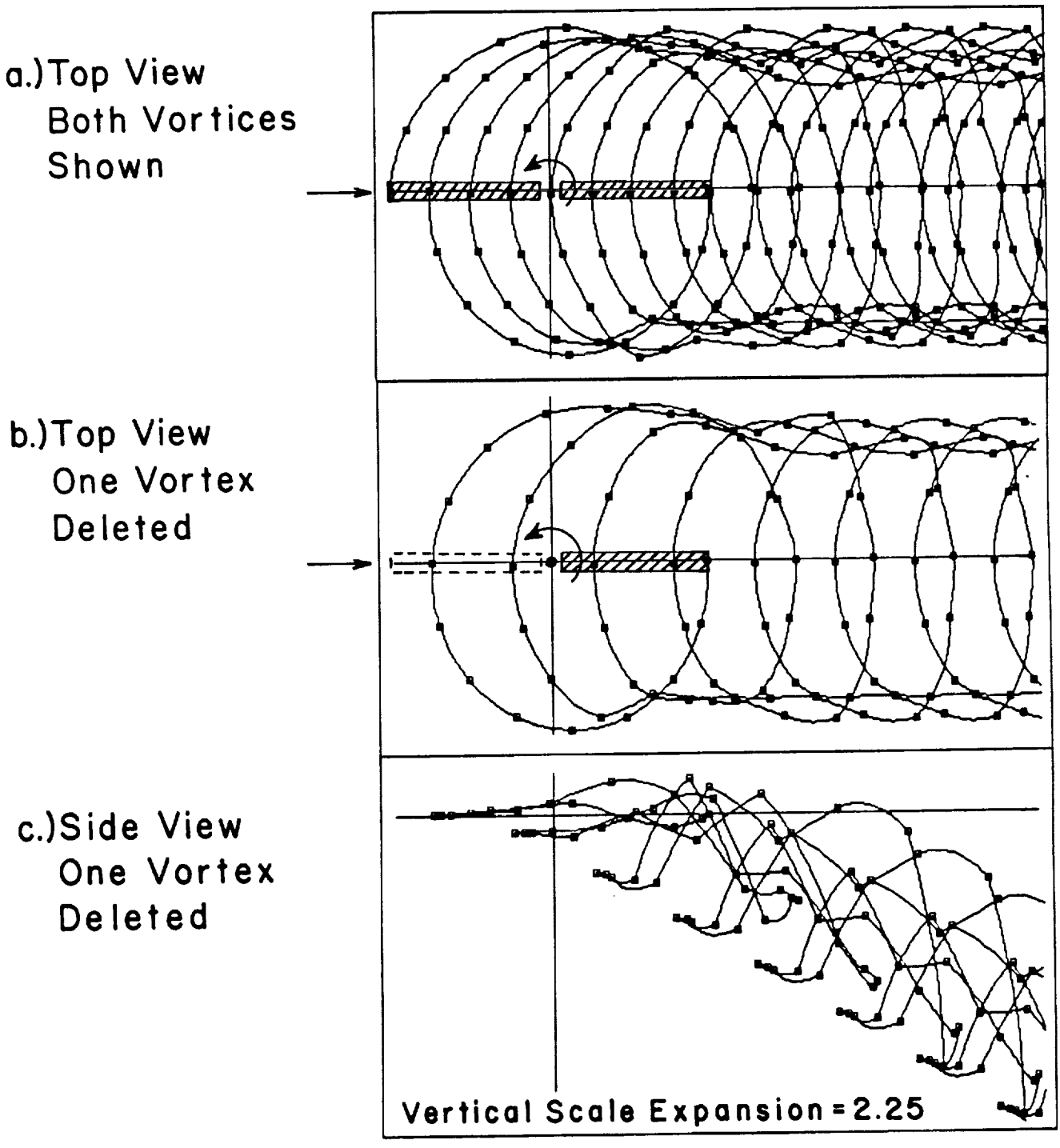

Figure 29. Solution for a two-bladed rotor with 3 turns of free wake at μ = .08 - after five blade revolutions.

are generated at every 22.5° of blade rotation. It is immediately apparent that the addition of a second tip vortex enhances the roll-up effect. The top view, Figure 29a, shows a larger, more entangled region of trailing vortices along the sides, as compared to the previous figures. Although the initial element size is reasonably small, considerable stretching may occur in the roll-up region along with relatively small radii of curvature. It is often possible to find elements in or near this region that have their arc angle, θ_o , more than doubled by this distortion and stretching. The concentrations of vorticity on the sides again wash the center of the wake downward producing the characteristic pattern of hooks or loops at the bottom of the wake as seen from the side.

Figures 29b and 29c show top and side views of the same calculation with one tip vortex deleted for clarity. The shape of each individual vortex actually resembles the one-blade rotor results presented earlier. The structure of the loops near the bottom of the wake is now seen more clearly in the side views. The roll-up type distortion along the sides of the wake is particularly clear in the top views, where the distortion of the overlapping turns gives the appearance of a twisted structure.

Figure 30 shows the corresponding calculation for a two-bladed rotor at advance ratio $\mu = .16$. The roll-up tendency along the sides of the wake is again clearly evident in the top views. Because the higher advance ratio has reduced the degree of overlap of the vortex turns, the roll-up is less pronounced than in the previous figure. The side view shows the roll-up distortions of the sides of the wake and the downward displacement of the forward and rearward facing loops in the center of the wake. In this calculation some secondary distortions caused by interactions between the loops are evident.

Next consider the structure of the crossflow velocity field in the rotor wake. Rotor wake surveys conducted in Ref. 26 showed the rapid formation of a vortex pair flow pattern in crossflow planes downstream of the rotor. This structure was evident immediately behind the rotor, even at fairly low advance ratio. The actual wake descends more slowly than would the skewed tubular

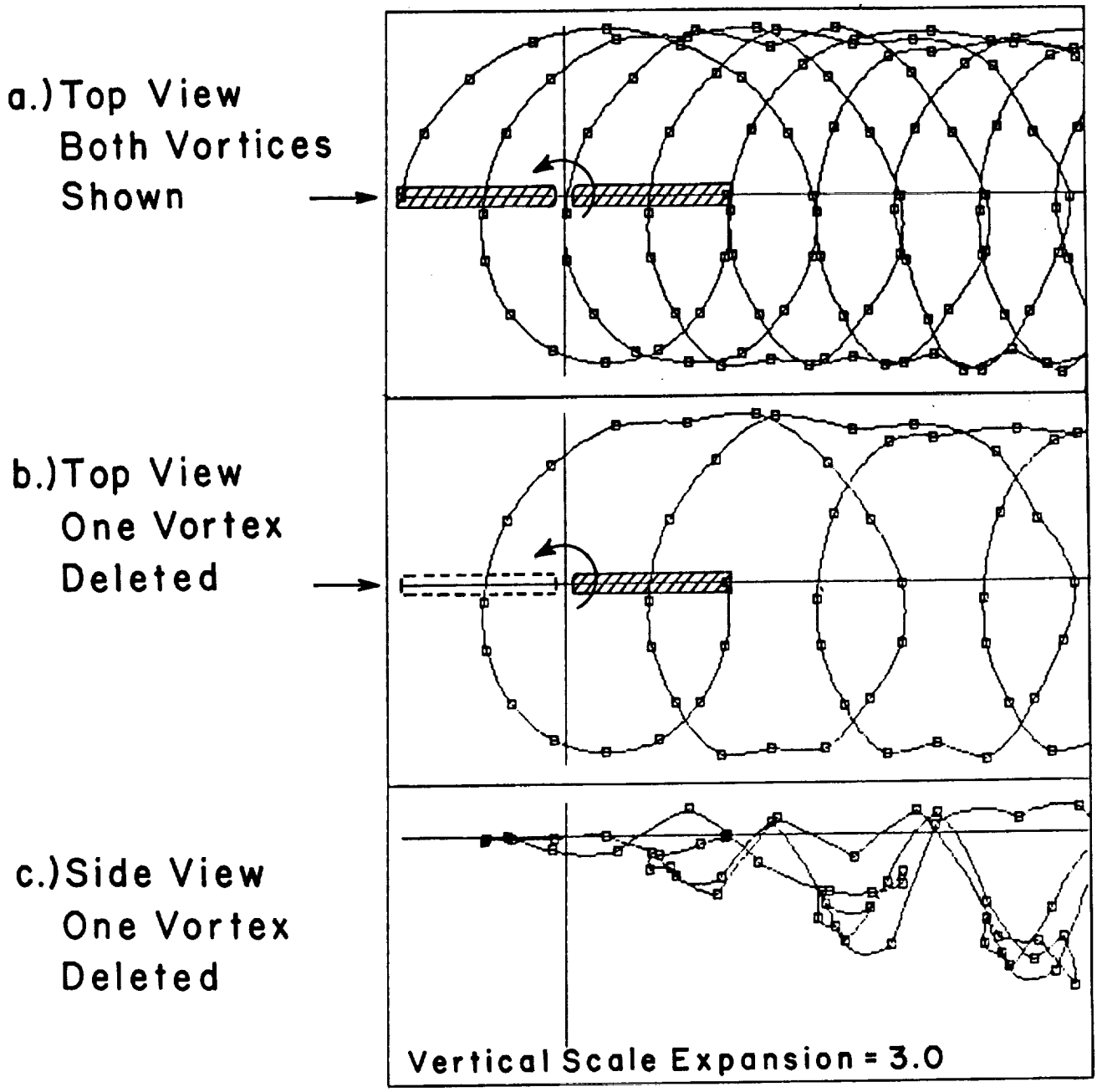

Figure 30. Solution for a two-bladed rotor with 3 turns of free wake at $\mu = .16$ - after five blade revolutions.

wake of momentum theory. Figures 31, 32 and 33 show the instantaneous crossflow velocity field at two downstream stations located at $x = -1.1R_r$ and $x = -2.2R_r$ behind a two-bladed rotor. These three figures present results for $\mu = .08$, $.16$ and 0.4 , respectively. All three cases involve three turns of free wake, with elements generated at every 22.5° increment of blade rotation. There is a definite resemblance between these crossflow results and those obtained experimentally. At the lower advance ratios, the formation of the vortex pair structure immediately behind the rotor is clearly evident. However, at $\mu = 0.4$ the pattern is less clear because there is much less overlap and interaction between the trailing vortices. In all cases the appearance of a trailing vortex pair flow pattern would have been even stronger if the time averaged, rather than instantaneous, crossflow velocities had been computed. Nevertheless, these results support the impression gained from earlier figures that the distorted overlapping sides of the vortex wake are a dominant feature of the flow field.

Finally, the important issue of the effect of element size on the calculated results is addressed. Three sets of calculations for a one-bladed rotor at advance ratio of $\mu = 0.16$ with three turns of free wake are presented. Figures 33a,b,c,d show the downwash velocities induced along the blade at four different azimuthal locations, $\psi = 0°$, $90°$, $180°$ and $270°$. In each case a comparison is made between the use of elements generated by 45°, 30° and 15° increments of blade motion. In this simplified demonstration analysis, only the tip vortex can contribute to the downwash velocity field. For clarity, a top view of the rotor blade and tip vortex position is shown for each azimuthal location. The effect of increasing the element size is surprisingly small, although the most deviation is seen in the 45° case, where the large elements produce some smoothing of the wake shape. In an analysis containing additional effects that contribute to the downwash velocity, e.g., near and inboard wake models, the differences would probably be even less pronounced. Note that the large elements require significantly less computer time. These results suggests that relatively large curved elements can indeed be used to improve efficiency without sacrificing accuracy. However, further systematic study is certainly needed to see if similar results can be obtained for multi-bladed rotors and at lower advance ratios, where local wake distortion is more severe.

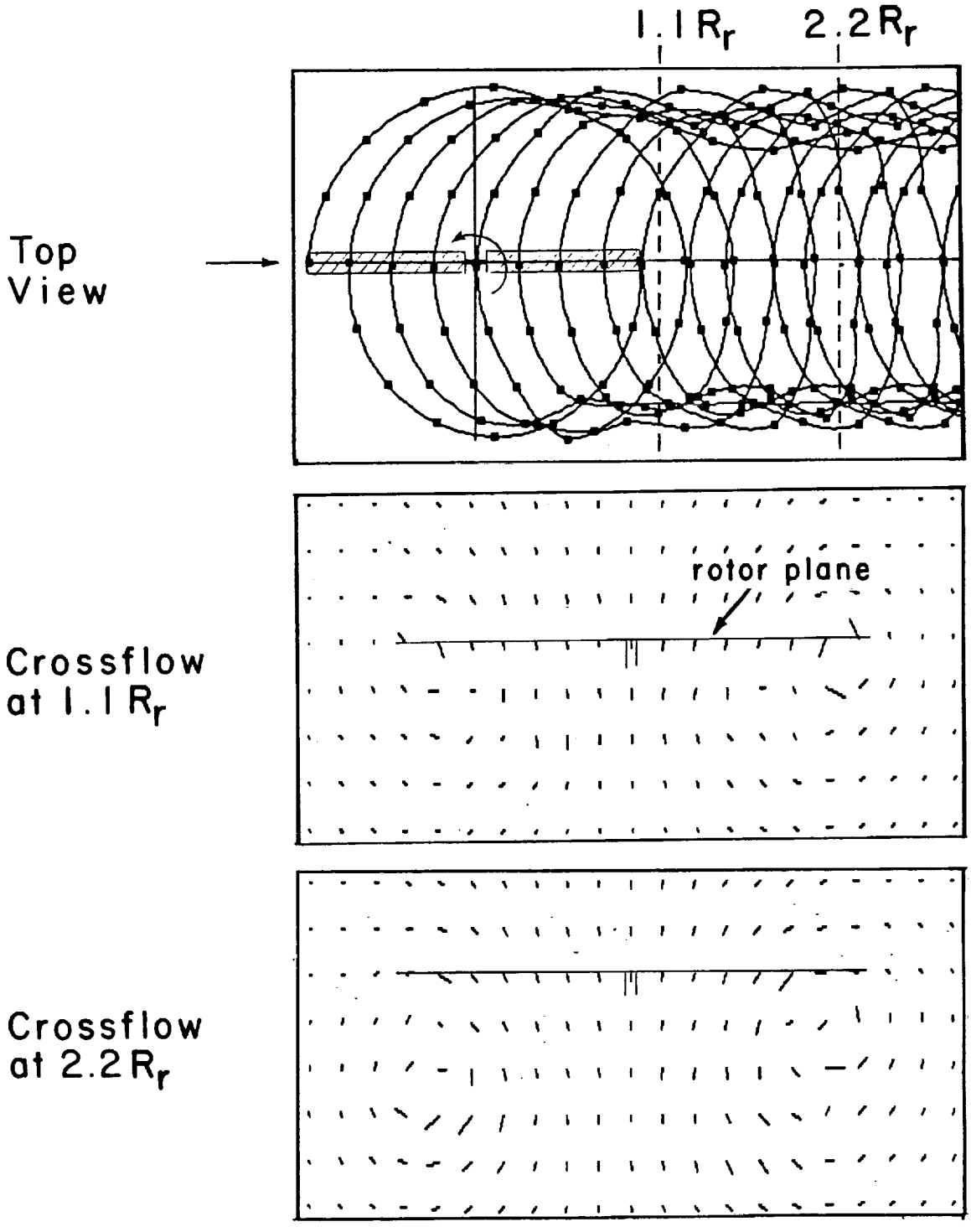

Figure 31. Instantaneous crossflow velocity patterns in planes located at $1.1R_r$ and $2.2R_r$ behind a two-bladed rotor at $\mu = .08$.

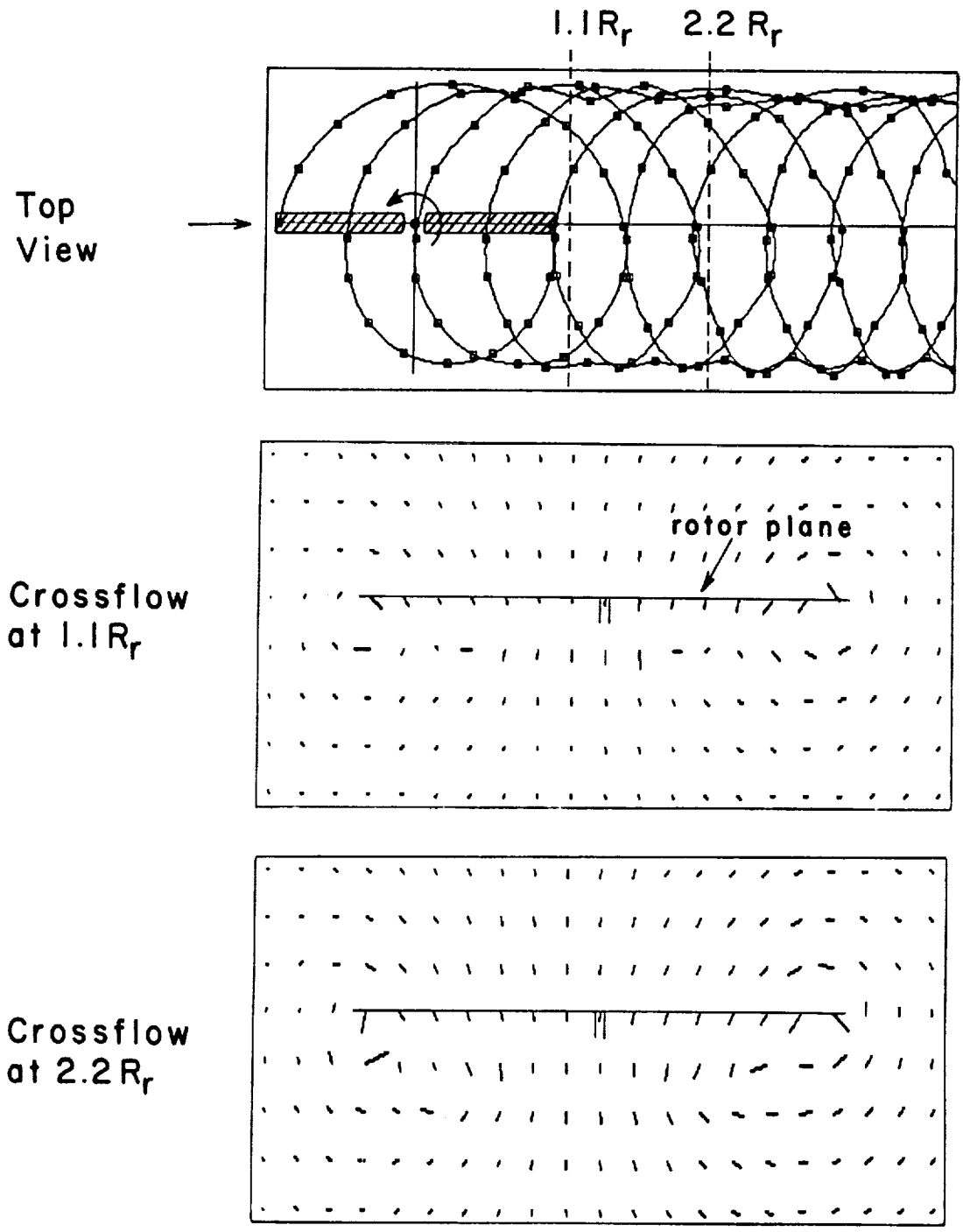

Figure 32. Instantaneous crossflow velocity patterns in planes located at $1.1R_r$ and $2.2R_r$ behind a two-bladed rotor at $\mu = .16$.

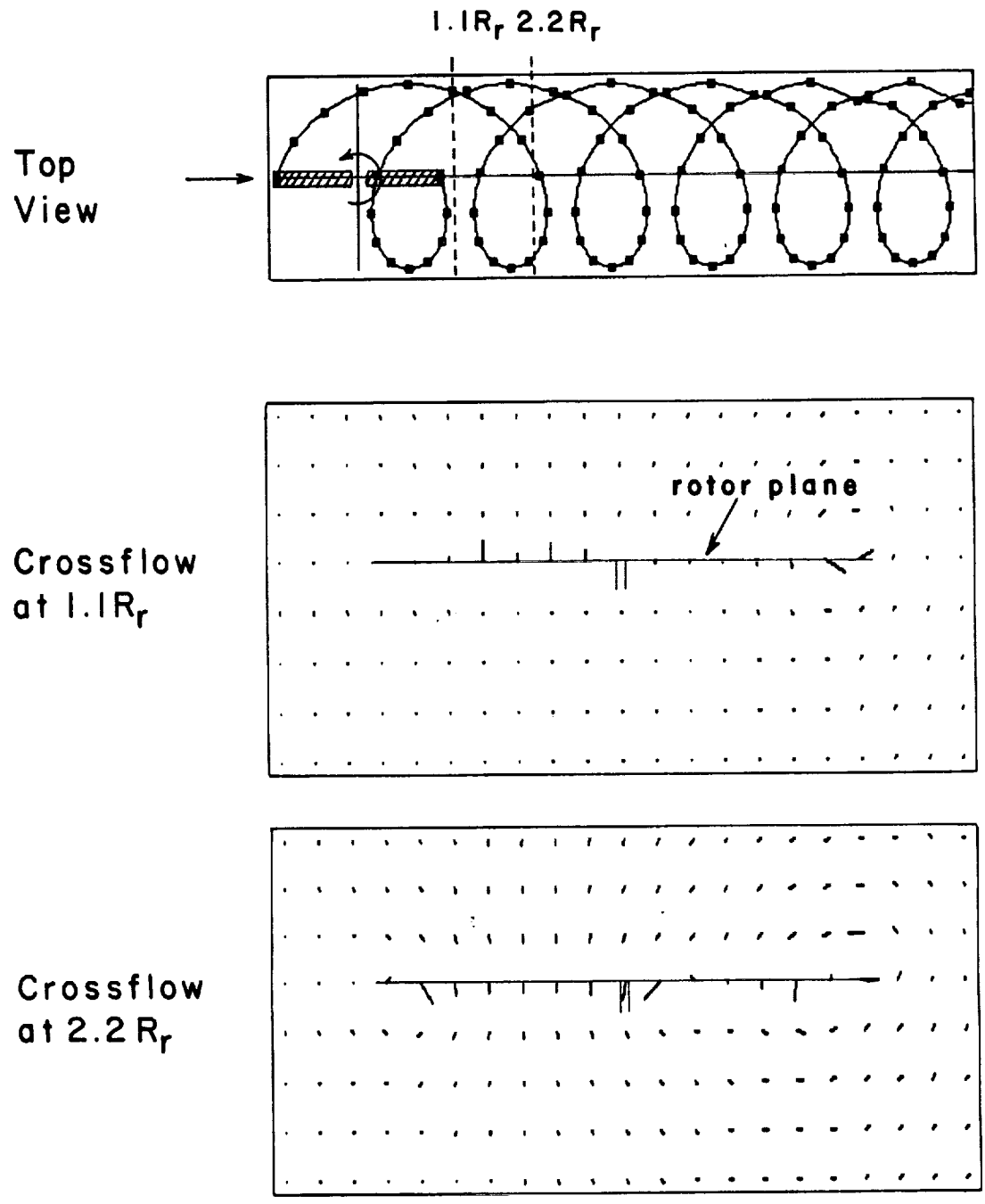

Figure 33. Instantaneous crossflow velocity patterns in planes located at $1.1R_r$ and $2.2R_r$ behind a two-bladed rotor at $\mu = .4$.

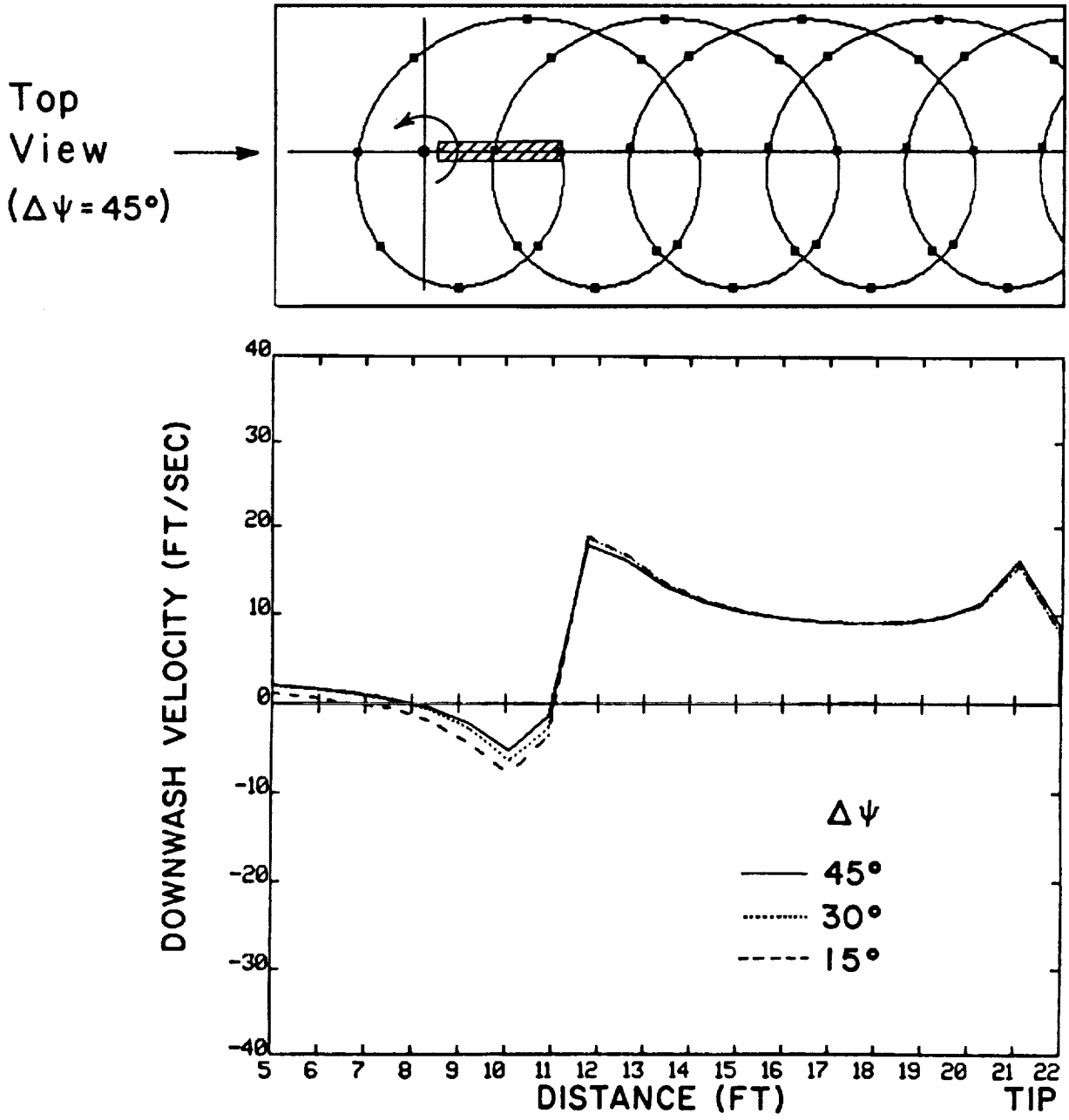

Figure 34a. Effect of vortex element size on the downwash velocity distribution along a rotor blade at azimuthal location $\psi = 0°$. Results presented for a one-bladed rotor with 3 turns of free wake with $\mu = .16$, after 5 rotor revolutions.

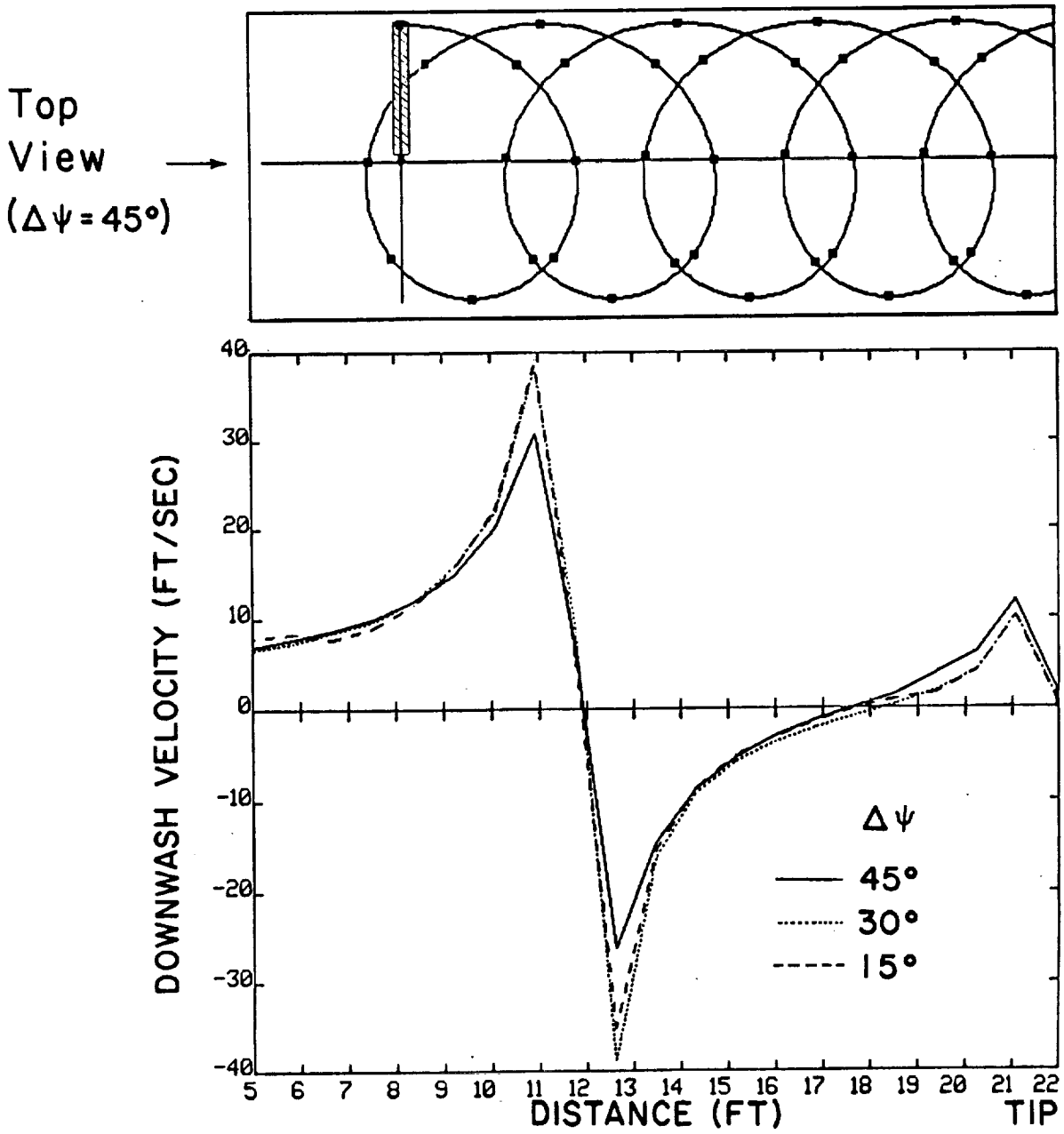

Figure 34b. Effect of vortex element size on the downwash velocity distribution along a rotor blade at azimuthal location $\psi = 90°$. Results presented for a one-bladed rotor with 3 turns of free wake with $\mu = .16$, after 5 rotor revolutions.

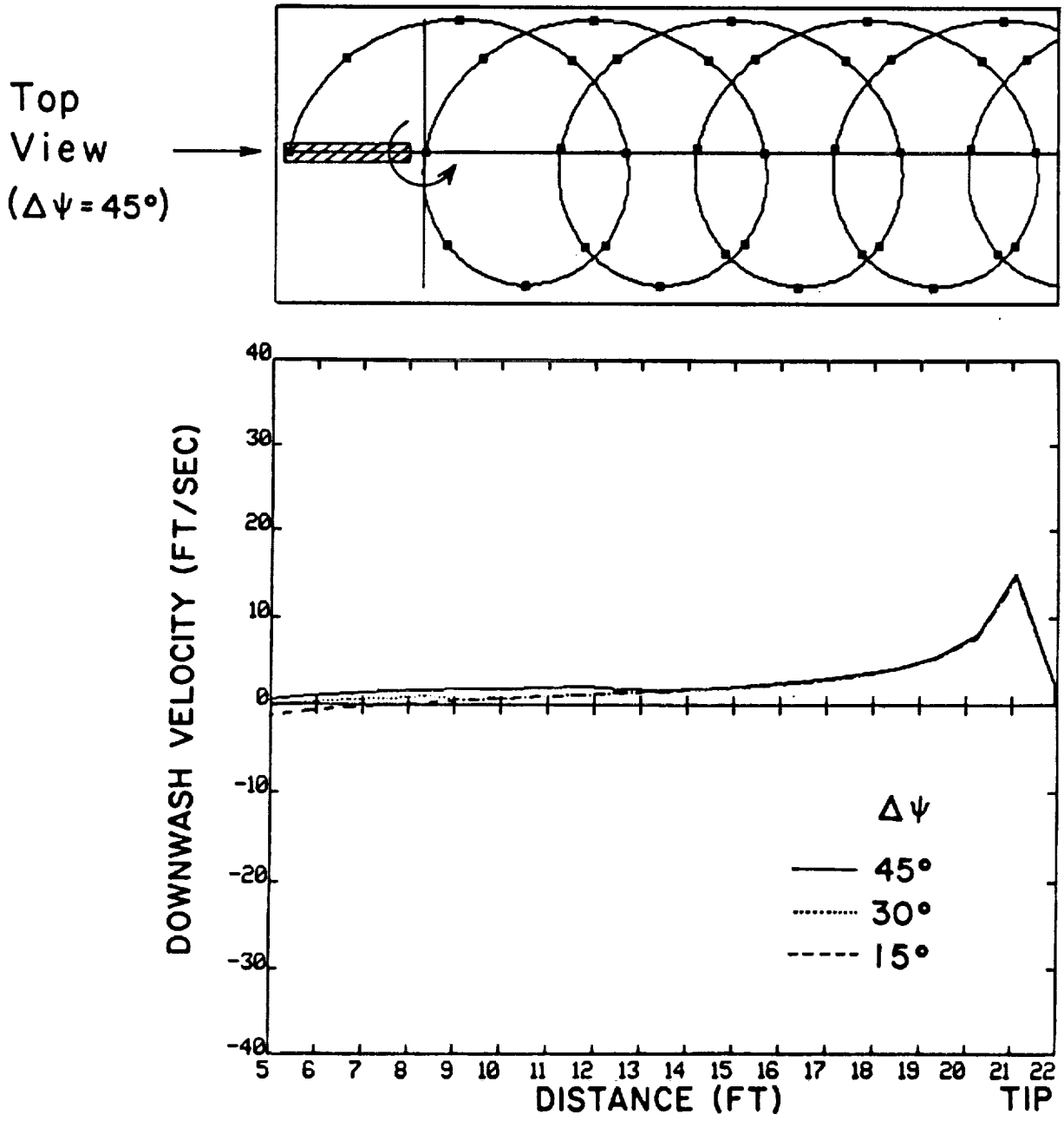

Figure 34c. Effect of vortex element size on the downwash velocity distribution along a rotor blade at azimuthal location $\psi = 180°$. Results presented for a one-bladed rotor with 3 turns of free wake with $\mu = .16$, after 5 rotor revolutions.

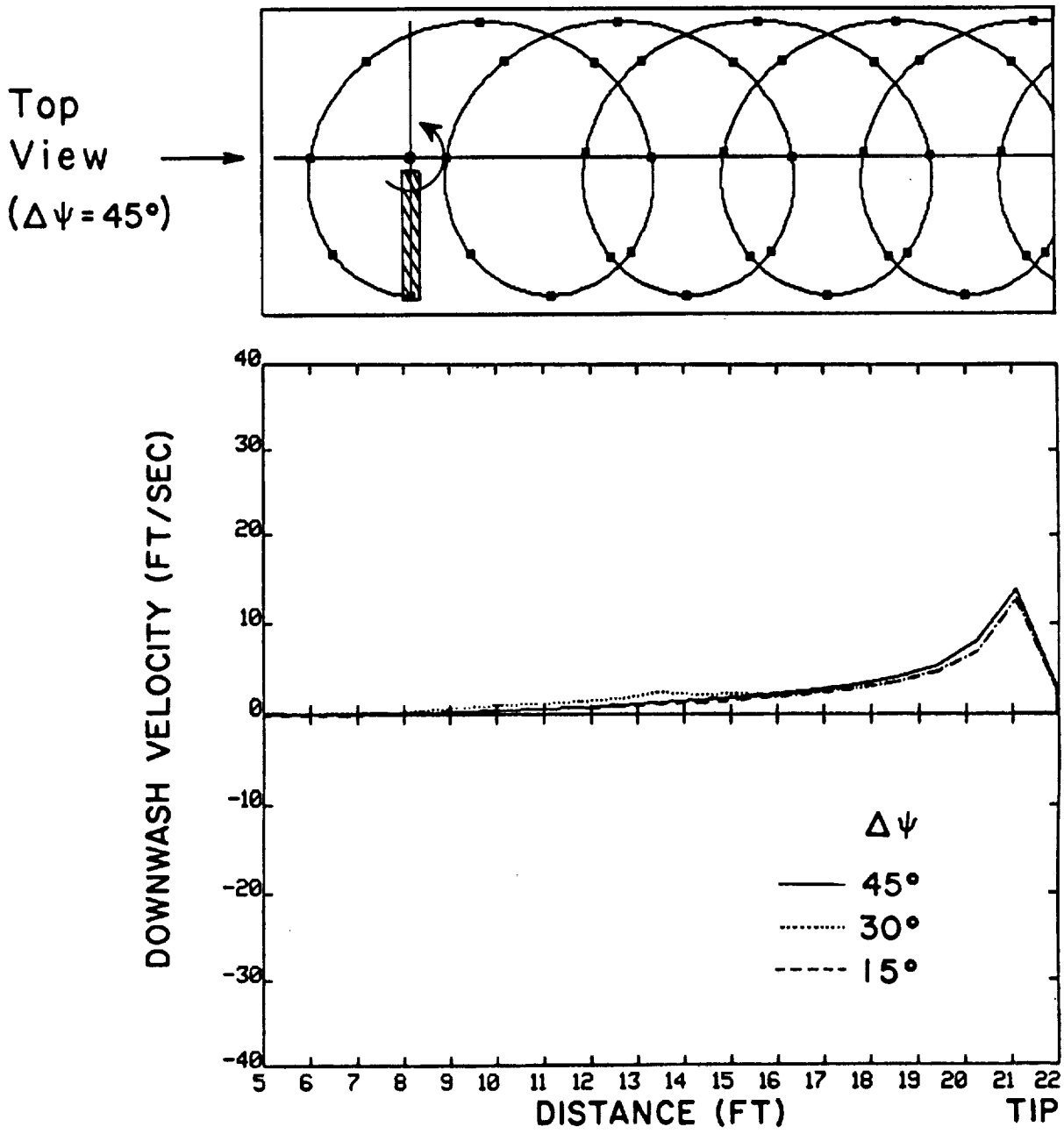

Figure 34d. Effect of vortex element size on the downwash velocity distribution along a rotor blade at azimuthal location $\psi = 270°$. Results presented for a one-bladed rotor with 3 turns of free wake with $\mu = .16$, after 5 rotor revolutions.

5. IMPLEMENTATION OF THE FREE WAKE MODEL INTO THE BOEING VERTOL B-65 CODE

5.1 Summary of the B-65 Code and its Implementation

The results given in the previous section of this report illustrate the capability of the basic free wake analysis using curved elements. A further, significant test of the free wake model is its implementation into a large mainframe rotor airloads computer program. For this exercise a copy of a version of Boeing Vertol's B-65 code was made available to Continuum Dynamics, Inc. for use on the mainframe IBM machine at Princeton University. In this section of the report the implementation of the free wake model into the B-65 code, and some predictions using the free wake model, are discussed.

The Boeing Vertol B-65 code solves for the airloads along the rotor blades using a detailed blade dynamics analysis. An initial solution for the loading is obtained assuming uniform induced inflow through the rotor plane based on momentum theory. The blade dynamic motions and equilibrium trim conditions are first determined iteratively. Then, a prescribed wake of straight-line segments generated at every 15° increment of blade rotation is trailed behind the rotor blades. The effect of these straight-line segments on the rotor plane is calculated using the Biot-Savart law. The aerodynamic model also includes a near wake and mid-wake associated with the lifting line analysis of the blade load distribution. Finally, the airloads and trim conditions are recomputed with the revised rotor plane velocities. The free wake curved vortex element model replaces the prescribed wake straight-line segment analysis.

It should be apparent that free wake and prescribed wake analyses are rather different in approach, and particularly in implementation. They will differ significantly in the computer time required for solution, quite apart from any question of relative accuracy. It is also important to realize that very little of the Boeing Vertol code deals with the prescribed wake. This is actually an advantage, because it implies that only a small portion of B-65

needs to be altered. The wake itself is broken into three parts by B-65: a near wake from 0 to 15 degrees behind the blades, represented as horseshoe vortices; a middle wake from 15 to 45 degrees behind the blades, represented by a vortex lattice; and a far wake from 45 degrees extending back a couple of turns, represented by root and tip vortex filaments. It is the far wake portion of the prescribed wake tip vortex that has been replaced by the free wake model.

To effect this substitution in as general a way as possible, additional code was written to interface B-65 to the free wake subroutines. The far wake subroutine was modified to make these additional subroutine calls, and a dormant variable was selected to trigger the various options provided in the modified code:

1. a prescribed wake solution with straight-line segments (the original technique),
2. a prescribed wake solution with curved vortex elements, and
3. a free wake solution with curved vortex elements.

The free wake solution was initialized with the prescribed wake developed by B-65. The free wake subroutines were run for the number of blade rotations equal to the number of prescribed wake turns input to B-65 for the prescribed wake analysis (an existing input). Computer timings were taken and critical parameters were compared. In all cases the input parameters correspond to the full-scale H-34 four-bladed rotor test conducted at NASA/Ames in the 40 x 80 wind tunnel,[27] at an advance ratio of 0.39 .

5.2 A Comparison of Numerical Results

Full implementation of all of the features in B-65 for the free wake was not included. A downwash velocity limiting algorithm was bypassed in the present study, and the effect of the root vortex was neglected. It was felt that the present root vortex treatment was a formulation chosen to improve the

prescribed wake prediction, and that its inclusion in the free wake analysis would require further treatment as a separate issue.

Additionally, the free wake analysis was never attempted with arcs of 15 degrees. The computer time required would be considerable in the current scheme with full velocity updating, and would reduce the practical applicability of the curved element free wake analysis in B-65. Rather, a velocity interpolation scheme was added to the free wake code so that solutions for 30 and 45 degree elements could be used to determine the blade velocities every 15 degrees. This approach was necessary because the 15 degree blade motion increments are rigidly set within the B-65 code.

Four cases were analyzed with the modified B-65 code:

1. B-65 was solved in its prescribed wake form with the neglect of the root vortices and the velocity test routine.

2. B-65 was solved using the prescribed wake spatial positions, but instead of evaluating velocities using straight-line segments, curved vortex elements were invoked.

3. B-65 was solved using two turns of free wake with 45 degree elements.

4. B-65 was solved using two turns of free wake with 30 degree elements.

Table 2 compares the values of several key parameters in B-65, all normalized by their values for case 1. Because the calculations were made at a fairly high advance ratio, the differences between the cases should be relatively small. Nevertheless, as can be seen from the table, changes can be observed in the horsepower, lift-to-drag ratio, and in some of the flapping coefficients. Interestingly, a comparison of cases 1 and 2, which use the same prescribed wake geometry and equal element sizes, shows some noticable differences attributable to the difference between element velocity fields. The apparent differences between cases 3 and 4 are probably attributable to the velocity interpolation scheme as much as to element size effects.

TABLE 2

A Comparison of B-65 Code Results for Several Versions of Prescribed and Free Wake

	Straight-Line Elements in Prescribed Wake ($\Delta\psi$ = 15°)	Curved Vortex Elements in Prescribed Wake ($\Delta\psi$ = 15°)	Free Wake with 8 Curved Elements per Blade per Revolution	Free Wake with 12 Curved Elements per Blade per Revolution
Horsepower	670.668	660.164	670.613	670.191
Lift/Drag	10.421	10.629	10.398	10.468
Flapping Coefficient A0	3.06789	3.07762	3.05795	3.05804
Flapping Coefficient A1	-0.22262	-0.15815	-0.22709	-0.26611
Flapping Coefficient A2	0.51606	0.51838	0.49982	0.51955
Flapping Coefficient A3	-0.04869	-0.03725	-0.03401	-0.04758
Flapping Coefficient A4	0.00021	0.00033	-0.00418	-0.00560
Flapping Coefficient B1	0.07976	0.06056	0.08585	0.08118
Flapping Coefficient B2	0.06359	0.05339	0.06186	0.05684
Flapping Coefficient B3	0.05993	0.06215	0.05674	0.06784
Flapping Coefficient B4	-0.03567	-0.02978	-0.02926	-0.03854
Normalized Computer Time (full velocity updating)	1.0	2.1	4.2	10.4

It is of interest to compare the computer time required for the different cases. Here it must be reiterated that a free wake time cannot be fairly compared to a prescribed wake time. Furthermore, the current free wake analysis is not fully optimized, as explained in the previous sections. The total run time for the development of the free wake solution with full velocity updating, and fully independent vortices from each blade, is approximately proportional to the square of the number of blades, the cube of the number of turns of free wake, and the cube of the number of segments in 360 degrees. In other words:

$$\text{Total time} \propto (\text{number of blades})^2 \times (\text{number of turns})^3 \times (\text{number of segments per turn})^3$$

To illustrate the consequence of this equation, the expected time difference between cases 3 and 4 may be checked. Since in the example selected there are four blades and two rotor turns, the significant variable is the number of segments. For the 45 degree case this number is 8, while for the 30 degree case it is 12. Thus, computer time should scale as $(12/8)^3$ or 3.38, a conservative estimate of the actual time difference of 10.4/4.2, or 2.48. As discussed in Section 3, the use of optimization methods such as partial updating could dramatically reduce the free wake computer time.

It is expected that calculations at lower advance ratios would show more significant differences between straight-line results and curved vortex elements.

5.3 Free Wake Results

The B-65 results can also give an indication of the structure of the trailed wake by plotting the free wake points. Several of these plots are shown in Figures 35, 36 and 37.

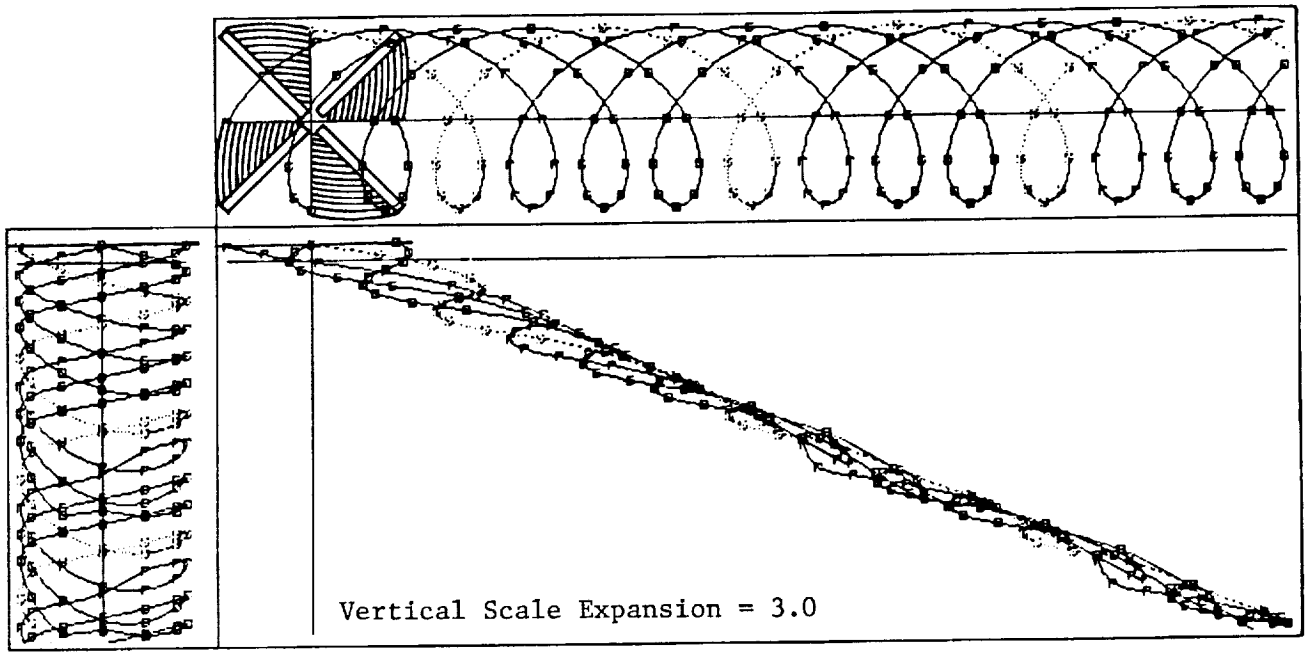

Figure 35. Three views of the initial prescribed wake for the H-34 test case.

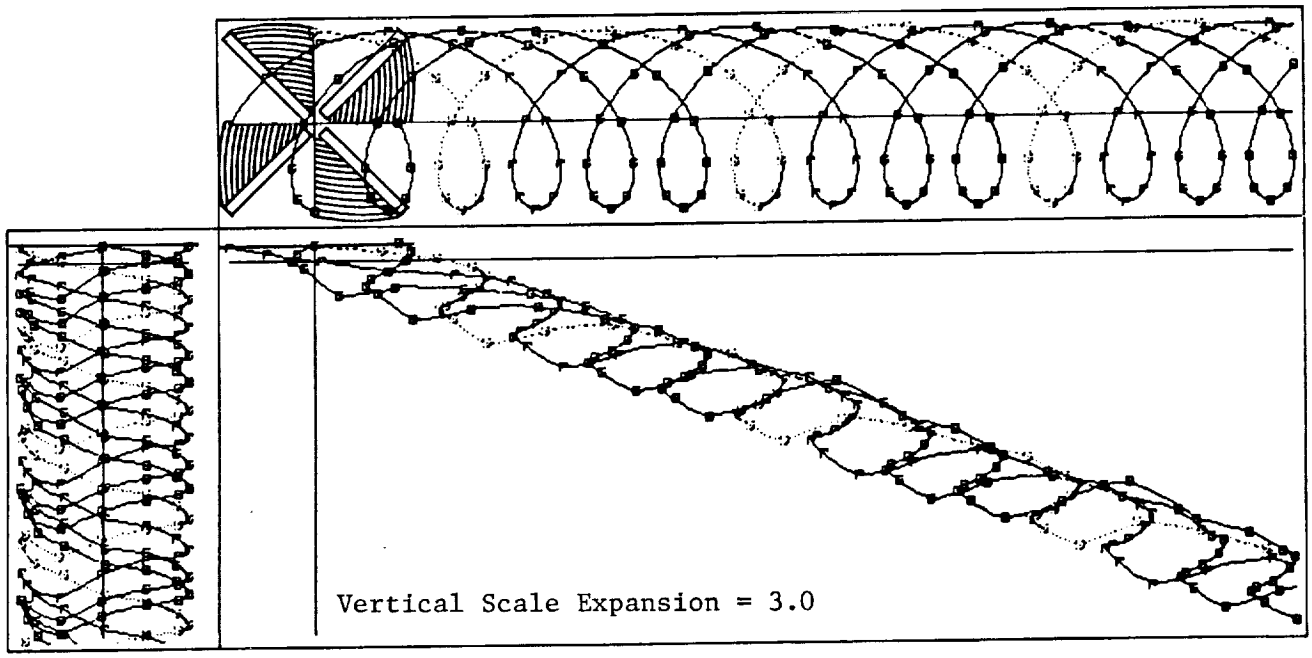

Figure 36. The free wake solution after two blade revolutions using elements generated at 30° blade rotation increments.

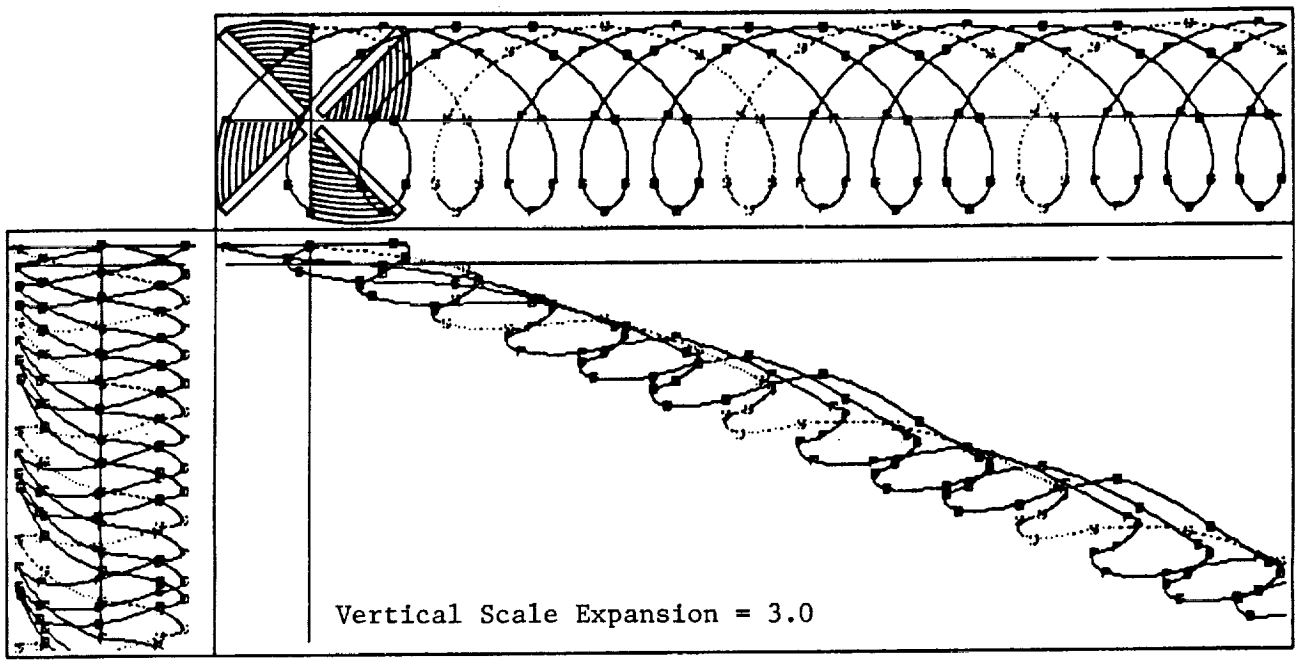

Figure 37. The free wake solution after two blade revolutions using elements generated at 45° blade rotation increments.

Figure 35 shows three views of the initial prescribed wake as defined by the B-65 code for the H-34 conditions provided by Boeing Vertol. Blade flapping and first-guess airloads are used to trail this wake behind and below the rotor disk and initialize the circulation pattern at every point in the wake.

Figure 36 illustrates the wake profile after two blade revolutions for a free wake solution using 30 degree elements. It is interesting to note that the top view has remained essentially unchanged, a feature also present to some degree for all the figures at higher advance ratios illustrated previously in this report. An important change occurs in the side views, where the center of the wake is seen to be washed downward. An examination of the front view also illustrates this feature and shows a roll-up tendency of the overlapping vortices on the advancing side. These changes can be noted by comparison to the initial conditions of Figure 35. Figure 37 illustrates a similar result for a free wake solution using 45 degree elements. At the high advance ratios used here, the difference between 30 and 45 degree elements is not large. It is only at much lower advance ratios that differences might become more apparent. However, results presented earlier showed relatively little difference between 45, 30 and 15 degree element sizes at $\mu = .16$.

6. CONCLUSIONS

This report has described the development, performance and implementation of a curved vortex element for rotor free wake calculations. The Basic Curved Vortex Element (BCVE) is derived from an approximate, but accurate integration of the Biot-Savart law for a parabolic arc. This element is intended for use in place of straight-line vortex elements, which have been used in previous free wake analyses. The results presented in this report justify the use of curved elements from the standpoint of improved accuracy and efficiency.

A curved element requires a special scheme to establish its spatial orientation and curvature between each set of collocation points along the wake. Three such schemes were considered, and an interpolated point method was chosen for the present work. This method utilizes the local information from each set of four adjacent collocation points to configure each element in space. This method contributes significantly to the overall accuracy of the scheme.

The relative accuracy of curved and straight-line elements was studied numerically and analytically. The purpose of this study was to assess the importance of straight-line element errors and to see if fewer, larger curved elements could be used instead. Scaling laws and relatively simple formulas for straight-line element errors on filaments of arbitrary shape were developed as part of this effort.

An important result of the accuracy analysis is that straight-line elements make velocity errors of order $\Gamma/4\pi R$, where R is the local radius of curvature, when the point of evaluation is within one element length of the filament. This error is of the same order as the self-induction effect which is normally included in free wake analyses. It is concluded that free wake flows involving close interactions between filaments should account for the curvature of nearby filaments to guarantee a consistent level of accuracy.

It was found that the velocity errors associated with the BCVE were typically two orders of magnitude smaller than those for straight-line elements. For this reason, it is possible to accurately represent a vortex filament with fewer, larger curved elements than straight-line elements. It is important to be able to make this trade-off to offset the increased complexity of the curved element method. In fact, because computer time depends strongly on the number of elements, numerical simulations show that a given level of accuracy can be achieved more efficiently with curved vortex elements.

The curved vortex element method was implemented into a forward flight free wake computer program. A special feature of this program is an adaptive far wake model that utilizes free wake information to extend the vortex filaments beyond the free wake region. This far wake model is based on an approximate method to sum semi-infinite rows of elements in an efficient manner. The curved element free wake, coupled with this far wake model, exhibited rapid convergence, even in regions where the free wake and far wake turns are interlaced.

Sample calculations of tip vortex motion for single and multi-bladed rotors were presented at various advance ratios. The highly distorted wake shapes share a number of common structural features. The strong tendency of filaments along the sides of the wake to "roll-up" while the center portions of the wake are convected downward is clearly evident. Crossflow plots reveal that the downstream wake flow resembles a trailing vortex pair, consistent with experimental observations. A preliminary study has shown that the downwash field at the rotor is relatively insensitive to element size, even when very large elements were used.

To further demonstrate the use of curved elements, the free wake program was successfully adapted for use with the Boeing Vertol B-65 rotor airloads program, which previously used a prescribed wake representation of the tip vortex. Sample calculations were performed for a four blade rotor with different size vortex elements.

Future work on the curved element method should focus on a full realization of its potential advantages. The accuracy and flexibility of the method pose new opportunities for the more realistic representation of rotor wake flows.

7. REFERENCES

1. Crimi, P.: "Theoretical Prediction of the Flow in the Wake of a Helicopter Rotor," Cornell Aeronautical Laboratory, Report CAL BB-1994-S, September 1965.

2. Landgrebe, A.J.: "An Analytical Method for Predicting Rotor Wake Geometries," JAHS, Vol. 14, No. 4, Oct. 1969.

3. Landgrebe, A.J.: "An Analytical and Experimental Investigation of Helicopter Rotor Hover Performance and Wake Geometry Characteristics," USAA-MRDL TR 71-24, June 1971.

4. Clark, D.R. and Leiper, A.C.: "The Free Wake Analysis: A Method for the Prediction of Helicopter Rotor Hovering Performance," JAHS, Vol. 15, No. 1, Jan. 1970.

5. Sadler, S.G.: "Development and Application of a Method for Predicting Rotor Free Wake Positions and Resulting Rotor Blade Airloads," NASA CR 1911 and CR 1912, December 1971.

6. Scully, M.P.: "Computation of Helicopter Rotor Wake Geometry and Its Influence on Rotor Harmonic Airloads," M.I.T., ASRL TR 178-1, Mar. 1975.

7. Johnson, W.: "Development of a Comprehensive Analysis for Rotorcraft - I. Rotor Model and Wake Analysis," Vertica, Vol. 5, 1981, pp. 99-129.

8. Johnson, W.: Helicopter Theory, Princeton University Press, 1980. Chapter 13 contains a discussion of free wake methods.

9. Summa, J.M. and Clark, D.R.: "A Lifting-Surface Method for Hover/Climb Airloads," Proceedings of the 35th Annual National Forum of the American Helicopter Society, Washington, D.C., May 1979.

10. Summa, J.M. and Maskew, B.: "A Surface Singularity Method for Rotors in Hover or Climb," USAAVRADCOM TR 81-D-23, December, 1981.

11. Saberi, H.-A.: "Analytical Model of Rotor Aerodynamics in Ground Effect," NASA CR 166533, Dec. 1983.

12. Rosen, A. and Graber, A.: "Free Wake Model of Hovering Rotors Having Straight or Curved Blades," Proceedings of the International Conference on Rotorcraft Basic Research, sponsored by the Army Research Office and the American Helicopter Society, Research Triange Park, N.C., February, 1985.

13. Bliss, D.B., Quackenbush, T.R. and Bilanin, A.J.: "A New Methodology for Helicopter Free Wake Analyses," Paper No. A-83-39-75-000 presented at the 39th Annual Forum of the American Helicopter Society, May 1983.

REFERENCES (Cont'd)

13. Bliss, D.B., Quackenbush, T.R. and Bilanin, A.J.: "A New Methodology for Helicopter Free Wake Analyses," Paper No. A-83-39-75-000 presented at the 39th Annual Forum of the American Helicopter Society, St. Louis, MO, 1983.

14. Bliss, D.B., Teske, M.E. and Quackenbush, T.R.: "Free Wake Calculations Using Curved Vortex Elements," Proceedings of the International Conference on Rotorcraft Basic Research, sponsored by the Army Research Office and the American Helicopter Society, Research Triangle Park, NC, February 1985.

15. Bliss, D.B., Wachspress, D.A. and Quackenbush, T.R.: "A New Approach to the Free Wake Problem for Hovering Rotors." Proceedings of the 41st Annual Forum of the American Helicopter Society, Fort Worth, TX, May 1985.

16. Leonard, A.: "Numerical Simulation of Interacting, Three-Dimensional Vortex Filaments," Proc. of the 4th International Conference on Numerical Methods in Fluid Dynamics, Colorado, Springer-Verlag, 1974, pp. 245-250.

17. Bliss, D.B.: "The Dynamics of Curved Rotational Vortex Lines," M.S. thesis, Department of Aeronautics and Astronautics, Massachusetts Institute of Technology, Sep. 1970.

18. Widnall, S.E., Bliss, D.B., and Zalay, A.: "Theoretical and Experimental Study of the Stability of a Vortex Pair," in Aircraft Wake Turbulence and its Detection, edited by Olsen J., Goldberg, A. and Rogers, M. Plenum Press, New York, 1971, pp. 305-338.

19. Moore, D.W., and Saffman, P.G.: "The Motion of a Vortex Filament with Axial Flow," Philosphical Transactions of the Royal Society of London, Vol. 272, July 1972, pp. 403-429.

20. Hamming, R.W.: Numerical Methods for Scientists and Engineers, 2nd Ed., McGraw-Hill, New York, 1973.

21. Bilanin, A.J., and Donaldson, C. duP.: "Estimation of Velocities and Roll-Up in Aircraft Vortex Wakes," Journal of Aircraft, Vol. 12, No. 7, July 1975, pp. 578-585.

22. Donaldson, C. duP., and Bilanin, A.J.: "Vortex Wakes of Conventional Aircraft," AGARD-AG-204, May 1975.

23. Donaldson, C. duP.: "A Brief Review of the Aircraft Trailing Vortex Problem," AFOSR-TR-71-1910, May 1971.

24. Tung, C., Pucci, S.L., Caradonna, F.X. and Morse. H.A.: "The Structure of Trailing Vortices Generated by Model Rotor Blades," Vertica, Vol. 7, No. 1, 1983, pp. 33-43.

25. Ballard, J.D., Orloff, K.L., and Luebs, A.B.: "Effect of Tip Planform on Blade Loading Characteristics for a Two-Bladed Rotor in Hover," NASA Technical Memorandum 78615, Nov. 1979.

26. Heyson, H.H. and Katzoff, S.: "Induced Velocities Near a Lifting Rotor with Nonuniform Disk Loading," NACA Report 1319, 1957.

27. Rabbott, J.P., Lizak, A.A. and Paglino, V.M.: "A Presentation of Measured and Calculated Fullscale Rotor Blade Aerodynamic and Structural Loads," USAAVLABS, TR66-31, July 1966.

28. Gradshteyn, I.S., and Ryzhik, I.W.: Tables of Integrals, Series, and Products, 4th ed., Academic Press, 1965. See pages 83 and 81.

APPENDIX A

The BCVE requires the evaluation of integrals of the form

$$I_n = \int \frac{x_1^n}{\left[cx_1^2 + bx_1 + a\right]^{3/2}} dx_1 \tag{A-1}$$

Let $R_1 \equiv cx_1^2 + bx_1 + a$ and $\Delta \equiv 4ac-b^2$. Then for the values $n = 0,1,2,3$ these integrals are found to be (Ref 28)

$$I_o = \frac{2(2cx_1 + b)}{\Delta\sqrt{R_1}} \tag{A-2}$$

$$I_1 = -\frac{2(2a + bx_1)}{\Delta\sqrt{R_1}} \tag{A-3}$$

$$I_2 = -\frac{(\Delta - b^2)x_1 - 2ab}{c\Delta\sqrt{R_1}} + \frac{1}{c}\int \frac{dx_1}{\sqrt{R_1}} \tag{A-4}$$

$$I_4 = \frac{c\Delta x_1^2 + b(10ac - 3b^2)x_1 + a(8ac - 3b^2)}{c^2\Delta\sqrt{R_1}} - \frac{3b}{2c^2}\int \frac{dx_1}{\sqrt{R_1}} \tag{A-5}$$

where

$$\int \frac{dx_1}{\sqrt{R}} = \begin{cases} \frac{1}{\sqrt{c}} \ln(2\sqrt{cR_1} + 2cx_1 + b) & c > 0 \\ \frac{-1}{\sqrt{-c}} \arcsin \frac{2cx_1 + b}{\sqrt{-\Delta}} & c < 0 \ , \ \Delta < 0 \end{cases} \tag{A-6}$$

It is clear from the form of these integrals that difficulties in numerical evaluation will be encountered when $c = 0$ and/or $\Delta = 0$. These difficulties are a consequence of removing the term $\varepsilon^2 x_1^4$ from the denominator of the integrand and thereby reducing its order. This problem occurs outside the region where the subinternal integration using the quadratic model of $\varepsilon^2 x_1^4$ is applied. It can be shown analytically that these integrals still exist at $c = 0$ and $\Delta = 0$ as long as the limits of integration are applied. However, from a numerical standpoint, near $c = 0$ and $\Delta = 0$ the net result is obtained as the difference between two large numbers. The programming for the element model includes a special treatment to avoid this difficulty. The correction procedure is based in part on the fact that the integrals, and in particular c and Δ, are known only to a certain level of accuracy because of the neglect of the $\varepsilon^2 x_1^4$ term (which is the source of the problem anyway). Small quantities of order $\varepsilon^2 \ell^4$ are selectively introduced into c and Δ to prevent their vanishing. Careful testing has shown that this correction procedure yields smooth, well behaved results.

1. Report No.	2. Government Accession No.	3. Recipient's Catalog No.
NASA CR-3958		

4. Title and Subtitle	5. Report Date
A New Methodology for Free Wake Analysis Using Curved Vortex Elements	December 1987
	6. Performing Organization Code

7. Author(s)	8. Performing Organization Report No.
Donald B. Bliss, Milton E. Teske, and Todd R. Quackenbush	84-6
	10. Work Unit No. 505-61-51

9. Performing Organization Name and Address	11. Contract or Grant No.
Continuum Dynamics, Inc. P.O. Box 3073 Princeton, New Jersey 08540	NAS2-11295
	13. Type of Report and Period Covered Contractor Report Final Report

12. Sponsoring Agency Name and Address	14. Sponsoring Agency Code
National Aeronautics and Space Administration Washington, DC 20546	

15. Supplementary Notes

Ames Technical Monitor: Fort F. Felker, MS 247-1, (415)694-6096, Ames Research Center Moffett Field, California 94035

16. Abstract

A method using curved vortex elements has been developed for helicopter rotor free wake calculations. The Basic Curved Vortex Element (BCVE) is derived from the approximate Biot-Savart integration for a parabolic arc filament. When used in conjunction with a scheme to fit the elements along a vortex filament contour, this method has a significant advantage in overall accuracy and efficiency when compared to the traditional straight-line element approach. A theoretical and numerical analysis shows that free wake flows involving close interactions between filaments should utilize curved vortex elements in order to guarantee a consistent level of accuracy. The curved element method was implemented into a forward flight free wake analysis, featuring an adaptive far wake model that utilizes free wake information to extend the vortex filaments beyond the free wake region. The curved vortex element free wake, coupled with this far wake model, exhibited rapid convergence, even in regions where the free wake and far wake turns are interlaced. Sample calculations are presented for tip vortex motion at various advance ratios for single and multiple blade rotors. Cross-flow plots reveal that the overall downstream wake flow resembles a trailing vortex pair. A preliminary assessment shows that the rotor downwash field is insensitive to element size, even for relatively large curved elements.

17. Key Words (Suggested by Author(s))	18. Distribution Statement
Helicopter Wake Free Wake Analysis Vortex Dynamics Rotor Aerodynamics	Unclassified - Unlimited Subject Category 02

19. Security Classif. (of this report)	20. Security Classif. (of this page)	21. No. of Pages	22. Price
Unclassified	Unclassified	136	A07

For sale by the National Technical Information Service, Springfield, Virginia 22161

NASA-Langley, 1987